NANOPHOTONIC FORCE MICROSCOPY: MEASURING NANOPARTICLE INTERACTIONS ON THE THERMAL ENERGY SCALE USING NEAR-FIELD OPTICAL TRAPPING AND LIGHT SCATTERING

A Dissertation

Presented to the Faculty of the Graduate School

of Cornell University

in Partial Fulfillment of the Requirements for the Degree of

Doctor of Philosophy

by

Perry Matthew Schein

May 2017

NANOPHOTONIC FORCE MICROSCOPY: MEASURING NANOPARTICLE INTERACTIONS ON THE THERMAL ENERGY SCALE USING NEAR-FIELD OPTICAL TRAPPING AND LIGHT SCATTERING

Perry Matthew Schein, Ph.D.

Cornell University 2017

Nanoparticles are becoming ubiquitous in many applications including diagnostic assays, drug delivery and therapeutics, enhanced hydrocarbon recovery, and catalysis. However, there are challenges in the quality control of these products - it is necessary to ensure that nanoparticle suspensions contain particles of the appropriate size, within tolerable polydispersity, and that they maintain colloidal stability in face of potentially harsh environmental conditions. Through my doctoral research, I have developed Nanophotonic Force Microscopy, a technique for directly measuring nanoparticle interactions in the native suspension environment. This technique works by measuring the fluctuations in the intensity and position of scattered light as a nanoparticle of interest interacts with a nanophotonic optically trapping structure. In this dissertation, I demonstrate the use of Nanophotonic Force Microscopy to measure thermal energy scale interaction potentials and sub-pN scale interaction forces on dielectric and metallic nanoparticles with characteristic sizes of 50-800 nm. I then extend this technique to make simultaneous measurements of nanoparticle stability, diffusion coefficient, and sample polydispersity. This orthogonal measurement is accomplished by tracking the motion of nanoparticles in all three special dimensions as they interact with the evanescent field near an optical waveguide. This near-field interaction generates forces and results in motion in all three spatial dimen-

sions. Along the propagation axis of the waveguide (x-direction) the nanoparticles are propelled by the optical forces which allow for a measurement of the sample polydispersity. Parallel to the plane of the waveguide and perpendicular to the optical propagation axis (y-direction) they experience an optical gradient force generated from the waveguide mode profile which confines them in a harmonic potential well, which can be used to provide a measurement of the diffusion coefficient. Normal to the surface of the waveguide (z-direction) they experience an exponential downward optical force balanced by the surface interactions that confines the particles in an asymmetric well, which is used to probe the suspension stability. The use of a waveguide integrated into a microfluidic channel allows for high throughput implementation of this technique, and the simultaneous measurement addresses several of the gaps left by current measurement technologies.

BIOGRAPHICAL SKETCH

Perry Schein was born on December 15, 1989 and grew up in Rockville Centre, New York where he attended South Side High School, graduating in 2008. Following high school, he received the Alexander Graham Bell scholarship to attend Boston University, where he majored in Mechanical Engineering, graduating Summa Cum Laude in 2012. Perry joined the Sibley School of Mechanical and Aerospace Engineering at Cornell University in 2012, where he worked in the Integrated Micro- and Nanofluidic Systems lab with Professor David Erickson on developing nanophotonic methods for characterizing nanoparticles, publishing several peer-reviewed articles. He earned the Master of Science Degree in Mechanical Engineering from Cornell in 2015. In addition to his dissertation work, at Cornell Perry was also involved in research to develop advanced photocatalytic reactors for carbon dioxide conversion, and provided major technical contributions to advance the technology to the semi-final round of the NRG Cosia Carbon XPrize.

ACKNOWLEDGEMENTS

Completing my doctoral studies has been a long journey, and along the way I relied on the help and support of many colleagues and friends. First, I'd like to acknowledge my advisor, David Erickson, for all of his support over the years, in helping me to develop as a scientist, engineer, and communicator, and for giving me the flexibility to pursue my research in my own way, but with excellent guidance, feedback, and direction. I'd like to thank my committee members Professors Warren Zipfel and Donald Koch for their support over the years. I'd also like to thank the staff of Nanobiotechnology Center at Cornell for maintaining their lab space and equipment, providing training, and allowing me to set up extra equipment and computers in their lab - without their support many of the experiments featured in this dissertation would not have been possible. Funding for the research in this dissertation came from the United States National Institutes of Health and Department of Energy; during my Ph.D. studies I was also supported financially through a departmental fellowship, two teaching assistantships, and the Atkinson Center for a Sustainable Future, who supported my work on carbon dioxide conversion.

I'd like to thank all of my research colleagues who I was fortunate enough to collaborate with during my graduate studies. In particular, I'd like to thank Pilgyu Kang, Xavier Serey, and Dakota O'Dell for helping me in getting started with optical trapping when I first joined the group years ago, and for all of their contributions and useful discussions on this research over the years. I'd also like to acknowledge Bernardo Cordovez and Chris Earhart at Optofluidics for all of their advice and useful discussions - working closely with people interested in the commercialization of my research was a valuable learning experience for me. I'd also like to acknowledge my collaborators Jessica Silva and Tobias Han-

rath who I worked with on the photocatalysis project, and Rifat Rahman in Information Science who I worked with on photoacoustics.

I'd like to acknowledge my friends and colleagues in the Integrated Micro- and Nanofluidic Systems lab and the Sibley School for all of their help over the years and for making my time in graduate school more enjoyable - in particular I'd like to thank my labmates Aadhar Jain, Michael Mak, Matthew Mancuso, Li Jiang, Abdullah Gumus, Saad Ahsan, Seoho Lee, Zhendga Lu, Liz Rey, Ryan Snodgrass, Rick Wang, Sasank Vemulapati, and Elizabeth Case. Whether it was providing helpful comments and feedback, discussing science fiction films, or drinking Thai iced tea and playing board games, these people provided some of the most memorable moments of my time in Ithaca. I'd also like to thank my friends from the Rockville Centre, Boston, and Dresden days that stayed in touch over the years - I've enjoyed visiting all of you in your new cities and your visits to Ithaca. I'd also like to thank my mother, Mindy Myers, and my brother, Jeremy Schein, for their support during the long journey of graduate school.

TABLE OF CONTENTS

LIST OF FIGURES

CHAPTER 1

INTRODUCTION

1.1 Summary of Research and Scope of Dissertation

The goal of this research is to develop and demonstrate new and improved methods for characterizing the physical and chemical properties of nanoparticle suspensions that dictate their functionality and stability using near-field photonics. Nanoparticles, with characteristic dimensions on the scale of tens to hundreds of nanometers are gaining widespread adoption in products and applications that take advantage of unique properties enabled by their small sizes and high surface-area to volume ratios. However, quality control of these products remains a key concern, motivating research into improved characterization techniques. Near-field optical trapping, in which the evanescent fields surrounding nanophotonic structures such as waveguides, photonic crystal resonators, and ring resonators are exploited to exert optical forces has shown promise in manipulating nanoparticles, and subjecting them to forces on the length scales of interest for colloidal characterization.

In this dissertation, I present several important steps towards achieving this goal. The central idea of this work is that as a nanoparticle interacts with the evanescent optical field near a nanophotonic device, it scatters light, and tracking the magnitude and position of this scattered over time as the nanoparticle moves allows us to make statistical mechanical measurements of the nanoparticle's properties. In Chapter 1, I introduce some of the key challenges associated with maintaining, predicting, and assessing the stability of nanoparticle products relevant to key application areas. I summarize currently used charac-

terization techniques, noting areas where improvement is needed, and provide background on the physics of near-field optical trapping, the platform I will use in later chapters for developing new nanoparticle characterization techniques. In Chapter 2, I introduce Nanophotonic Force Microscopy, a method for directly measuring the interactions between nanoparticles and surfaces, demonstrating the ability to make measurements of pico-Newton scale forces on 100 nm diameter particles. In Chapter 3, I extend this technique to a high-throughput implementation that uses a single-mode waveguide to interrogate many nanoparticles in rapid succession. In this chapter I also provide further analysis of the resolution and experimental uncertainties in these measurements and investigate how many samples are needed to provide accurate data on each particle. In Chapter 4, I extend the Nanophotonic Force Microscopy technique to tracking the in-plane motion of the nanoparticle, and show how tracking the motion in all three spatial dimensions leads to additional characterizations of the nanoparticle size as well as the surface interactions. In Chapter 5, I apply near-field light scattering to measure the short-timescale dynamics of the nanoparticle motion, in contrast to the long time scale equilibrium statistical mechanics, and show how this physics can lead to additional insights about the colloidal suspension. In Chapter 6 I summarize the research conclusions and give an outlook for future lines of research inquiry in this field.

1.2 Characterizing Nanoparticles and Their Interactions

1.2.1 Nanoparticle Applications and Stability in Harsh Environments

Colloidal nanoparticles, defined as those having characteristic sizes with at least one physical dimension on the order of 1 -1000 nm, have found use in many application areas, primarily where their small size and high surface-area to volume ratio enable physical and chemical properties not available in the material at "bulk" scale, or where their small size enables transport through highly confined regions. Specifically, in recent years nanoparticle products have been used as markers in diagnostic assays [4, 5], as therapeutic agents and for enhanced drug delivery [6], for industrial catalysis [7], in enhanced hydrocarbon recovery [8, 9], and in cosmetic products [10]. The ability to perform in environments with tightly confined spaces with characteristic particle-wall separation distances only a few times the particle diameter, high salt concentrations, and elevated temperatures is especially important for in vivo biological applications and enhanced oil recovery. For in vivo applications, nanoparticles undergo transport through capillaries with characteristic diameters in the 4-12 μm range [11], face exposure to high salt concentrations [12], and experience binding interactions with suspended proteins [13]. These interactions can reduce the functionality of the product and in some cases trigger an immune response. In oil reservoir applications, maintaining stability is a critical concern as salt concentrations in reservoir brine typically exceed 300 mM, and temperatures greater than 50°C are routinely encountered [9]. Designing nanoparticle suspensions to withstand these conditions is a major area of research, and sig-

nificant efforts focus on developing stabilizers and particle coatings for these application scenarios. In engineering these particles, understanding and predicting the particle-particle and particle-surface interactions can provide a great deal of insight to the development of improved products.

1.2.2 Theoretical Understanding of Nanoparticle Interactions

Most current theoretical understanding of nanoparticle interactions comes from the Derjaguin-Landau-Verway-Overbeek (DLVO) theory, which has been modified over the last 70 years with a series of extensions to different physical systems. This extended-DLVO (EDLVO or sometimes XDLVO [14]) family of theories suffers from some key limitations that hinder its performance in predicting physical outcomes in many situations.

The central piece of the DLVO theory is that the total interaction potential of a colloidal particle is the sum of the contributions due to the van der Waals and electrostatic forces. Modelling these forces requires parameters such as the surface potential that must be obtained empirically, and cannot be predicted a priori for a given particle suspension. Even with these empirical parameters, measured force profiles often deviate from the DLVO model. To account for these deviations, researchers have added numerous other force terms to the summation, including terms describing hydrophobic, osmotic, and steric forces [14], terms which contain their own sets of empirically derived parameters. This is especially true at high salt concentrations, which are relevant for biological and industrial applications [12]. There are also some fundamental problems with the linear summation of forces approach, as elaborated by Ninham and

co-workers in several papers over the last twenty years [15, 16, 12, 17]. Because of these flaws, to gain predictive insight into the behavior of real nanoparticle suspensions, new approaches are needed. Here, we explore the possibility of directly measuring the particle interactions in the native suspension environments. Another branch of active research seeks to determine the potential of mean force between interacting nanoparticles through atomistic simulations [18, 19]. In Chapter 6, we will briefly discuss the potential for future lines of research to bridge these two approaches.

1.2.3 Nanoparticle Characterization Techniques

Due to the limitations of the theory and difficulties in predicting a priori how real, functional nanoparticles will behave in complicated suspension environments, researchers and those responsible for quality assurance of nanoparticle products have turned to a variety of tools for measuring nanoparticle properties. These can be classified as direct techniques which measure the strength of the colloidal interactions, and indirect techniques that measure size dependent optical, electrical, and transport properties to infer if aggregation has occurred.

Colloidal Probe Atomic Force Microscopy

One commonly used direct measurement technique is colloidal probe atomic Force Microscopy (AFM). This technique was independently developed by Ducker [20] and Butt [21] in 1991, and builds on earlier applications of AFM to force measurements in other contexts [22, 23]. In colloidal probe AFM, each colloidal particle of interest to be measured is physically attached to micro-

mechanical cantilevered beam, making sample preparation a time-consuming process. The experiments are performed in a liquid flow cell, where conditions matching the use-environment of the colloidal product such as salt concentration and pH can be applied. The cantilever with the attached particle is then lowered down towards the surface. The deflection of the cantilever is measured by focusing a laser beam onto the back side (away from the surface) of the cantilever and measuring the reflected light with a position sensitive photodetector. When the stiffness of the cantilever is known, this measured displacement can be calibrated to give a measure of the net force acting to displace the probe.

The measurement can either be made by moving the colloidal probe close to a reference surface to measure a particle-surface interaction, or by scanning the colloidal probe over the position of a second colloidal particle deposited on a surface to measure a particle-particle interaction. The probe-surface separation distance can be controlled, and the result from colloidal probe AFM is the force-distance curve, where the force (sometimes normalized by the particle size) is plotted as a function of the probe-surface separation distance. This gives direct insight into the strength of the interactions, and has the advantage of being capable of measuring both attractive and repulsive forces. Colloidal probe AFM has been successfully applied to study many physical systems, including those featuring van der Waals forces [24], polymer bridging interactions [25] and macromolecular depletion interaction forces [26]. However, one key limitation of this technique is that the measurements are limited by thermal noise: in a liquid environment, due to molecular collisions the cantilever will displace even in the absence of any applied colloidal forces, effectively setting a lower limit noise floor on the forces that can be measured using this technique. This is discussed through a quantitative example in Chapter 2. As smaller probe par-

ticles experience weaker interactions, in effect this sets a limitation to the sizes of particles that can be probed with colloidal AFM. In practice, most colloidal probe AFM experiments use probe particles with diameters in the range of tens of μm, and measure forces on the nN scale, with typical reported force resolutions in the 10-50 pN range [27].

Total Internal Reflection Microscopy

A strategy for getting around the thermal noise limitations of AFM is to use the thermal fluctuations of a nanoparticle as the measurement itself. This is a passive, observational measurement rather than one where the experimenter can impose the conditions onto the particles, and is stochastic in nature, but it does achieve a direct measurement of the interaction profile. This can be accomplished by measuring the Brownian motion of the colloidal particle of interest as it experiences "drift" due to the colloidal forces.

The typical experimental implementation involves generating an evanescent field, and using the light scattered by the particle as it interacts with the evanescent field to measure the particle position. This is conventionally accomplished by shining light through a waveguiding structure (traditionally laser light through a glass microscopy slide) at an angle beyond the critical angle, causing the light to undergo total internal reflection and generating an evanescent field at the interface. A flow channel is placed on the surface of the slide where the evanescent field is generated, and the colloidal suspension is flowed past. When particles are close to the surface, they scatter more light, and when they are further away, the signal decays exponentially. The scattered light is collected through an objective lens and measured with either a camera or pho-

tomultiplier tube. When many measurements of the particle's scattered light intensity are made, the statistical distribution of states sampled is related to the potential energy landscape through the Boltzmann statistics. As a statistical measurement that essentially examines the confined Brownian motion of the particle, TIRM is not limited by thermal noise and can resolve sub-pN forces and k_BT scale interaction energies.

First developed in the late 1980s by Prieve and co-workers [28, 29], TIRM has been used successfully to study electrostatic interactions, van der Waals effects [30], depletion interactions [31], Casimir forces [32], fundamental statistical physics [33], and many other phenomena, typically involving weak interactions between micrometer scale particles and surfaces. TIRM has limits when going to smaller particles, in terms of both engineering challenges in detection and physical challenges in confining the particles for long enough times to make good measurements. Smaller particles scatter much less light, and so the signal-to-noise ratio decreases with decreasing size. Another issue is that smaller particles diffuse faster, making the probability of finding them near a scattering surface for long enough to make a good measurement small. While in the initial TIRM studies the gravitational settling of the particles was sufficient to balance the electrostatic forces, these quickly become insufficient when looking at particles in the single micrometer and smaller regime. Approaches to addressing this in the TIRM literature include the use of free space optical traps to force particles close to the surface with radiation pressure forces, which limits the technique to dielectrics larger than about 1 micrometer [34, 35]. Another approach to increase particle confinement has been the introduction of a second surface located several hundred nanometers above the scattering surface to physically force particles into the evanescent field. This can be accomplished

by using a deposited nanoparticle as a spacer [36, 37, 38], or nanochannels fabricated using electron beam lithography [39]. With the enhanced confinement provided by the geometry, these studies were able to study smaller particles than in conventional TIRM implementations. To overcome the signal-to-noise challenges they used either metallic particles [36, 37, 38] which interact much more strongly with the optical field than dielectrics [40], or relied on fluorescent labels [39] which resulted in inaccurate results due to poor temporal resolution.

Measurements of Optical and Electrical Properties

In many cases, rather than measuring nanoparticle interactions directly as with AFM and TIRM it is easier to infer stability by examining the optical or electrical properties of the particles. These properties can be easily measured at high-throughput using available commercial instrumentation, and are capable of measuring smaller particles than those typically studied in AFM and TIRM with less extensive sample preparation and with simpler experiments.

For example, metallic nanoparticles including gold and silver particles that exhibit localized surface plasmon resonances are used frequently in applications. The localized surface plasmon resonance peak is a strong function of the particle size and shape [41], so measuring the spectral location and width of this peak gives insight into the constituent particles in the sample. These resonances can be observed by performing spectroscopic measurements, such as UV-Vis spectroscopy, where a cuvette containing the nanoparticle suspension is illuminated by light at a series of wavelengths, and the optical extinction through the sample is measured as a function of this illumination. UV-Vis measurements can be used to assess the stability of the suspension - if the particles aggregate

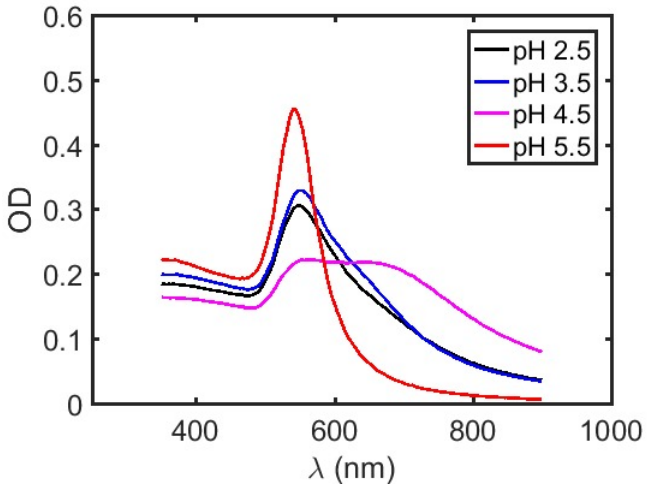

Figure 1.1: UV-Vis absorption spectra showing measured optical density (OD) as a function of illumination wavelength for gold nanoparticles with nominal diameter 60 nm suspended in buffers with pH 2.5 (black), 3.5 (blue), 4.5 (purple) and 5.5 (red), as measured using the Molecular Devices SpectraMax Plus 384 spectrophotometer. The shift in the localized surface plasmon resonance peak towards longer wavelengths is indicative of particles aggregating.

the peak will shift to a longer wavelength. They can also be used to asses the application of a particle coating as this will cause a small shift in the resonance peak as the particle effectively becomes larger, and sample polydispersity which results in a broadening of the peak. These measurements can be made to assess the behavior of the nanoparticles in response to different suspension conditions, such as changes in pH [42, 43, 44]. Figure 1.1 shows the resonance shift for gold nanoparticles suspended in buffers at different pH.

In many nanoparticle systems, electrostatic repulsion between similarly charged particles provides an important stabilizing force. One experimentally measurable parameter that gives reasonable empirical insight into the strength of these interactions is the ζ-potential, the apparent electrokinetic potential mea-

sured for a particle undergoing electrophoresis. In typical commercial systems the ζ-potential is measured using laser Doppler electrophoresis in which an electric field is applied across the suspension, causing the particles to undergo electrophoretic motion. The electrophoretic velocity of the particles is determined by measuring the Doppler shift in the light scattered by the particles, which is related to the electrophoretic mobility and potential through established relations [45]. As the ζ-potential is a measure of the potential difference between the effective slip plane around the particle and the bulk electrolyte solution, it is a function of the environmental conditions and it is especially sensitive to changes in pH and ion species and concentration, as shown in Figure 1.2. As a general guideline, for systems in which the electrostatic forces are most important in determining stability, ζ-potential of $>$30 mV or $<$ -30 mV typically indicates a stable suspension. However, this does not tell the whole story, as other forces and effects may actually influence the stability of a nanoparticle suspension in a complex environment allowing electrically neutral particles to remain stable.

Dynamic Light Scattering and Nanoparticle Tracking Analysis

Another strategy for assessing nanoparticle suspensions is to measure the size and size distribution of the particles. This provides an important quality assurance metric as it can identify the polydispersity of the sample as well as highlight the presence of aggregates or impurities. One way of measuring the particle size is to measure the diffusion of the nanoparticles, and relate this to the effective hydrodynamic particle size through the Stokes-Einstein relation:

$$R = \frac{k_B T}{6\pi\eta D} \tag{1.1}$$

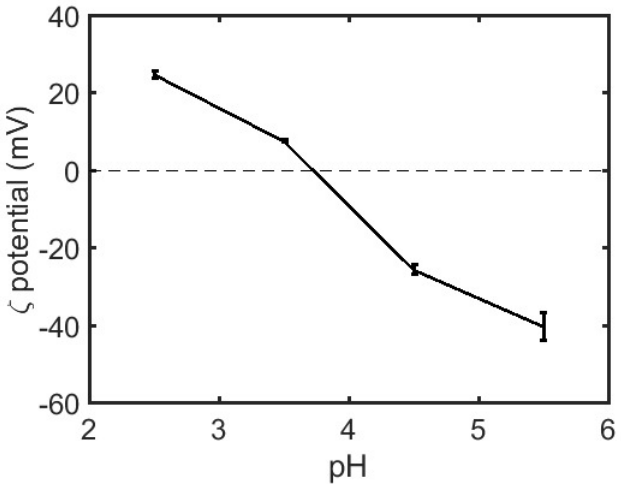

Figure 1.2: ζ-potential as a function of suspension pH for nominal diameter 50 nm gold nanoparticles, as measured using the Malvern Zetasizer Nano ZS. At the ends of the curve, the particles are electrostatically stabilized by the positive or negative potential, while in the middle near the isoelectric point the suspension becomes unstable.

where R is the hydrodynamic radius, k_B is Boltzmann's constant, T is the absolute temperature, η is the dynamic viscosity, and D is the measured diffusion coefficient.

Two strategies for experimentally measuring the diffusion coefficient are dynamic light scattering (DLS) and nanoparticle tracking analysis (NTA). Instruments employing both these methods with data analysis software are commercially available.

In DLS, light is focused into a small volume of the sample suspension, and the scattering signal at a fixed angle is measured using a photodetector. As the particles in the scattering volume undergo diffusion, the magnitude of this scattered light signal changes in time. By computing the intensity time autocorrelation function of the scattered light signal and applying statistical mechani-

cal relations and system calibrations, the diffusion coefficient can be computed from the autocorrelation function signal, if some assumptions about the sample are made. This procedure becomes more complicated for polydisperse and highly concentrated samples, but methods have been developed for treating these cases [46].

In NTA, the particles flow through a cell where they are illuminated by a light sheet [47]. As the particles move through this light sheet, they scatter light, which is collected through a microscope objective and imaged with a camera. The position of each particle is tracked in time through analysis of this scattered light video, and the bulk convective motion is subtracted, leaving only the displacement due to diffusion. From this, the mean-square displacement of each particle is computed, which is used to calculate the measured diffusion coefficient:

$$D = \frac{MSD(R, \Delta t)}{2\Delta t} \tag{1.2}$$

where $MSD(R, \Delta t)$ is the mean square displacement measured in the NTA experiment and Δt is the elapsed time during the particle track. The diffusion constant, D, is related to the particle size through the Stokes-Einstein relation (Eq. 1.1).

Figure 1.3 shows a comparison of DLS and NTA measurements made on nominally monodisperse gold nanoparticles in buffer using standard commercial instrumentation and software. Rigorous comparative studies [48] of DLS and NTA indicate that NTA provides superior performance in resolving multiple peaks in polydisperse samples. NTA is able to provide reasonably accurate sizing information even on particles such as sub-micrometer protein aggregates and extracellular vesicles down to about 70-90 nm that have little refractive in-

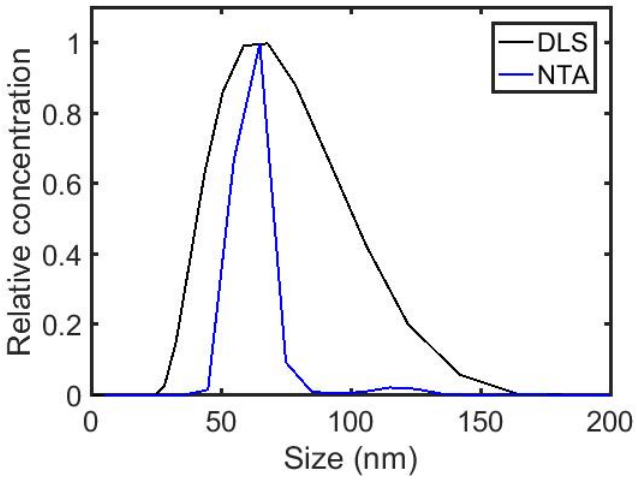

Figure 1.3: Comparison of DLS (black curve) and NTA (blue curve) measurements made on the same 50 nm nominal diameter gold nanoparticles suspended in 0.01x Phosphate Buffered Saline (PBS) buffer solution. DLS measurements were made using the Malvern Zetasizer Nano ZS, and NTA measurements were made using the Malvern NanoSight NS300. For reference, each curve is normalized by its peak value.

dex contrast with the fluid they are suspended in [49, 50]. Still, the presence of large, brightly scattering impurity particles and biases due to improperly accounting for drift can limit the accuracy of NTA measurements [48, 51]. While successive NTA measurements have been used to assess the stability of suspensions [49] under stresses including freeze-thaw cycles and mechanical stresses, this requires multiple measurements on the same samples over time, and is an observational rather than predictive technique.

Electron Microscopy

Another way of characterizing particle size is through electron microscopy. This method provides direct, geometric measurement of particle size, but relies on a dried and specially prepared sample, meaning that the results are not nec-

essarily representative of what happens in the native application environment for these particles. The extensive sample preparation and measurement time make this a low-throughput technique that is rarely used in quality assurance situations. Electron Microscopy is however used as a reference ground-truth benchmark for particle size, and the NIST-certified particle size standards used in some experiments here have been validated through Transmission Electron Microscopy (TEM) measurements.

1.3 Background on Near-field Optical Trapping

The nanoparticle characterization methods that I have developed in my doctoral research involve the use of optical trapping forces to hold and move nanoparticles near a surface. First pioneered by Ashkin [52, 53], optical trapping has been used for a number of fundamental and applied studies over the last few decades, particularly in the area of biophysics [54, 55]. This technique exploits the momentum transfer from electromagnetic fields to suspended particles, resulting in optical forces. These forces are typically decomposed as forces acting in the direction of the optical intensity gradient and forces due to optical scattering and absorption that act along the axis of optical propagation. In the most commonly implemented optical trapping configuration, often referred to as the free-space optical tweezer, laser light is focused through a high numerical aperture lens to a diffraction limited spot, where the particle of interest is held due to the optical gradient force:

$$F_{grad} = \frac{2\pi\alpha}{c}\nabla I \tag{1.3}$$

where F_{grad} is the optical gradient force, α is the optical polarizability, c is the speed of light, and ∇I is the optical intensity gradient. As α is proportional to the particle volume, exerting sufficient forces to overcome Brownian motion and stably trap smaller particles becomes much harder as particle size is decreased, and requires the generation of a large intensity gradient. As the laser focus spot size is limited by diffraction, this spot cannot be made arbitrarily small, and so increased peak optical power is necessary to trap smaller particles. In practice, these high optical powers can damage sensitive specimens and cause localized thermal effects which can influence experiments. As a result, researchers have looked to alternative approaches for engineering sharp optical gradients [56].

One way to generate a sharp gradient and therefore exert a large optical gradient force is to use a nanostructured device that confines light. This generates a region of high optical intensity, surrounded by evanescent zones where the intensity spatially decays exponentially, resulting very sharp intensity gradients. These sharp gradients exert large gradient forces (see Eq. 1.3), providing stronger and more stable optical traps than in the diffraction limited free-space optical tweezers. As these gradient forces are generated near the surface of the optical device through near-field effects, this is referred to as near-field optical trapping. By holding particles close to the surface of the device, near-field optical trapping provides a natural platform for measuring particle-surface interactions.

In Chapter 2, I will demonstrate the use of a device called a photonic crystal resonator to generate a near-field optical trap to probe particle-surface interactions. These devices have been demonstrated in the literature to provide significant improvements in optical trapping as compared to free-space optical traps,

and have been used for studies involving the trapping of sub-100 nm beads, single viruses, Wilson disease proteins, and λ DNA [57, 58, 59, 60]. Briefly, a photonic crystal resonator is an optical structure consisting of a gap or defect enclosed between photonic crystal mirrors. The photonic crystal mirrors are formed by alternating layers of material with different refractive indices arranged in a periodic structure. This periodic structure prevents the propagation of certain wavelengths of light, opening up a photonic bandgap. In the 1-D photonic crystal configurations used here, the periodic mirrors are formed by etching circular holes in a silicon nitride waveguide, providing alternating layers of silicon nitride (refractive index $n \approx 2$) and water ($n \approx 1.33$). In the center of the device there is a microcavity defect formed by having no hole [61]. Light at wavelengths that are forbidden from propagating through the mirrors forms standing waves in this central cavity that interfere constructively, satisfying the resonance condition. The superposition of these waves forms a "hot-spot" at the central cavity, creating a region of strong localized optical intensity which exponentially decays away from the center resulting in sharp gradients and large gradient forces in all three dimensions. Essentially, these structures confine light and trapped particles to a point.

In Chapters 3, 4, and 5, I demonstrate experiments using a different near-field optical trapping architecture. By guiding light through a single-mode waveguide, I relax a dimension of optical confinement from the photonic crystal configuration used in Chapter 2, and instead confine light along a line. This has the advantage of driving optical transport along the direction of optical propagation, thereby increasing the system throughput by measuring particles sequentially and simultaneously rather than one at a time. The trapping and transport of nanoparticles in the evanescent field of waveguides has been

developed previously in the literature and demonstrated for several different waveguide materials and particle types [62, 63, 64, 65, 66, 67, 68]. The transport is driven by propagation axis optical forces, typically decomposed into optical scattering and absorption forces. The optical scattering force, F_{scat} can be computed as

$$F_{scat} = \frac{8\pi\alpha^2\epsilon_m I}{3c\lambda^4} \tag{1.4}$$

where ϵ_m is the permittivity of the medium, λ is the optical wavelength, and I is the optical intensity incident on the particle. If the particle absorbs light at the wavelength used propagating in the optical trapping waveguide, this process will also transfer momentum to the particle, resulting in an absorption force, F_{abs}, which can be expressed as

$$F_{abs} = \frac{2\pi Im(\alpha)\epsilon_m I}{c\lambda} \tag{1.5}$$

where $Im(\alpha)$ is the imaginary part of the polarizability function. This arises from the complex permittivity of the absorbing particle, as α is a function of both permittivity and volume. These forces are balanced by the hydrodynamic drag on the particles, having the net effect of propelling the trapped particle along the top of the waveguide in the direction of the optical propagation at a terminal velocity. In the direction perpendicular to the waveguide surface, the optical field still decays evanescently from the surface as in the photonic crystal case, generating a strong optical gradient force described by Eq. 1.3. In Chapters 3, 4, and 5, I will describe studies to characterize nanoparticles using a waveguide near-field optical trap architecture. It is precisely the motion of the particle under the action of F_{scat} as described in Eq. 1.4 that enables the size sensitive motion used in Chapter 4 to characterize the sample polydispersity.

CHAPTER 2

NANOPHOTONIC FORCE MICROSCOPY: CHARACTERIZING PARTICLE-SURFACE INTERACTIONS USING NEAR-FIELD PHOTONICS

2.1 Abstract

Direct measurements of particle-surface interactions are important for characterizing the stability and behavior of colloidal and nanoparticle suspensions. Current techniques are limited in their ability to measure piconewton scale interaction forces on sub-micrometer particles due to signal detection limits and thermal noise. Here we present a new technique for making measurements in this regime which we refer to as Nanophotonic Force Microscopy. Using a photonic crystal resonator, we generate a strongly localized region of exponentially decaying, near-field, light that allows us to confine small particles close to a surface. From the statistical distribution of the light intensity scattered by the particle we are able to map out the potential well of the trap and directly quantify the repulsive force between the nanoparticle and the surface. As shown in the paper, our technique is not limited by thermal noise and therefore we are able to resolve interaction forces smaller than 1 pN on dielectric particles as small as 100 nm in diameter.

2.2 Introduction

The subtle balance of particle-particle and particle-surface force interactions that exist within nanoparticle and other colloidal suspensions plays a key role in determining long term stability. Generally speaking these interactions encompass a complex and dynamic combination of electrostatic forces[69], van der Waals interactions[70], hydrodynamic interactions[71], particle coating[72] and steric exclusion effects[73]. Stresses on stable suspensions, including changes in solution phase conditions such as ionic strength[74], pH, surfactant concentration[75] and temperature, can lead to particle aggregation[76], adsorption onto surfaces[77] and flocculation. To assess the risk of a suspension becoming unstable or the effectiveness of a preventative stabilizing measure, it is desirable to measure these interactions directly in the native solution environment.

The most common technique to directly measure particle-surface interactions is Atomic Force Microscopy (AFM). In what is known as the colloidal probe technique[21, 20], a particle of known size and surface composition is physically attached to a cantilevered beam which can then be moved close to the surface, allowing for the force to be measured at arbitrary particle-surface separation distances. Typically, the probes used are on the scale of $\sim$1-10 μm and the forces measured are on the order of nanonewtons[78]. Measurements made using colloidal AFM include studies on polymer bridging forces[25], van der Waals forces[24], depletion forces[26], and many others. While AFM has been used in low temperature and low pressure environments to make incredibly sensitive measurements of fundamental importance in physics and the life sciences[23], in colloidal environments the primary limitation of this technique

is thermal noise. To illustrate this limitation, consider a typical V-shaped cantilever used in colloidal probe experiments with a nominal stiffness K = 0.1 N/m. The expected root mean square displacement (See Equation 2.29 in Butt et al. [79]) of this cantilever due to thermal excitation at 298 K is about 0.17 nm; in other words forces smaller than 17 pN will result in deflections smaller than the thermal motion of this device. Indeed, practical colloidal AFM measurements report force resolutions of about 10-50 pN[27].

Another technique for measuring particle-surface interactions is Total Internal Reflection Microscopy (TIRM)[29]. First developed 30 years ago[28], this technique has been used to measure interactions in many physical systems, as highlighted by a recent review article[80]. Some notable examples include depletion interactions in polymer systems[81], specific ion effects[82], steric interactions[31], Casimir forces[32], and many others. As a statistical measurement based around the distribution of positions that a particle samples as it undergoes Brownian motion near a surface, unlike AFM, TIRM is not limited by thermal noise and is successful at measuring interactions with energies on the k_BT scale and forces smaller than 1 pN. However, previous studies performed using TIRM have been limited in their focus to dielectric particles with diameters on the micrometer scale or larger. This is due to several practical limitations that occur when working with smaller particles. The traditional method for making these measurements involves balancing the repulsive force of the particle-surface interaction with the weight of the particle itself. For smaller particles the gravitational contribution to the potential well is much weaker relative to k_BT so the particle does not stay near the surface. This has been addressed through the use of optical tweezers in TIRM[34] that limit the lateral diffusion of small particles through the application of optical gradient forces as well in-

fluence the range of particle-surface separation heights sampled through the application of radiation pressure forces. However, the diffraction limit of light restricts minimum spot size of the optical tweezers, meaning that more power is needed to generate the necessary optical gradients to hold smaller particles, which can be damaging to sensitive samples. Another approach to addressing this limitation in TIRM has been to confine nanoparticles close enough to the illuminated surface to make a measurement by introducing a second wall. Previous researchers have used silica nanoparticles as spacers to create very thin channels. This approach has allowed for TIRM measurements on gold nanoparticles with [37] and without[36] protein coatings as well as multiwall carbon nanotubes[38] in a confined region where the particles experience interaction potentials from both walls. As these metallic nanoparticles interact much more strongly with the evanescent field than dielectric particles of the same size, the scattered light signal is much stronger and is observable from gold particles as small as 100 nm. Generally, smaller particles scatter a much lower fraction of the available light, making scattering from these particles more difficult to discern from the background.

In this paper we present a technique that overcomes these limitations by using a photonic crystal resonator structure to confine light into a small area. This greatly increases the optical intensity at the surface and generates an optical gradient force[83]. In this near-field configuration[56] the optical force acts to pull particles closer to the surface. The sharp optical intensity gradients in the evanescent field generated by a resonator allow for much smaller particles to be trapped and analyzed than the conventional free-space optical-tweezer configuration[59]. Furthermore, due to the highly concentrated optical intensity on the surface, much more light is available for scattering by particles which

allows for signals from smaller particles to be detected.

2.3 Results and Discussion

Figure 2.1 shows a schematic illustration of the Nanophotonic Force Microscopy (NFM) method. As Figure 2.1a illustrates, a nanoparticle trapped in the evanescent field above a photonic crystal resonator will undergo a confined Brownian motion, scattering more light when it is close to the surface, and less when it is further away. As Figure 2.1b shows, the applied attractive optical gradient force balances the net particle-surface forces, resulting in an equilibrium position about which the particle undergoes Brownian fluctuations. For the case of strongly repulsive interactions (Fig. 2.1bi) this equilibrium is farther from the surface than for weaker repulsion (Fig. 2.1bii). Using the Boltzmann statistics, we obtain a map of the potential energy landscape that the particle interacts with from the distribution of scattered light intensities (Fig. 2.1ci and 2.1cii). By subtracting the optical component that we have applied and taking the derivative, we obtain the force-distance curve (Fig. 2.1ciii).

Figure 2.2 shows the procedure of the NFM data analysis technique. In this representative example measurement we are in a dilute solution of a 1:1 electrolyte (0.076 mM KCl, λ_D = 50 nm). Figure 2.2a shows the experimentally measured distribution of scattered light intensities. The particle will diffuse around equilibrium as it undergoes Brownian motion. Each position that the particle samples has an associated potential energy relative to equilibrium. As the available optical intensity exponentially decays away from the surface, each intensity state can be related to a position state using this exponential dependence. Fol-

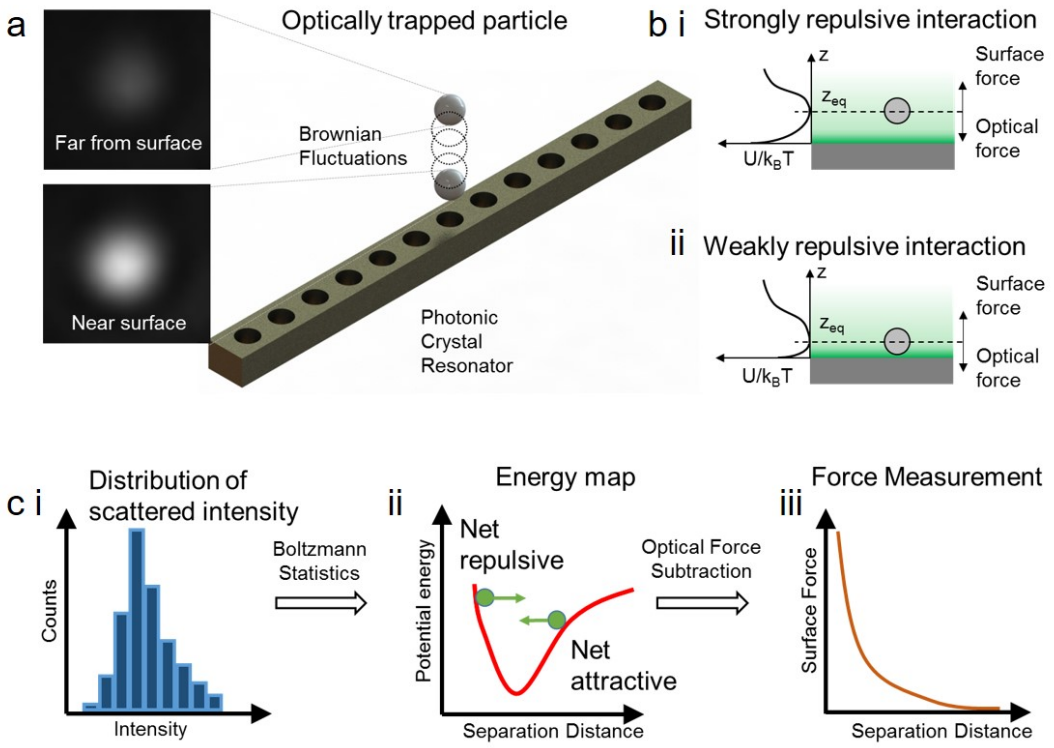

Figure 2.1: Overview of the Nanophotonic Force Microscopy setup and technique. a.) Light from a 1064 nm laser source is coupled into a photonic crystal resonator, creating a large optical intensity on the surface as well as a strong optical gradient force. As particles interact with the light in this evanescent field, they undergo Brownian motion, scattering more light when they are close to the surface. b.) The applied optical gradient force equilibrates the net effect of any surface forces. This equilibrium can be (i) farther from the surface if the interactions are strongly repulsive or (ii) closer if they are weakly repulsive. c.) i) Measuring the scattered light intensity at many times gives us the probability distribution of intensities. ii) Assuming that the probability of the particle occupying a given energy state follows the Boltzmann statistics, the potential energy landscape is mapped. iii) Subtracting the optical component of the energy landscape and taking the derivative gives us the force-distance curve for the particle-surface interaction.

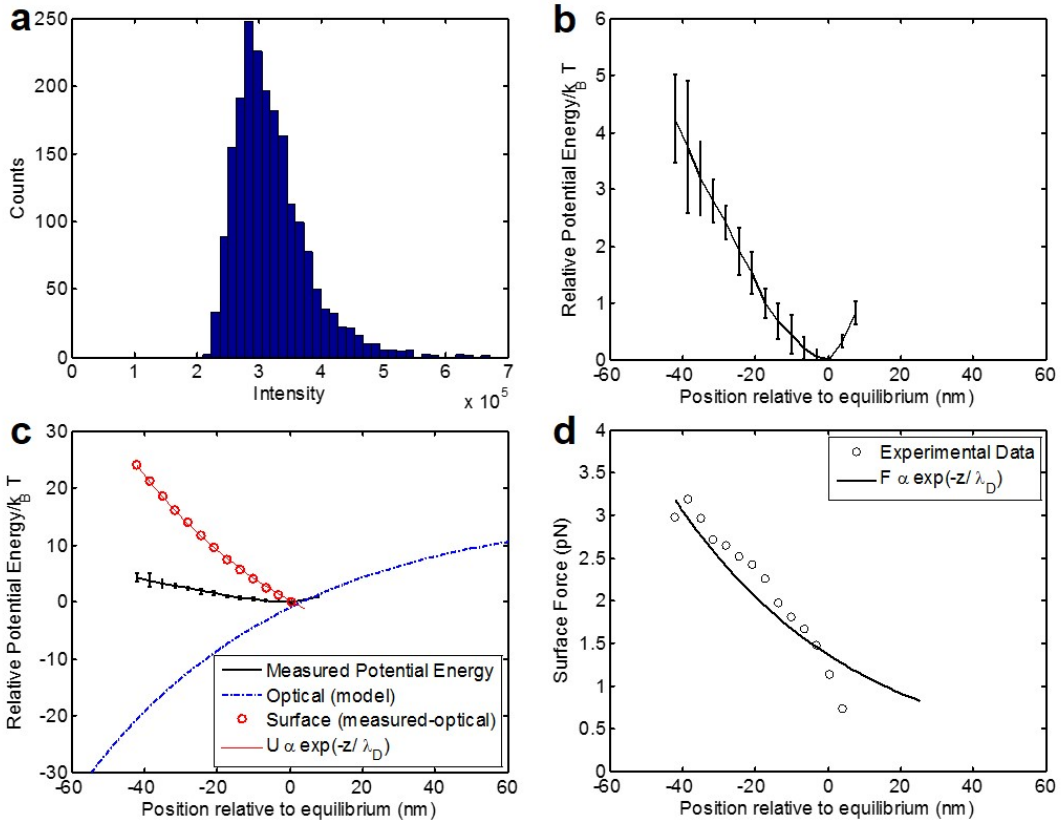

Figure 2.2: Summary and validation of the data analysis technique. Measurements performed on a 300 nm diameter polystyrene sphere in dilute KCl solution (λ_D = 50 nm). a.) Distribution of scattered light intensities for one representative measurement. b.) Potential Energy map derived using Boltzmann statistics from experimental scattered light distributions. The solid line indicates the average of N=5 independent measurements, error bars indicate standard deviations. c.) Subtraction of the optical component. The black solid lines indicate the experimental measured potential energy wells (average of N=4 data sets under constant experimental conditions, error bars indicate standard deviations). The blue dash-dot curves show the optical potential energy contribution calculated according to Eq. 2.2. The red open circles indicate the surface contribution as calculated by Eq. 2.1, while the red solid line indicates an exponentially decaying surface potential energy with 1/50 nm (1/ λ_D) decay constant as predicted from the electrostatic model. d.) Force vs. distance curve. The hollow circles represent the numerical derivative of the experimental data points on the dotted line in c. The solid line represents an exponentially decaying force with 1/50 nm ($1/\lambda_D$) decay constant.

lowing the procedure established in TIRM[84], we assume that the probability of finding the particle in a given intensity state follows the Boltzmann distribution, and use this to derive a map of the potential energy landscape, as shown in Figure 2.2b.

The key difference between our technique and TIRM is that in addition to the particle-surface interaction potential energy our measurement also includes the contribution from the optical field that we have applied. This means that in order to measure the particle-surface interaction we must correct for this. Symbolically,

$$U_{particle-surface} = U_{measured} - U_{optical}. \tag{2.1}$$

For a particle in the Rayleigh regime [85] (valid when $2\pi n_{med} a \ll \lambda$, where a is the particle radius, n_{med} is the refractive index of the surrounding medium and λ is the free-space wavelength of the incident light) $U_{optical}$ is provided by the well-known optical gradient force [53] and can be computed as [56]

$$U_{optical} = I_o \alpha \left(\frac{2\pi}{c}\right) exp\left(-\frac{z}{d}\right) \tag{2.2}$$

where I_o is the surface intensity, α is the polarizability of the particle, c is the speed of light, and d is the evanescent field penetration depth [64]. For a Rayleigh particle,

$$\alpha = \frac{3V(\epsilon_p - \epsilon_m)}{\epsilon_p + 2\epsilon_m} \tag{2.3}$$

where V is the particle volume, and ϵ_p and ϵ_m are the permittivity of the particle and medium respectively at the optical wavelengths used. For materials with low optical absorption we assume $\epsilon \approx n^2$ where n is the refractive index. Finite element simulations have confirmed that the optical force experienced by a 100 nm polystyrene sphere interacting with a photonic crystal resonator trap indeed follows this exponential decay[61]. Note that in practice since the length scale

of the evanescent field is often longer than the length scales associated with the surface forces, the exponential pre-factor can be obtained by a fit to the data in the region where $U_{optical} \gg U_{particle-surface}$. This means that our technique can be applied to situations where the Rayleigh point-dipole approximation is no longer valid, as long as the optical force is still proportional to the intensity gradient. This optical subtraction is shown in Figure 2.2c. Also, as the waveguide surface optical intensity is directly proportional to the optical power applied from the laser, the magnitude of optical component can be tuned allowing for the stable trapping of particles over a wide range of sizes.

The force exerted on the particle by the surface, $F_{particle-surface}$, can be computed from these interaction energies by

$$F_{particle-surface} = -\frac{dU_{particle-surface}}{dz} \tag{2.4}$$

where z is the spatial coordinate normal to the surface and $U_{particle-surface}$ is the particle-surface interaction potential energy. The hollow circles on Figure 2.2d represent this derivative applied numerically to our experimental data.

To validate our technique we seek to compare our measured force profile to a theoretical prediction. Most theoretical approaches for describing colloidal interactions come from the Derjaguin-Landau-Verway-Overbeek (DLVO) theory and its extensions [14]. While the DLVO theory fails to accurately describe many complex systems [16, 12], we look to simple limiting cases where we can expect the DLVO theory to make reasonable predictions. In the limit of a simple 1:1 electrolyte in a dilute solution relatively far from the surface, we expect that the van der Waals interactions should be negligible, and the electrostatic interactions can be approximated [84] as:

$$F_{particle-surface} = \frac{16\epsilon_m a}{\lambda_D}\left(\frac{k_B T}{q_e}\right)^2 tanh\left(\frac{q_e\psi_s}{4k_B T}\right) tanh\left(\frac{q_e\psi_p}{4k_B T}\right) e^{-\frac{z}{\lambda_D}} \tag{2.5}$$

Where ϵ_m is the DC permittivity of the medium, a is the radius, q_e is the charge of an electron, and ψ_p and ψ_s are the Stern potentials of the particle and the surface respectively, k_B is the Boltzmann constant, T is the absolute temperature, and λ_D is the Debye screening length. This weak overlap approximation is considered valid for surface potentials less than $\sim$100 mV [86]. In this limiting case, the surface force should decay exponentially with decay constant equal to $1/\lambda_D$, the Debye screening length. This curve is shown by the solid line in Figure 2.2d. Note that the decay constant used in this solid line is the Debye length calculated from the known experimental parameters and not a fit to the experimental data. To test whether the magnitude of our measured force is correct, we measured the ζ-potentials ($\sim \psi$ [14]) of 300 nm diameter polystyrene beads as well as the silicon nitride surfaces suspended in our experimental solution environment using laser-Doppler electrophoresis (Malvern Zetasizer Nano ZS, see also [87]), finding ζ_s = -43.8 mV and ζ_p = -54.2 mV. Using Equation 2.5, this gives a pre-exponential factor of 4.3 pN. As Figure 2.2d shows, our measurements offer reasonable agreement with this prediction.

To demonstrate our ability to measure different types of surfaces, in Figures 2.3 and 2.4 we compare the interaction potentials of polystyrene beads to fused silica beads. Both of these materials have different refractive indices, and have very different surface types. Both experiments shown here were performed in a buffered solution at the same pH and salt concentration. In 2.3a and 2.4a, we show the potential energy landscape, highlighting our ability to perform the optical subtraction for particles of different indices. We subtract the optical component using the known refractive indices of each particle at 1064 nm (n = 1.59 and n = 1.44 for polystyrene and silica respectively), which contribute to the polarizibility α in Equation 2.3. Taking the derivative of the resulting sur-

face potential energy (as in Eq. 2.4), we are able to distinguish the different force profiles for each case, as shown for polystyrene and silica in 2.3b and 2.4b respectively. In these plots, we show both the numerical derivative of the surface potential energy data points (open circles) as well as the computed analytical derivative of exponential fits of the surface potential energy. We attribute the greater measured forces for the silica beads to greater surface charge[88]. As can be seen the measured interaction energies are on the order of a few k_BT while the measured forces are on the pN scale.

One major advantage of our technique over conventional TIRM implementations is that by using a photonic crystal resonator we are able to create a large surface light intensity, and a strong optical gradient force capable of holding very small particles near the surface. This allows us to measure our particles for long enough times to acquire thousands of scattered light images, allowing us to make a good statistical measurement. This also means that more light is available to be scattered by particles, allowing for observable signals to be measured even from very small dielectric particles with low refractive index contrast from the medium that would give too dim of a signal to otherwise be measured. In Figure 2.5, we show our experiments with 100 nm diameter polystyrene beads in high and low salt concentrations. Here we again see the expected result of stronger electrostatic repulsive forces in the case where the salt concentration is lower and there are fewer ions to screen the surface charges. In the lower salt experiments shown in Figure 2.5a, we find that the force decays with an exponential decay constant of 1/7.1 nm, in good agreement with the known Debye length for this solution of 7.58 nm. As we move to higher biologically relevant salt concentrations, as shown in Figure 2.5b, we experimentally measure decay constants that are no longer equal to $1/\lambda_D$. This can likely be at least partially

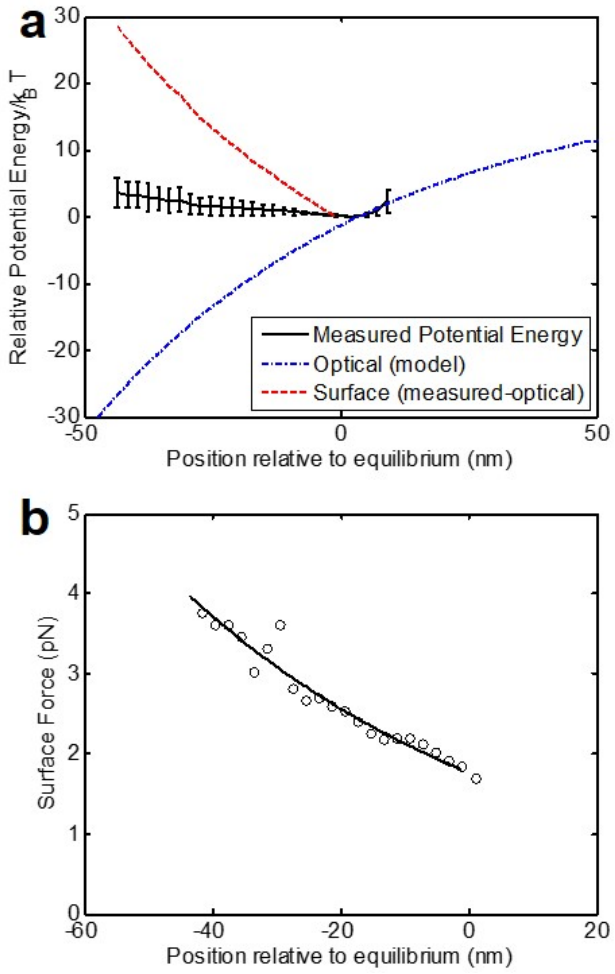

Figure 2.3: Measurements on polystyrene spheres (300 nm diameter, refractive index n = 1.59). Experiments performed in 0.01x PBS (λ_D = 7.58 nm), N=5 independent measurements. a.) Measured potential energy map showing subtraction of the optical component for polystyrene. Black line with error bars indicates the experimental measurement. The blue dash-dot curve indicates the model for the optical contribution. The red curve (shifted vertically for clarity) represents the surface component following subtraction. b). Force curves for polystyrene. Solid lines indicate derivatives of fitted curves to the surface contribution to the potential energy calculated using Eqs. 2.1 and 2.4. Hollow circles indicate numerical derivatives of the unfitted experimental data.

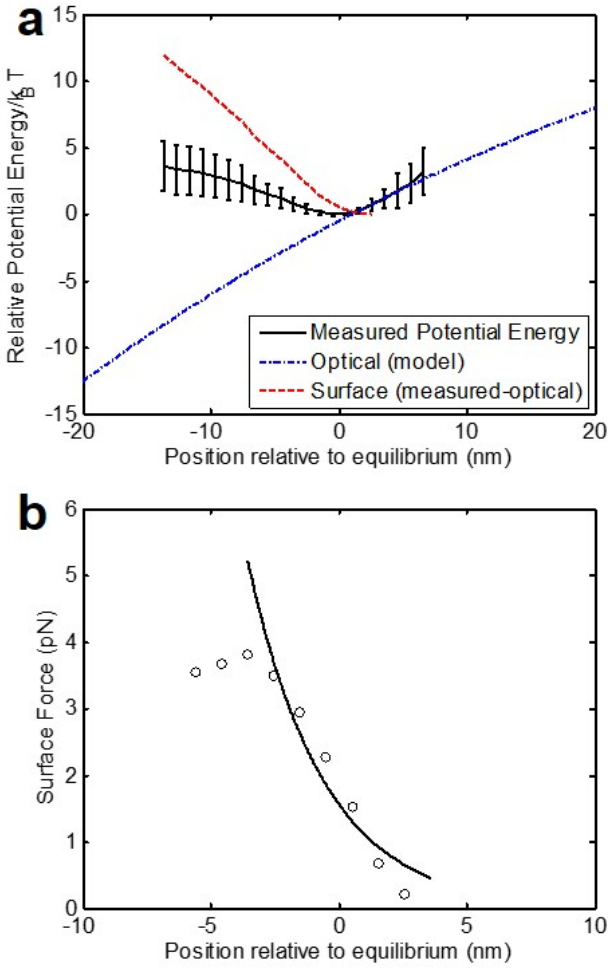

Figure 2.4: Measurements on silica spheres (310 nm diameter, n = 1.44). Experiments performed in 0.01x PBS (λ_D = 7.58 nm), N=5 independent measurements. a.) Measured potential energy map showing subtraction of the optical component for silica. Black line with error bars indicates the experimental measurement. The blue dash-dot curve indicates the model for the optical contribution. The red curve (shifted vertically for clarity) represents the surface component following subtraction. b). Force curves for silica. Solid lines indicate derivatives of fitted curves to the surface contribution to the potential energy calculated using Eqs. 2.1 and 2.4. Hollow circles indicate numerical derivatives of the unfitted experimental data.

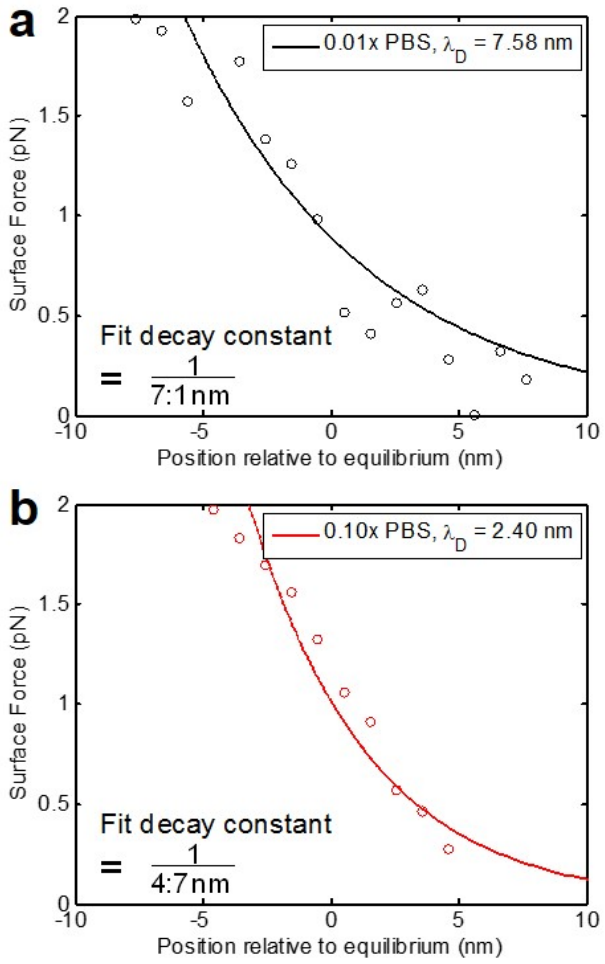

Figure 2.5: Effect of changing salt concentrations. Data are for 100 nm polystyrene spheres in a.) 0.01x Phosphate Buffered Saline (PBS) solution, λ_D = 7.58 nm and b.) 0.1x PBS, λ_D = 2.40 nm. Solid lines indicate derivatives of fitted curves to the surface contribution to the potential energy calculated using 2.1 and 2.4. Hollow circles indicate numerical derivatives of the unfitted experimental data averaged for N=4 (a.) and N=7 (b.) independent measurements at each salt concentration respectively.

explained by ion-ion correlations and other finite ion size effects as the calculated screening lengths approach the hydrated ion sizes [89]. As shown in the figure, we are able to measure forces smaller than 1 pN. This force regime is inaccessible to AFM due to thermal noise limitations.

We have established the application of our technique to dielectric spheres with diameters ranging from 100-310 nm. In general, any particle that can be optically trapped by our devices will scatter light. Previous and concurrent studies have demonstrated the trapping of polystyrene beads as small as 22 nm, quantum dots, various proteins [59], and DNA[58], as well as scattered light measurements on influenza viruses [60]. An upper bound to the magnitude of forces that can be measured is the necessity of applying a large input optical power in order to generate a large optical gradient force to balance them. While previous studies have shown that silicon nitride photonic crystal traps operating with 1064 nm light generate much less heat than conventional free space optical tweezers [59], some sensitive samples can be damaged by very high optical powers [90]. One major limitation of our technique is that the throughput is low. Because it is necessary to have only one particle interacting with the resonator at a time in order to obtain accurate measurements, our experiments have used low particle concentrations, and as a result the time spent waiting between measurements is much longer than the measurement time itself. Going forward, this technique can be applied to additional surfaces through the immobilization of macromolecules on the resonator surfaces as well as the deposition of thin dielectric films. Previous work in photonic crystal biosensors has demonstrated the immobilization of proteins on photonic crystal resonator devices similar to the ones used in this work [57], and we expect that similar procedures could be used to apply NFM to study interactions between particles and adsorbed macromolecules.

2.4 Conclusions

In conclusion, we have demonstrated a technique capable of making direct measurements of particle-surface interaction potentials and forces. Our technique excels at measuring small particles and small forces in a regime previously inaccessible using conventional TIRM implementations and colloidal-probe AFM. By engineering photonic crystal structures capable of confining and concentrating light, we are able to detect scattered light from dielectric particles with diameters as small as 100 nm. This is important since many colloidal products rely on particles in this range. In the limits of a simplified system, we recover the predictions of the DLVO theory, validating our technique. However, our technique makes no assumptions about the physical mechanisms that generate the forces we are measuring; we are able to measure arbitrary forces and combinations of forces in a complex physical system.

2.5 Methods

2.5.1 Optical and Fluidic Setup

The experimental setup for our Nanophotonic Force Microscopy (NFM) system consists of photonic crystal devices integrated into a microfluidic channel. In this work we use silicon nitride devices. Light from a 1064 nm wavelength diode laser (LU1064M400, Lumics, El Segundo, CA) is coupled into a single mode optical fiber with a tapered lensed tip (Oz Optics, TSNJ-3A-1064-6/125-0.25-18-2.5-12-3). This tip is brought into contact with the chip where a tapered

input waveguide is used to couple the light into the device. The light is then guided through the waveguide to the photonic crystal resonator. A microfluidic channel is integrated on top of the photonic layer, and used to transport suspended particles to the resonator, where they interact with the evanescent field. Additional experiments confirming the results presented here were performed using the Optofluidics NanoTweezer system (Optofluidics Inc., Philadelphia, PA).

The operating principles of photonic crystal resonator optical traps and procedures for designing them are detailed elsewhere in the literature37. In this work, we use the same devices as in our previous paper [60] which were designed using Finite Difference Time Domain (FDTD) simulations (Lumerical FDTD Solutions package). Briefly, a set of holes in a silicon nitride waveguide form a structure with a periodically varying refractive index. This structure forms standing waves when excited by wavelengths that satisfy its resonance condition. A defect is added by having no hole at the center of this structure. This configuration is referred to as the microcavity design in the previous literature [61]. Here the superposition of the evanescent tails of the standing waves forms a hot-spot with a strong local optical intensity, which exponentially decays away from the surface, resulting in a strong optical gradient force.

The microfluidic channels are fabricated from parafilm cut using a CO_2 laser (VersaLaser VLS3.50). The parafilm is bonded between the chip and a glass microscope coverslide with holes for the inlet and outlet also patterned using the CO_2 laser by heating on a hotplate at 140$^{\circ}C$. Punched PDMS is bonded to the glass at the inlet and outlet. Tygon tubing is used to deliver fluid into the channel from a syringe pump (New Era Pump Systems, Inc. NE-1000, Farmingdale,

NY).

2.5.2 Imaging and Analysis

The scattered light is imaged using a CCD camera (Hamamatsu ORCA-ER CCD). Imaging is accomplished using a 40x microscopy objective (Olympus LUCPlanFL N, 0.60, ∞/0-2/FN22, UIS2). To optimize the imaging, the shortest possible exposure times (10-100 μs) are used. For particles that scatter enough light to saturate the images with this exposure time, imaging was optimized with Thorlabs Premium Bandpass (FLH1064-8) and Brightline Bandpass filters (FF01-641/75-25, FF02-628/40-25) which allow 90%, 2.6% and 0.2% transmission at 1064nm respectively. Images were recorded with 16-bit pixel depth. For each particle 2000-5000 images were captured to build a statistically valid distribution. A limited region of interest was used to optimize data transfer, allowing for image acquisition at a rate of $\sim$59 frames per second. As a result, data acquisition from an experiment consisting of 5000 images was accomplished in less than 90 seconds. Once acquired, images were cropped to include only the scattered light from the particle, and integrated using ImageJ.

2.5.3 Solution Conditions and Sample Preparation

Salt concentrations were achieved by diluting Phosphate Buffered Saline (Gibco, 10x concentrate, P5493 pH 7.2) in filtered deionized water. The experiments in KCl were performed by preparing a solution of 0.076 mM KCl in filtered deionized water. Samples of 100 nm and 300 nm diameter polystyrene spheres (Bangs

Labs PS02N and ThermoScientific Fluoromax 09-980-464) and 310 nm diameter silica spheres (Bangs Labs SS02N) were prepared by diluting the samples in the desired solution environment by an amount necessary to create a mean distance between particles on the order of tens of m. Working at too high of a concentration increases the risk of having multiple particles interact with the resonator simultaneously, while working at low concentrations lengthens the wait time for particle interactions to occur. Experimental concentrations of $\sim$100-200 particles/μm^3 for the 100 nm particles and $\sim$1-10 particles/μm^3 for the 300 nm and 310 nm particles resulted in typical wait times in the range of ten minutes to one hour. Dilutions were typically accomplished in 2 stages, with each stage sonicated for 5-10 minutes to prevent particle aggregation. Clean tygon tubing was used in each experiment. In between experiments the parafilm microfluidic channels were removed and the chips were soaked in Nanostrip (Cyantek) for 12-24 hours to clean the surfaces.

CHAPTER 3

NEAR-FIELD LIGHT SCATTERING TECHNIQUES FOR MEASURING NANOPARTICLE-SURFACE INTERACTION ENERGIES AND FORCES

Adapted with Permission from Perry Schein, Colby K Ashcroft, Dakota ODell, Ian S Adam, Brian DiPaolo, Manit Sabharwal, Ce Shi, Robert Hart, Christopher Earhart, and David Erickson, "Near-Field Light Scattering Techniques for Measuring Nanoparticle-Surface Interaction Energies and Forces," Journal of Lightwave Technology, 33(16), 3494-3502, 2015.

3.1 Abstract

Nanoparticles are quickly becoming commonplace in many commercial and industrial products, ranging from cosmetics to pharmaceuticals to medical diagnostics. Predicting the stability of the engineered nanoparticles within these products a priori remains an important and difficult challenge. Here we describe our techniques for measuring the mechanical interactions between nanoparticles and surfaces using near-field light scattering. Particle-surface interfacial forces are measured by optically pushing a particle against a reference surface and observing its motion using scattered near-field light. Unlike atomic force microscopy, this technique is not limited by thermal noise, but instead takes advantage of it. The integrated waveguide and microfluidic architecture allow for high-throughput measurements of about 1000 particles per hour. We characterize the reproducibility of and experimental uncertainty in the measurements made using the NanoTweezer surface instrument. We report surface interaction studies on gold nanoparticles with 50 nm diameters, smaller than

previously reported in the literature using similar techniques.

3.2 Introduction

Nanoparticles represent the largest commercialization of nanotechnology [91, 92, 93, 94, 95, 96] with applications in medicine, electronics, batteries and household products, to name a few. Despite the recent manufacturing advances that enable synthesis of a large variety of nanoparticles, there remain significant measurement challenges. In biomedical applications, nanoparticles are often highly reactive, display complicated size-dependent interfacial properties and are applied in complex biological systems with often unclear and ambiguous results [97, 13, 98, 99]. Specifically, the vastly increased surface area and high surface energy of nanoparticle dispersions result in performance that is strongly mediated by surface interactions, and there is a pressing demand for improved nanoparticle surface analysis [97, 100, 101, 102, 103, 104, 105, 106]. The surface of a nanoparticle is a key determinant of its properties and performance, and the synthesis of nanoparticle dispersions almost always utilizes surface treatment or coating to yield dispersions with both chemical and colloidal stability [100, 107, 108].

In practice, nanoparticle suspensions are incredibly complicated and their behavior is difficult to theoretically predict. Most theoretical approaches begin with the Derjaguin-Landau-Verway-Overbeek (DLVO) theory. The basic premise of the DLVO theory is the summation of effects due to the electrostatic and van der Waals interactions. This theory has been extended to account for many additional effects, typically by adding an additional potential energy term

to the summation [14]. While these descriptions have some success in describing simple systems, the theory breaks down in describing more complicated situations [16]. This is particularly true at biological salt concentrations [12].

Due to these shortcomings, predicting the behavior of a realistic engineered suspension from first principles remains a daunting proposition. Yet, evaluating the surface properties and predicting long-term stability is not possible with current commercial techniques [103, 108, 109, 110]. A variety of authors [97, 100, 101, 102, 103] and regulatory agencies [111, 112] have specifically cited the need for improved methods to analyze nanoparticle surfaces.

Here we describe our waveguide-based method for making direct measurements of particle-surface interactions. We detail the theoretical background of how the potential energy landscape is determined from measurements of scattered light intensity. We then discuss the waveguide architecture which brings this technique into a new regime of high-throughput nanoparticle characterization on samples with diameters as small as 50 nm. We present new data with this high-throughput technique and characterize the reproducibility and uncertainty in measurements made using this method.

3.3 Background

To gain practical insights into colloidal behavior it is useful to measure the net colloidal forces directly in the native solution. One technique for doing this is Atomic Force Microscopy (AFM) with a colloidal probe. In this technique the colloidal particle of interest is physically attached to a cantilever. As the probe is brought close to a surface, the surface forces cause the device to deflect, which

can be calibrated to give the displacement of the cantilever. Independently developed by Butt [21] and Ducker in 1991 [20], colloidal probe AFM has proved useful in the study of many physical phenomena. However, in a colloidal environment thermal noise will actuate the cantilever; deflections will be observed even in the absence of an interacting surface. This fact is commonly used to empirically measure the stiffness of the probe using the equipartition theorem [79]. The implication of this is that AFM is not a suitable technique for studying interactions on the k_BT scale. Considering the stiffness of typical cantilevers used, surface forces smaller than approximately 10-50 pN will cause displacements smaller than the thermal motion of the device. Typical studies with colloidal probe AFM use micrometer scale probes and measure forces in the nN range [78]. Additionally, colloidal AFM suffers from low-throughput.

Another approach to studying particle-surface interactions is to illuminate the surface by guiding light through it. In this configuration, an evanescent field is generated at the interface between the surface and the aqueous suspension. The intensity of light in this evanescent field decays exponentially in the direction normal to the surface. Particles interacting with this evanescent field will scatter light; this scattered light is measured in order to gain information about the particles. The first implementations of this concept involved the use of a dielectric slab, typically a glass microscope slide into which laser light was coupled at an angle beyond the critical angle to generate the evanescent wave. First developed by Prieve [28, 29] and coworkers, this technique is called Total Internal Reflection Microscopy [84] (TIRM).

Briefly, this technique works by noting that the amount of light scattered by a particle depends on its position in the evanescent field, as the optical intensity

is a function of distance from the surface. This means that particles scatter more light when they are near the surface than when they are further away. The distribution of the scattered light intensities is related to the distribution of particle positions as it undergoes confined Brownian motion near the surface. Therefore, the probability of finding the particle scattering at a given intensity corresponds to the potential energy associated with that state as described by the Boltzmann statistics. In this way, the potential energy well is mapped. By making statistical measurements that essentially examine the confined Brownian motion of a particle, these light scattering techniques are not limited by thermal noise and are capable of resolving sub-pN forces.

The TIRM technique has given researchers insight into many colloidal phenomena, including polymer and macromolecular mediated depletion interactions [31] and has enabled fundamental studies of the Casimir force [32] and non-equilibrium statistical mechanics [33]. However, the classical TIRM implementation has limitations when applied to smaller particles. Smaller particles scatter much less light, so the signal-to-noise ratio decreases with decreasing size. Smaller particles also diffuse faster, greatly reducing the probability of finding them near a scattering surface for enough time to make a good measurement. In the initial TIRM studies the gravitational settling of the particles was sufficient to balance the electrostatic forces. This quickly becomes insufficient for particles in the single micrometer and smaller regime. One approach for addressing this in the TIRM literature is the use of free space optical tweezers to force particles close to the surface with radiation pressure forces, which improves the ability to measure micrometer scale dielectric particles [34]. Another approach is to introduce a second surface located several hundred nanometers above the scattering surface to physically force particles into the evanes-

cent field. Using this technique, researchers have been able to measure metallic particles such as 100 nm gold spheres [36, 37] and multi-walled carbon nanotubes [38], which interact much more strongly with the evanescent field than dielectrics [40].

Recently we have explored a different strategy, illustrated in Fig. 3.1, for bringing near-field light scattering techniques to the nanoparticle regime. Unlike the slab approach used in TIRM, which confines light only in one dimension, our technique relies on additional confinement of the light using a waveguide. This has the dual benefits of increasing the local optical intensity at the scattering surface, thereby increasing the signal, and introducing an attractive optical gradient force, which pulls particles close to the surface in a predictable way, increasing confinement. In the previous chapter, we introduced the Nanophotonic Force Microscopy (NFM) technique with light confinement in three dimensions using a photonic crystal resonator and demonstrated the ability to measure 100 nm dielectric particles. However, this one particle at a time approach has limited throughput.

In this chapter, we use a waveguide structure which confines light as well as interacting particles in two dimensions, taking advantage of both the increased signal and particle confinement offered by NFM while allowing many particles to be interrogated in rapid succession, greatly increasing throughput. Optical waveguides have previously been used in a variety of sensing and measurement applications including absorbance and Raman spectroscopy for particle identification and chemical sensing [113, 114, 115] as well as particle and cell sorting and manipulation [66]. This architecture is well-suited for high-throughput measurements because the optical scattering force propels [65, 116] nanoparti-

cles along the waveguide in the optical propagation direction [56]. This can be expressed as:

$$F_{scat} = \frac{8\pi^3 I \alpha^2 \epsilon_m}{3c\lambda^4} \tag{3.1}$$

where I is the optical intensity, α is the polarizability, ϵ_m is the permittivity of the medium, c is the speed of light, and λ is the optical wavelength. In general there can also be an additional force in this direction due to optical absorption. These forces are balanced by the Stokes drag force:

$$F_{drag} = 6\pi\eta R u \tag{3.2}$$

where R is the particle radius, η is the dynamic viscosity of the medium, and the particles travel down the waveguide with velocity u. Rather than waiting to load one particle at a time into a central resonator hot-spot, particles are measured as they continuously move down the waveguide in the direction of optical propagation.

3.4 Technique Overview

Briefly, our technique works by pushing particles against a waveguide surface, taking advantage of the optical trapping force provided by the light confinement. The particles experience this force as well as the net effect of the surface forces and undergo confined Brownian motion near the surface. The optical intensity in the evanescent field depends exponentially on the distance to the surface, so diffusing particles scatter more light when they sample positions near the surface and less light at times when they are further away. By observing the scattered light from a particle at many times we build up a histogram giving us the probability of finding a particle in a given state, and use the Boltzmann

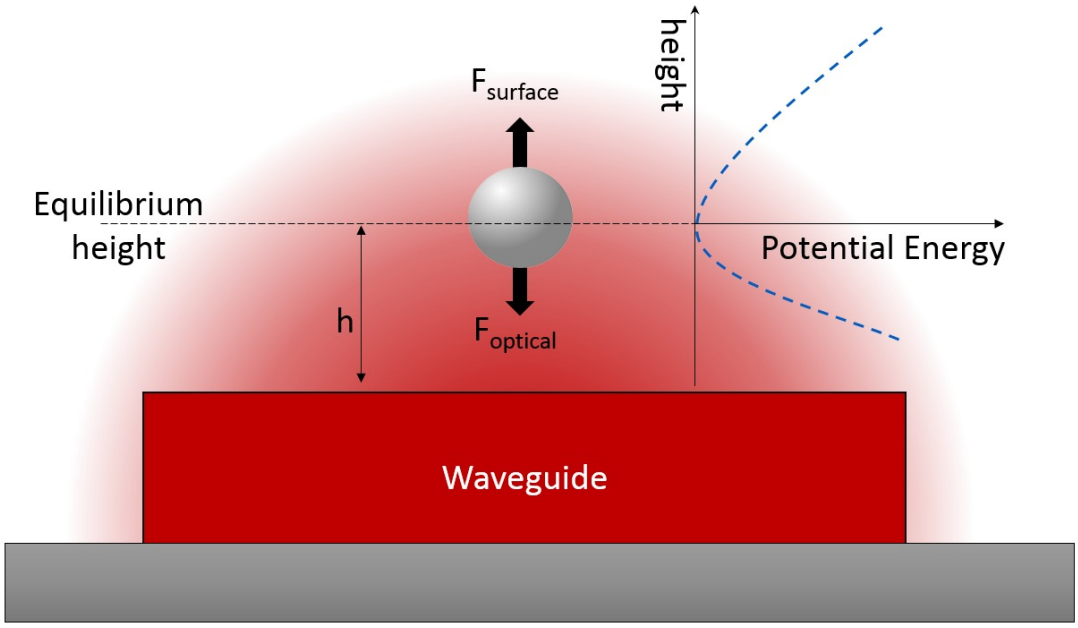

Figure 3.1: Nanophotonic force microscopy using a waveguide structure. Nanoparticles are trapped and illuminated by the waveguides evanescent field. The optical intensity in the evanescent field decays exponentially away from the surface. The particle position fluctuates due to thermal energy about an equilibrium position determined by the optical and surface forces present. The height-dependent scattered intensity allows for mapping of the particle height distribution, from which the potential energy landscape is calculated.

statistics to deduce the potential energy landscape from this probability distribution. Since we know the contribution provided by the optical trap, we can subtract this component, leaving us with the particle-surface interaction, giving insight into the behavior of the system.

Fundamentally, in order to make measurements that are not thermal noise limited one must rely on a technique that accounts for the thermal motion of the particle. In other words, since we are working in liquid environments, the

solvent molecules will have thermal energy and will collide with the nanoparticle, transferring some of their energy. This will result in the particle undergoing Brownian motion. A particle near a surface will experience a variety of forces, many of which depend on the particle-surface separation distance. Therefore, this motion will be biased and the particle position will fluctuate about some equilibrium position at which these forces are balanced and the net force on the particle is zero. However, as the particle is pushed away from equilibrium, it will experience a net restoring force due to moving into a region where the forces are not balanced. In the experiments that we present in this paper the dominant forces are a repulsive electrostatic force balanced by an attractive optical gradient force, but the method is generally applicable to the case of other forces.

In energetic terms, as these collisions push a particle away from equilibrium the work done in displacing the particle gives it some potential energy. As the particle moves to a new state, it scatters a different amount of light, which is recorded in the next camera frame. In the limiting case where many observations are made (the question of how many observations are necessary in practice is addressed later in this chapter) the distribution of intensity states observed corresponds to the probability distribution of finding the particle in a given intensity state. Following the arguments used in the TIRM literature [34, 80], these intensity states follow the Boltzmann distribution [117]:

$$P(state1) \propto e^{\frac{-U(State1)}{k_B T}} \tag{3.3}$$

where $P(state1)$ represents the probability of finding the particle in a given state, $U(state1)$ is the associated energy of that state, k_B is the Boltzmann constant and T is the absolute temperature. Note that this refers to the probability of finding the particle scattering with a given intensity, the quantity that we

measure in the experiment. However, we are interested in the probability of finding the particle at a given separation distance from the surface, and in mapping the potential energy landscape as a function of this separation distance. To make this conversion these probability distributions are related by the Jacobian matrix, which in this case this can be stated as:

$$P(z) = P(I(z))\frac{dI(z)}{dz} \tag{3.4}$$

where $P(z)$ is the probability distribution of finding the particle at height z, $P(I(z))$ is the measured probability distribution of the particle scattering intensity I, and the Jacobian is the derivative of this intensity with respect to the spatial coordinate normal to the surface. We know that the field is evanescent in nature, so we can expect the intensity to decay exponentially:

$$I(z) = I_o e^{-\frac{z}{d}} \tag{3.5}$$

where d is the evanescent field penetration depth and I_o is the surface optical intensity, so combining these equations we get

$$\frac{U(z) - U(z_{eq})}{k_B T} = ln\left[\frac{P(I(z_{eq}))I(z_{eq})}{P(I(z))I(z)}\right] \tag{3.6}$$

where z_{eq} is the equilibrium separation distance. This procedure is known as the Boltzmann inversion- by "inverting" the Boltzmann distribution that we measure, we map out the energy difference between the states. The most probable state is the equilibrium state, so by comparing all other states to the equilibrium we obtain a map of the potential energy, normalized by $k_B T$, as a function of the distance from equilibrium. The only assumptions made up to this point are that the optical field is exponentially decaying in the direction normal to the scattering surface and that the probability of finding the particle in a given state follows the Boltzmann distribution. For the types of structures used here, finite

element simulations indeed verify the exponential dependence of the evanescent field [61]. More generally, previous work in TIRM has established methods of accounting for fields that do not exactly follow this dependence or where multiple scattering events between the particle and the surface need to be accounted for [118].

In practice, our technique works by intentionally generating an attractive optical gradient potential well to pull the particle close to the surface. While this is useful in that it confines the particle close to the surface, the potential energy well that we map includes both the interactions that we are interested in characterizing and a contribution from the optical gradient that we have applied in order to make the measurement. The magnitude of this optical contribution depends on both the polarizability of the particle and the surface optical intensity, which can be adjusted by tuning the input laser power. To account for this we assume that the optical contribution can be completely decoupled from the other interactions. The justification for this assumption is that the optical frequencies used are in the terahertz range, meaning that the timescales of the electromagnetic oscillations are much faster than the timescales associated with ions reforming electrical double layers [119]. We can write out this subtraction symbolically:

$$U_{int} = U_{tot} - U_{opt} \tag{3.7}$$

where U_{int} is the potential energy of the particle-surface interaction, U_{tot} is the total measured potential energy landscape and U_{opt} is the optical component. Fortunately, the optical gradient force is well understood and can be computed based on material and system parameters. For particles in the Rayleigh regime, where the particle size is small relative to the wavelength, the Rayleigh gradient

force can be integrated giving us [56]:

$$U_{opt} = \frac{2\pi}{c}\alpha I_o e^{-\frac{z}{d}} \tag{3.8}$$

where c is the speed of light and α is the polarizability. Note that Eq. 3.8 can be generalized for both metallic and dielectric Rayleigh particles [40]. Theory and experiments have confirmed these models for free-space optical tweezers [83, 53, 85], and the applicability of these models to near-field interactions has also been extensively established through theory [64] and simulations [61]. For larger particles where the Rayleigh approximation does not hold, the magnitude of the scattered light will not increase monotonically with size owing to morphology dependent resonances. A full solution to Maxwells equations is needed, and this is typically accomplished numerically. Even so, the optical gradient itself is unchanged, so the force will still decay exponentially with decay constant determined by the known evanescent field penetration depth. In practice, this means that as long as there are enough data points in the region where the optical effects dominate the surface effects, the optical component can be determined by fitting the data with an exponential function, and this can be subtracted giving the surface force.

We expect the primary component of the particle-surface interaction to be due to the electrostatic repulsion in the overlapping electrical double layers of the particle and the surface. According to the DLVO theory, the component from the screened electrostatic interactions, U_{es}, has the form of a decaying exponential:

$$U_{es} = Ae^{-\frac{z}{\lambda_D}} \tag{3.9}$$

where z is the coordinate normal to the surface, λ_D is the Debye screening length, and A is a coefficient depending on material properties and solution

conditions.

3.5 Overview of the High-Throughput System

3.5.1 NanoTweezer Surface

The NanoTweezer Surface instrument consists of opto-fluidic microchips that enable manipulation, as well as visualization and measurements of nanoparticles with an accompanying microscope and CMOS camera. The system is composed of an instrument (∼400 mW 1064 nm laser, regulated pneumatic pump for fluid flow, and associated electronics and optics), a microscope mount, and cassettes that house microfluidic chips with photonic waveguide structures (Fig. 3.2). Laser power, sample flow rate, and imaging acquisition conditions are controlled by a custom software suite.

NanoTweezer chips contain nanostructured Si_3N_4 waveguides with a rectangular cross section of 250 x 600 nm (HxW). Waveguide patterns are defined by e-beam lithography and fabricated using standard nanofabrication techniques. The waveguide is cladded by SiO_2 films (8 μm thickness above and 3 μm below) across the chip with the exception of the experimental window, in which the waveguide is exposed to the fluid sample.

Each chip contains three waveguides which are coupled to optical fibers on the edge facet of the chip (Fig. 3.3). 1064 nm laser light (TE mode polarized) is supplied by the instrument laser, coupled to the waveguides by the pre-aligned optical fibers, and guided to the waveguide outputs where optical power is

measured with a photodiode.

A sample is introduced by inserting an aspirator into the solution of interest. The sample is drawn through the system with vacuum pressure and ultimately collected in a waste reservoir. Vacuum pressure is regulated in the range of 0 to 70 mBar, and can be increased to $\sim$300 mBar for rapid sample loading and washing. Precise flow rate control in the range of 0-7 μl/min is achieved by using an in-line flow rate sensor and a PID feedback control loop. Upon introduction of a sample at flow rates below 7 μl/min, particles passing by the waveguide are trapped by the evanescent field and propelled along the waveguide by optical scattering forces. This movement enables continuous imaging of particles as they travel along the waveguide and pass through the imaging region of interest. The intense scattering generated by particles enables high signal to noise imaging at low (¡100 μs) exposure times and high frame rates (1500 fps) using a CMOS camera. Images recorded by the camera are analyzed with a custom software package that performs automated particle tracking, intensity measurements, and generation of potential energy wells.

3.5.2 Number of Measurements per Particle

The intense scattering of particles in the waveguides evanescent field enables thousands of measurements to be performed on each trapped particle. Typical residence times of trapped dielectric particles are on the order of 3-10 seconds, depending on the laser power and the particles size and refractive index, which determine particle velocity. The CMOS camera equipped on the NanoTweezer surface instrument has an upper frame rate limit of 1529 fps, which translates

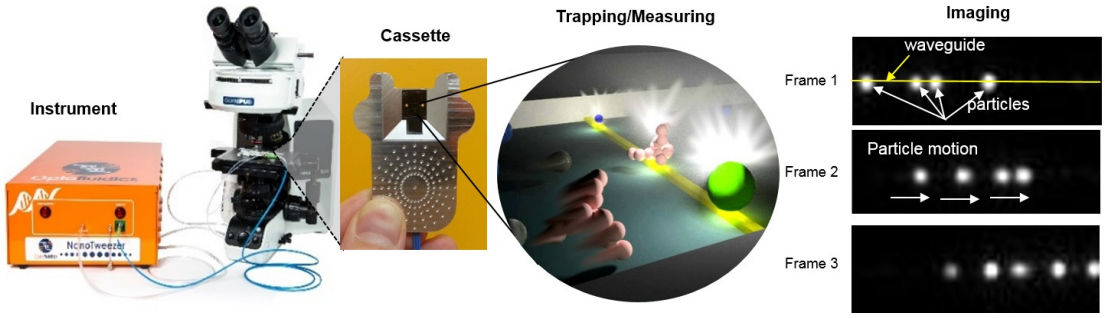

Figure 3.2: The NanoTweezer Surface system consists of an instrument and microfluidic cassettes. Particles in solution become trapped by an optical waveguide residing on the bottom of a microfluidic channel. Once trapped, particles scatter light and progress down the waveguide in the direction of light propagation.

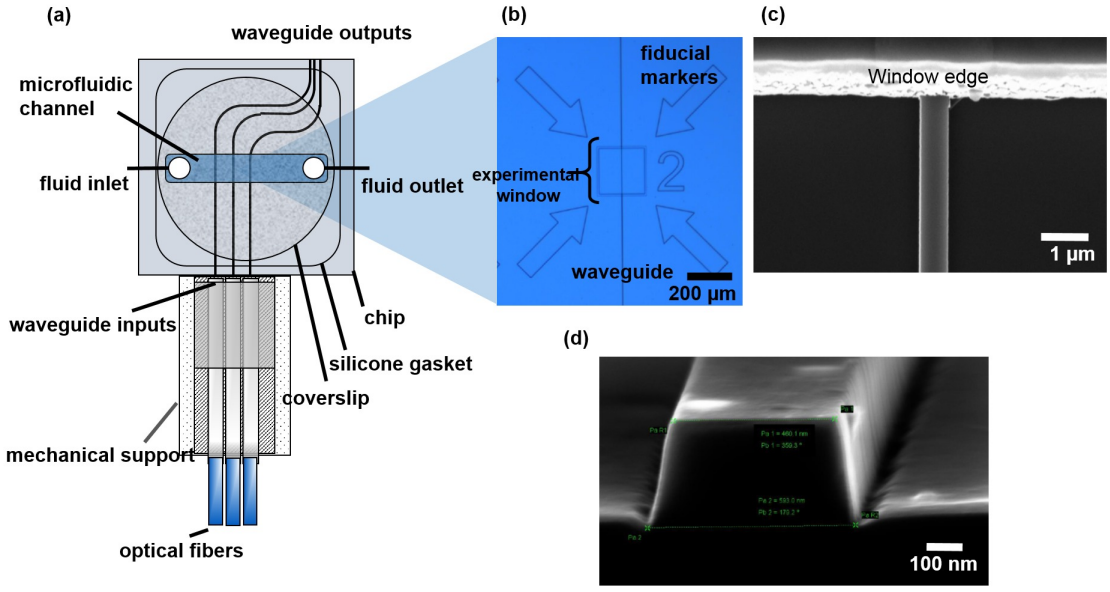

Figure 3.3: (a) Each chip consists of three waveguides, a microfluidic channel, and an optical fiber assembly for waveguide excitation. The waveguides are cladded by glass across the entire chip with the exception of the experimental window (b), in which a sample delivered to the microfluidic channel interacts with the waveguide. (c) SEM micrograph showing the edge of experimental window. (d) Cross-sectional view of waveguide structure.

to around 4,500-15,000 measurements per particle.

When too few measurements are made the high energy (low probability) portions of the curve are not sampled enough times for the histogram to accurately represent the probability distribution. As a result, the computed energies of these states fluctuate depending on how many data points are actually used in constructing the distribution. For example, if we only take 1000 measurements in the equilibrium state, the Boltzmann statistics predict that there is a 0.25% probability of observing a particle in a state 6 k_BT from equilibrium so the expected value of counts in the corresponding intensity bin is 2.5, but the actual number we observe must be an integer. If we actually sample this state 3 times, we will miscalculate its energy as 5.8 k_BT. To quantify this effect, subsets of increasing numbers of measurements were analyzed for 300 nm polystyrene nanoparticles. Fig. 3.4 shows potential wells constructed from randomly sampled subsets of increasing measurement number from a particle on which a total of 16,000 intensity measurements were collected. For clarity, only five potential wells are displayed in Fig. 3.4a. Each sub-sampled potential well was compared individually with the potential well constructed from 16,000 measurements by treating the subset potential well as an estimation model and computing the residual sum of squares between the two datasets in the range of $\pm$40 nm (Fig. 3.4b). An initial increase in the residual sum of squares is observed from 1000-2000 measurements. This is because very few observations are made in the lower probability states near the limits of the range, resulting in high sensitivity to measurement number. After this point, the effect of added measurement number is reduced, and the residual sum of squares decreases significantly for sample sizes above 3000 measurements. While some fluctuation is still observed due to the low probability (i.e. high potential energy) states, now enough ob-

servations are made in these states to mitigate these effects. In subsequent data analyses, a minimum measurement number of 3000 is applied to remove particles for which an insufficient number of intensity observations are collected. Raising the required measurement number would reduce uncertainty in potential energy and increase the range of observed displacement values. In practice, however, applying a minimum measurement number can remove a significant portion of the measured particles from the analysis, and a balance between individual particle data quality and inclusion of a sufficient number of particles should be sought.

3.6 Uncertainty Analysis

The measurements made using our technique consist of the integrated scattered light intensity from a particle in a frame captured by our camera. To characterize the uncertainty in these measurements, we measure the intensity of a particle stuck to the waveguide surface over time. As this particle is not actually moving in the z-direction, any observed intensity fluctuations will be due to the noise in the system and can be decoupled from the actual signal we are trying to measure, namely the intensity fluctuations due to particle motion. From this, we determine the uncertainty in I is 3-5% of the measured intensity value.

The next stage of the data processing consists of computing a histogram of the number of counts, N, of observations in a bin with a given intensity range. As each measurement has its own associated uncertainty, the value being placed in a bin is really $I \pm \sigma I$ where we assume that the errors in I follow the Gaussian distribution and therefore from our observations of the stuck particle we take

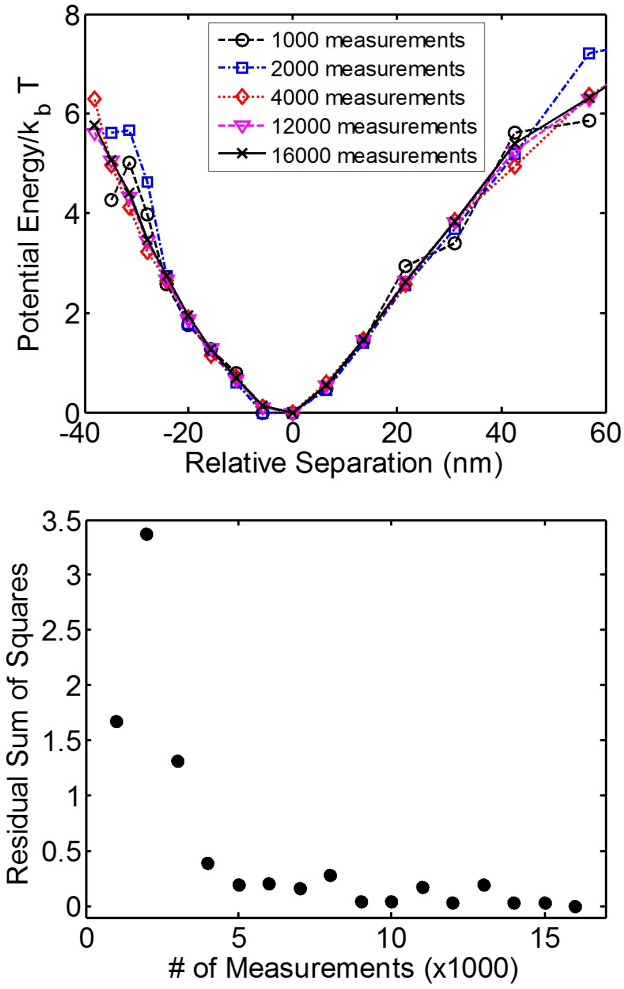

Figure 3.4: Effect of number of observations on potential well measurement accuracy. (a) Potential energy wells generated from randomly sampled subsets with varying sample size from a 16,000 measurement dataset. (b) Residual sum of squares plotted as a function of subset sample size. Residual sum of squares was computed by comparing the potential well generated from each individual subset to the potential energy well generated from all 16,000 measurements.

$\sigma I/I = 0.05$. Integrating the normal distribution between the bounds of each bin gives us the probability of a given value of the intensity falling into each of these bins. Summing these probabilities allows us to determine an expected value for N, and we can also compute the variance in N, $sigma_N^2$. As the measured potential energy is a function of N, I, N_{eq}, and I_{eq}, we can compute the uncertainty in U:

$$\frac{\sigma_U}{k_B T} = \sqrt{\left(\frac{\partial U}{\partial I}\sigma_I\right)^2 + \left(\frac{\partial U}{\partial I_{eq}}\sigma_{I_{eq}}\right)^2 + \left(\frac{\partial U}{\partial N}\sigma_N\right)^2 + \left(\frac{\partial U}{\partial N_{eq}}\sigma_{N_{eq}}\right)^2} \tag{3.10}$$

where U is the potential energy computed as in Eq. 3.6, N represents the number of intensity measurements in a bin and N_{eq} represents the number of measurements in the bin corresponding to equilibrium. These correspond to the probabilities discussed in Eq. 3.6. For typical experiments, this gives an uncertainty in the energy of each bin of around 0.07-0.08 $k_B T$. We show error bars computed using this procedure in Fig 3.5. Propagating this uncertainty to our computation of the force we see that

$$F = -\nabla U \approx -\frac{\Delta U}{\Delta z} \tag{3.11}$$

$$\frac{\delta_F}{F} = \sqrt{\left(\frac{\delta \Delta U}{\Delta U}\right)^2 + \left(\frac{\delta \Delta z}{\Delta z}\right)^2} \tag{3.12}$$

For typical forces on the order of 1 pN, this means that our uncertainties are on the order of 100 fN. In comparison, the TIRM literature reports force resolutions of about 10 fN and the AFM literature reports resolution of 10-50 pN [34, 120, 27].

The optical force confinement and enhanced signal give us the ability to measure much smaller particles than with conventional TIRM implementations. In general, metallic particles are easier to optically manipulate [40] and scatter far

more light than dielectrics of the same size, mainly owing to the fact that metals have much greater polarizability than dielectrics. Taking advantage of this, in Fig. 3.5a we demonstrate a direct measurement of the interaction of a 50 nm diameter gold nanoparticle (Sigma-Aldrich) with a waveguide. In the figure we show measurements on three independent particles on the same waveguide with the same optical power. As the figure shows, when the optical subtraction is performed the results are remarkably consistent for all three samples. There is sufficient light available for us to make these measurements with 9 μs exposure times. In Fig. 3.5b we show the surface force computed by taking the derivative of the surface energy for a representative sample, highlighting our ability to make pN scale force measurements. This represents a truly new regime, as these particles are half the size of the smallest gold nanoparticles measured by conventional TIRM implementations [36].

3.7 Conclusion

Using near-field light scattering techniques we have demonstrated the capability of making high throughput interaction measurements between nanoparticles and optical waveguide surfaces. The enhanced light confinement and optical gradient structure allow for measurements in the true nanoparticle regime. Here we have shown measurements on particles with diameters as small as 50 nm. However, there are no fundamental lower limits on the size of particles that can be measured as long as a large enough optical force can be applied to confine them in the evanescent field without damaging the particles and the scattered light signal is large enough to be observed. Furthermore, other than the well-known contribution from the optical gradient, no assumptions about the forces

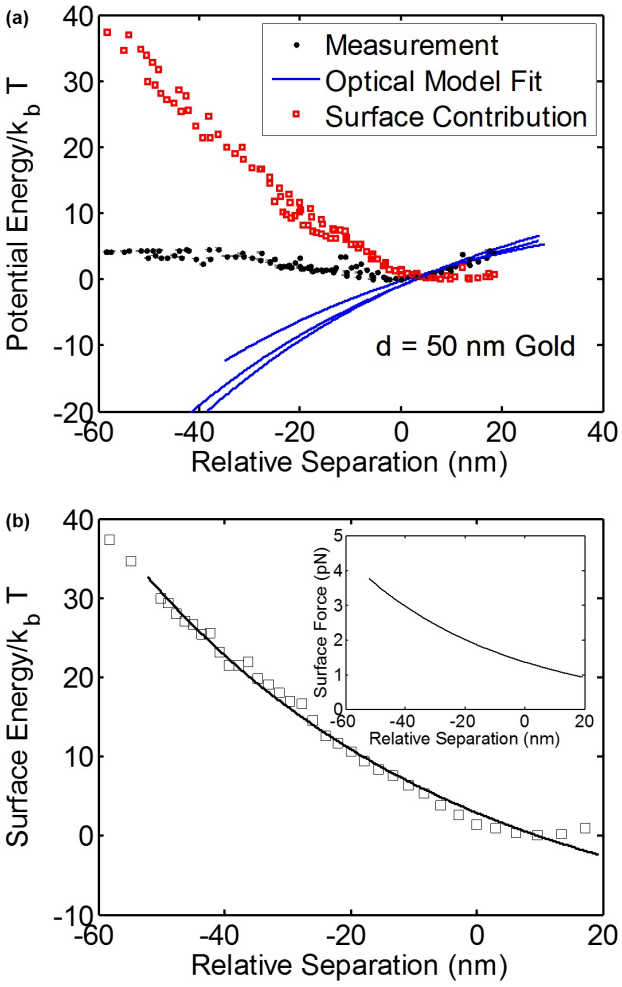

Figure 3.5: Experiments on 50 nm diameter gold particles in 0.01x PBS solution. (a) Data from 3 different particles are shown. The black points indicate the experimentally measured potential wells from three independent particles on the same waveguide with the same input optical power. Error bars are computed as described in the text. The blue curves indicate the optical model fits for each particle. The red points show the resulting surface interaction potential energy following optical subtraction. (b) Surface contribution to the energy landscape for a representative data set. Solid line represents fit to the data using Eq. 3.9. Inset shows the force profile computed from this using Eq. 3.11.

involved in the interaction need to be made. This is a key point because biomedically relevant nanoparticle suspensions can be incredibly complex. Going forward, this technique can be useful in characterizing nanoparticle coatings and determining the efficacy of nanoparticle surface modifications and other measures taken to enhance stability. Also, by measuring the same nanoparticles at different post production times in a given solution environment, this can be an important tool in assessing particle shelf-life and quality.

CHAPTER 4

ORTHOGONAL NANOPARTICLE SIZE, POLYDISPERSITY, AND STABILITY CHARACTERIZATION WITH NEAR-FIELD OPTICAL TRAPPING AND LIGHT SCATTERING

4.1 Abstract

Here we present and demonstrate a new technique for simultaneously characterizing the size, polydispersity, and colloidal stability of nanoparticle suspensions. This method relies on tracking each nanoparticles motion in three spatial dimensions as it interacts with the evanescent field of an optical waveguide. The motion along the optical propagation axis of the waveguide provides insight into the polydispersity of a nanoparticle suspension. Horizontal motion perpendicular to the propagation axis gives the diffusion coefficient and particle size. In the direction normal to the surface, statistical analysis of the scattered light intensity distribution gives a map of the interaction energy landscape and insight into the suspension stability. These three orthogonal measurements are made simultaneously on each particle, building up population level insights from a single-particle rather than ensemble averaged basis. We experimentally demonstrate the technique using polystyrene spheres obtaining results consistent with the manufacturers specifications for these suspensions.

For NIST-traceable polystyrene size standard spheres, we measure a variability in the hydrodynamic radius of $\pm$ 5 nm, compared with the manufacturers certified measurement of $\pm$ 9 nm in the geometric diameter made using transmission electron microscopy.

4.2 Introduction

As nanoparticles become increasingly important for applications including biosensing[121], drug delivery[6], catalysis[7], and enhanced oil recovery[8], quality control and verification of expected behavior remain important concerns[110]. Three key quantities for quality assurance are particle size,[122, 123, 124], polydispersity [125, 126], and interaction strength [127], because these metrics can give an estimate of the suspension's stability and performance.

Currently there are several existing techniques for characterizing subsets of these nanoparticle properties. Size and polydispersity characterization can be accomplished by making measurements of nanoparticle diffusion through methods like dynamic light scattering and nanoparticle tracking analysis which give a hydrodynamic size, by measuring size dependent optical or electrical properties, as in UV-Vis spectroscopy or with the Coulter principle, or by directly imaging the size using electron microscopy on a dried and prepared sample. Nanoparticle Tracking Analysis (NTA) [48] is one such sizing technique that can make single-particle size measurements in the native suspension environment. In NTA, particle suspensions in a channel pass through a light sheet, and scatter light. Particle trajectories are tracked by capturing video of the scattered light pattern and the mean-square displacement is computed. This is linked

to the diffusion coefficient and ultimately the particle size through the Stokes-Einstein relation [48, 128]. Other techniques such as those that use total internal reflection microscopy (TIRM) offer highly sensitive measurements of particle-surface interaction forces which are indicative of system stability, but do not provide size information [34]. Colloidal probe atomic force microscopy (AFM) also allows for measurements of surface-interaction forces [129, 79] but requires extensive sample preparation and suffers from very low throughput, making it largely impractical for large-scale quality control [130]. Because of these drawbacks, it is often necessary to perform multiple measurements on a given sample in order to gain a complete picture[130, 131, 132].

In this work we address this problem through an optical waveguide trapping technique that allows us to make orthogonal and simultaneous measurements of particle size, polydispersity, and colloidal stability. Using the optical forces to transport nanoparticles, we track the optically confined motion in three dimensions by imaging the light that each particle scatters as it interacts with the evanescent field. Particles are measured successively in a high-throughput, conveyer-belt like rapid interrogation, building population level metrics from single particle data. This extends our previous experimental and theoretical work with tracking the nanoparticle motion in the y- and z-directions and adds a new simultaneous characterization of the transport velocity in the x-direction to the picture (coordinate system shown in Figure 4.1), bringing in a new dimension where the physics are much more sensitive to the particle size. In addition to the analytic advances, we present demonstration experiments on real nanoparticle suspensions. We show how measuring these three axes yields insights into the suspension properties of polystyrene nanoparticles with radii of 260 nm and 400 nm that are missed using bulk techniques. While the initial

demonstrations presented here do not completely address all of the drawbacks of the existing techniques, we believe that making simultaneous measurements in three-dimensions is a promising approach for high-throughput nanoparticle analysis.

4.3 Results

4.3.1 Waveguide Based Optical Trapping

The primary element of our experimental system is a single-mode silicon nitride waveguide. Similar waveguides have been explored as tools for capturing and characterizing nanoparticles due to their optical confinement on the same length scale as the nanoparticles of interest [62, 63, 64, 65, 66, 67, 68]. In the present experiment fluid containing nanoparticles is delivered to the waveguide via a microfluidic channel (see our previous work in Chapter 3 and the Methods section herein for details). When a nanoparticle interacts with the evanescent field of the waveguide, it exerts a net force on the particle, which is commonly decomposed as an optical gradient force acting downward and inwards towards the center of the surface of the waveguide, and optical scattering and absorption forces which act along the direction of propagation. The forces that can be applied in these near-field optical traps cover the pico-Newton range and are tunable through the input optical power, allowing for force spectroscopy in a range of interest for many physical systems [133]. These forces are also strongly dependent on particle size [56], giving significant sensitivity in the transport behavior to variations in particle radius. In addition to the optical forces, the nanoparticle

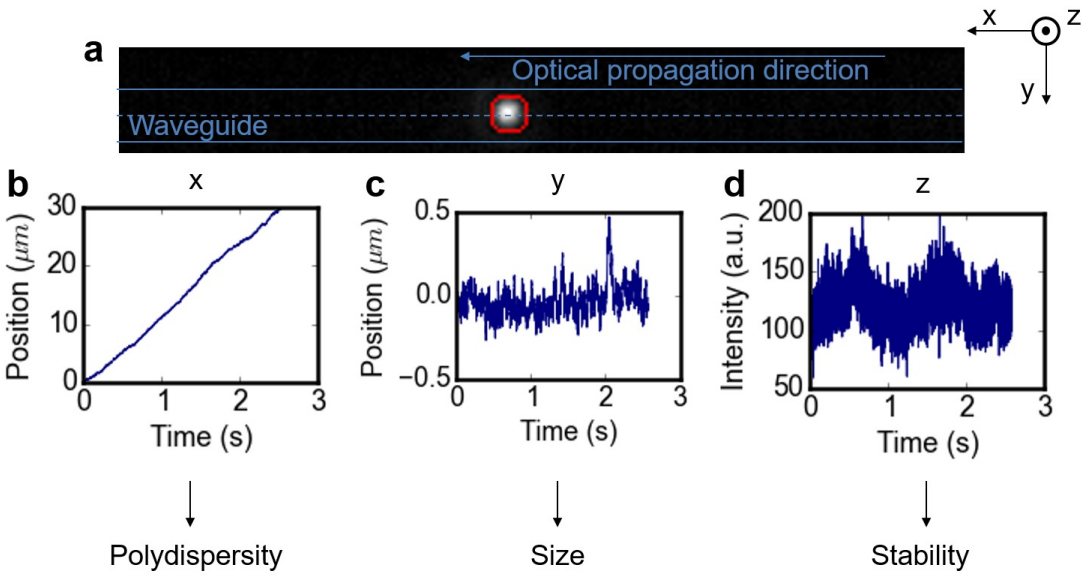

Figure 4.1: Orthogonal nanoparticle characterization scheme. (a) A particle is transported along an optical waveguide, scattering light as it interacts with the evanescent field. This scattered light is captured and recorded using a CMOS camera (example frame shown). The particle position is localized in each frame (red circle).The centroid position of the particle is tracked with sub-pixel resolution and the total intensity of light scattered by the particle is integrated in each frame. (b) In the x-direction (coordinate system shown in the upper-right corner of this figure) the particle translates at a terminal velocity, and the distribution in terminal velocities over the particle population gives a measurement of sample polydispersity. (c) In the y-direction, the particle undergoes confined and hindered diffusion in a harmonic potential well near the surface, which can ultimately be related to the particle size. (d) In the z-direction, the particle scatters more light when it is close to the waveguide and less when it is far away, so the scattered light intensity is used to track the z-position. Over many samples, the statistical distribution of scattered light intensity gives the probability distribution of finding the particle at a given energetic state, corresponding to a height in the potential energy well. Using the Boltzmann distribution, these probabilities give a map of the potential energy landscape, which is related to the energy barrier preventing the particle from sticking to the surface and therefore indicative of the suspension stability.

transport is influenced by hydrodynamic effects as well, which themselves are affected by the presence of the nearby surface [1, 134].

4.3.2 Three Dimensional Scattered Light Nanoparticle Tracking

An additional effect of the particles interaction with the evanescent field is that the particle scatters light. This scattering depends on the size and refractive index of the particle, but for a given particle the amount of light that it scatters is proportional to the local optical intensity in the evanescent field. Given that the evanescent wave decays exponentially, it is possible to use this intensity as a measure of the distance between the particle and the top of the waveguide. As we demonstrate herein, this fluctuation in intensity, coupled with the ability to track the centroid of the scattered light in the x-y plane allows for a particles motion to be tracked in all three spatial dimensions.

Figure 4.1 outlines the orthogonal characterization procedure. From a captured image of the scattered light as the nanoparticle interacts with the waveguide, the particle position is localized in each frame, as illustrated by the red circle in Figure 4.1(a). Based on 2D Gaussian fitting the x- and y-position of the particle centroid are localized with sub-pixel resolution as shown in Figure 4.1(b) and 4.1(c) respectively [135]. The intensity of the measured light signal is integrated around this centroid point, giving a value for the total intensity scattered by the particle as shown in Figure 4.1(d), corresponding to the position in the z-direction. These values are captured in every frame from a tracked particle, giving the particle's velocity, which is related to the polydispersity, the

y-direction diffusion coefficient, which is related to the particle size, and the z-direction interaction energy landscape, which indicates the relative strength of repulsive surface interactions. The details of how this information is extracted are provided in the following three sections.

4.3.3 Particle Size Information from the y-Direction Confined Brownian Motion

In the y-direction, the particle sees a potential energy well due to the optical intensity gradient of the mode profile of the waveguide. For single-mode operation, this will be strongest above the center of the waveguide and decreasing towards the edges. This results in an optical gradient force restoring the particle to the central intensity maxima. For small displacements from the center of the waveguide, these forces can be approximated as being linear in the y-displacement, and the particle experiences a harmonic potential well [61]. This is a useful approximation because a Brownian particle in a harmonic potential well is a canonical problem in the statistical mechanical literature and many developments have been made by previous researchers in measuring physical particle parameters from this motion[136]. We have previously developed a theoretical method for applying this harmonic model for particle sizing along the y-direction [137], of which we will give an abbreviated summary here.

For a particle confined within a harmonic potential, the time evolution of its position can be described by the Smoluchowski equation:

$$\frac{\partial}{\partial t}P\left(y,t|y_o,t_o\right)=D\left(\frac{\partial^2}{\partial y^2}+\frac{k_{trap}}{k_BT}\frac{\partial}{\partial y}y\right)P\left(y,t|y_o,t_o\right) \tag{4.1}$$

where $P(y, t|y_o, t_o)$ is the probability density function of finding a particle at position y at time t given initial position y_o at time t_o, D is the particle's diffusion coefficient and k_{trap} is the spring constant of the effective harmonic potential, k_B is Boltzmanns constant, and T is the absolute temperature. In the limit of very short time lags, Δt, between observations, the solution to this equation is a Gaussian function whose variance, σ, grows linearly with time:

$$\sigma^2(\Delta t) \approx 2D\Delta t. \tag{4.2}$$

By applying a linear fit to the variance over time in this regime, an effective diffusion coefficient can be extracted. Near the surface of the waveguide, however, this diffusion coefficient is not the same as its bulk value; rather, it is hydrodynamically hindered by a factor, here denoted as $\beta_{\parallel}(z, R)$ which depends in general on both the height above the surface as well as the particle size:

$$D_{\parallel}(z) = \beta_{\parallel}(z, R)D_{bulk} \tag{4.3}$$

where $D_{\parallel}$ is the hindered diffusion coefficient in the x-y plane, and D_{bulk} is the free-space diffusion coefficient. Detailed theoretical calculations of $\beta_{\parallel}(z, R)$ are well established in the literature [134]. In our previous work, we demonstrated that for very small heights above the surface, this converges to roughly $1/3$ the bulk diffusion for all values of R [137]. Refactoring this equation, we can then relate the measured diffusion coefficient directly to the hydrodynamic particle radius:

$$R \approx \frac{1}{3}\left(\frac{k_B T}{6\pi\eta D_{\parallel}(z=0)}\right) \tag{4.4}$$

where η is the fluid viscosity, and $D_{\parallel}(z = 0)$ is the experimentally measured diffusion coefficient assuming a negligible particle surface separation distance. To demonstrate the ability to distinguish differently sized nanoparticle populations using this analysis method, we performed two experiments: one using R

= 260 nm polystyrene beads and the other R = 400 nm polystyrene beads. The results of these experiments are shown in Figure 4.2. In Figure 4.2(a), the first three data points of the short time data are plotted for one particle of each size. We focus on the short time data because this is the regime where Eq. 4.2 is the most accurate. The data points here represent the variance in the displacement of a single particle in the y-direction. Each point computed by looking at how far the particle has displaced after a time of Δt from each frame in its trajectory and taking the variance of these displacements. As expected, the variance in the 260 nm particle motion increases more rapidly than the 400 nm one, consistent with a higher diffusion constant (and therefore a smaller particle). The slope of a linear fit to this short time data is taken, and it is used to compute the measured diffusion coefficient using Eq. 4.2. The non-zero intercept, not included in Eq. 4.2 is the result of Gaussian sources of noise in the experiments such as those due to localization errors in the particle tracking[3]. As long as these sources of noise are frequency independent, they will not alter the slope and the measured diffusion coefficient. Figure 4.2(b) shows a boxplot with aggregated effective diffusion coefficients from all particles measured. N = 8 particles are plotted for the 260 nm set, and N = 25 for the 400 nm set. This plot shows the distribution of the measured diffusion coefficient for the particles in the measured population.

If we compare the mean value of the diffusion coefficient for the two data sets, the 260 nm beads are indeed distinguishable from the 400 nm beads by their effective diffusion coefficient. If we take the approximation that

$$D \approx \frac{1}{3} D_{bulk}, \tag{4.5}$$

however, we find a measured radius of 149 nm and 238 nm, respectively 60% of the nominal radius for both particles. This overestimate of the diffusion coefficient might be attributable to the equilibrium height being above the surface.

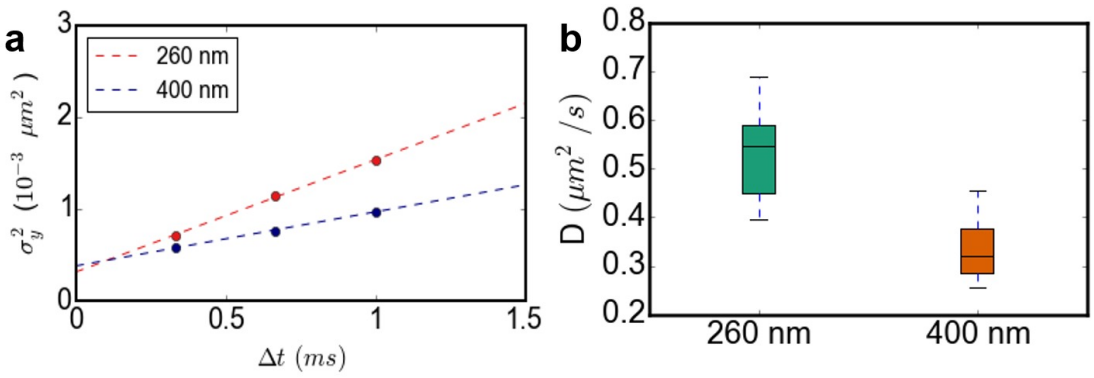

Figure 4.2: Analysis of y-direction motion. (a) Variance in y-position as a function of lag time for example R = 260 nm (red curve) and R = 400 nm (blue curve) nominal sized particles (only short lag times shown). In the limit of short lag times, the particle does not yet have time to respond to the restoring forces of the optical trap. In this diffusion-dominated regime, the variance in position is linear in lag time, and the particle undergoes normal diffusion. Linear fits are shown with dashed lines. The slope of these lines corresponds to the diffusion coefficient, as indicated in Eq. 4.2. (b) Population level measurements of diffusion coefficient. The smaller diameter particles diffuse faster, allowing for the two particle populations to be distinguished.

We hypothesize that this might be the case with these particles whose size is comparable to the width of the waveguide, as part of the particle may overhang the waveguide, experiencing hydrodynamic hindering from the substrate further below rather than the waveguide itself. This would lead to less hindering than predicted by the model, consistent with our experimental observation. This is not likely attributable to under-sampling the particle motion in the presence of the force-field, as this would result in an underestimate of the diffusion coefficient. Additional experiments must be conducted to determine the origin, but even with this bias, the populations of particles are still separable. Testing this hypothesis could be accomplished through experiments on smaller particles, which would require a higher sampling rate than is currently available in

our experiments. The primary limitation to the sampling rate is the data transfer rate over the USB 3.0 interface of full-waveguide images. As data transfer standards have greatly improved in recent years, we expect that these experiments will become possible with low cost CMOS cameras in the coming years, allowing for further validation and extension of these techniques to smaller size ranges.

4.3.4 Sample Polydispersity Information from x-Direction Transport Velocity

The y-direction analysis is valuable because it yields a hydrodynamic estimate of particle size, which is independent of the particle's optical properties or the optical power used. However, this is a stochastic estimator, and there is a lower bound on the variance in size estimate. As such, it can be useful for distinguishing e.g. 300 nm particles from 600 nm particles, but cannot resolve small deviations, e.g. 300 nm particles from 305 nm. These small differences in size can, however, be very significant for determining the reliability of the particles size dependent functionality. To determine this spread in the particle size distribution, we add an additional orthogonal measurement from the x-direction motion.

In the x-direction, the particle is propelled along the waveguide in the direction of optical propagation by its interaction with the evanescent field[62]. This motion arises from the optical scattering and absorption forces. These are balanced by the hydrodynamic drag on the particle. This results in transport at a terminal velocity with some fluctuations due to changes in the optical forces

resulting from the coupled motions in the other directions, as well as due to Brownian motion in the x-direction itself. For a particle in the Rayleigh regime (whose size is small compared to the optical wavelength), the optical scattering force, F_{scat} can be expressed as [64]:

$$F_{scat} = \frac{128\pi^5 I \epsilon_m}{3c\lambda^4} \left(\frac{\epsilon_p - \epsilon_p}{\epsilon_p + 2\epsilon_m} \right)^2 R^6 \tag{4.6}$$

where I is the locally available optical intensity in the evanescent field, ϵ_m is the relative permittivity of the medium, ϵ_p is the relative permittivity of the particle, c is the speed of light in vacuum, and λ is the optical wavelength. The accuracy of this approximation decreases for larger sized particles, please see the discussion below for more details regarding when use of this approximate model is justified. This optical propulsion is counterbalanced by the hydrodynamic drag force, F_{drag} which for these sub-micrometer particles can be modeled using Stokes' equation:

$$F_{drag} = 6\pi\eta R U_o \tag{4.7}$$

where η is the fluid viscosity, R is the particle radius, and U_o is the velocity in the x-direction. For a lossless dielectric particle, the optical absorption forces are negligible, and by equating F_{drag} from Equation 4.7 and F_{scat} from Equation 4.6, we derive an expression for this terminal velocity:

$$U_o = \frac{64\pi^4 I \epsilon_m}{9c\lambda^4 \eta} \left(\frac{\epsilon_p - \epsilon_p}{\epsilon_p + 2\epsilon_m} \right)^2 R^5 \tag{4.8}$$

This velocity is very strongly dependent (R^5) on the particle size, so small differences in the particle size can yield easily measurable differences in the measured velocity. The pre-factor in Equation 4.8 is in general unknown so the radius cannot be found directly from the velocity, and may be further complicated due to the increased hydrodynamic drag near a surface. If a solution of

multiple nanoparticles are measured under the same experimental conditions, e.g., on the same waveguide and at the same optical power, however, the velocity of two particles can be directly compared to find the difference in radius:

$$\Delta R = R\left[\left(\frac{U_{o,(R+\Delta R)}}{U_{o,mean}}\right)^{1/5} - 1\right]. \tag{4.9}$$

Here, $U_{o,mean}$ is the mean measured particle velocity, R refers to the nominal sample radius, and $U_{o,(R+\Delta R)}$ is the velocity of an individual measured particle. If a statistically significant number of particles are processed, this gives a highly sensitive measurement of the variance in the particle size within the sample. Combined with the mean radius determined from the y-direction motion, it is also possible to calculate the coefficient of variation of the nanoparticle distribution, a useful quality control metric to quantify polydispersity within the distribution.

In Figure 4.3 we plot the results of this experimentally for nominally monodisperse R = 260 nm and R = 400 nm nanoparticle suspensions (the same particles as shown in Figure 4.2). In 4.3(a) and 4.3(b) we show the nanoparticle displacement in the x-direction as a function of time for particles in each suspension. The linearity of the data indicate that each particle travels at a relatively constant velocity, subject only to very small fluctuations. These can be attributed to small variations in I due to input power fluctuations or the nanoparticle motion in the other spatial dimensions. From particle to particle, within each set there is some spread in the observed slope, corresponding to U_o. The velocity is steady over the length of the observation window, allowing for much less error in the measurement compared with the stochastic y-direction motion. By comparing the velocity of each trajectory to the average velocity for the full dataset, we can apply Equation 4.9 to find differences in the particle size

to single nanometer precision. We can use these variations to compute the standard deviation in particle radius, which when divided by the nominal sample radius supplied by the manufacturer gives us the coefficient of variation (CV). In Figure 4.3(c), we plot the spread in the radius for each particle using a box-and-whiskers plot (top and bottom bars indicate largest and smallest particles, box indicates 25th and 75th percentiles, line indicates median). The computed coefficient of variation is shown in the figure. For the nominal R = 400 nm particles, the spread in particle hydrodynamic radii is found to be $\pm$5 nm, yielding a coefficient of variation of 0.5%. This corresponds favorably to the CV of 0.6% and geometric diameter of $\pm$9 nm specified on the Certificate of Analysis from the manufacturer, as measured by Transmission Electron Microscopy (TEM).

4.3.5 Sample Stability Information from z-Direction Potential Energy Landscape

In addition to the motion in the x-y plane, the nanoparticles also experience forces and resulting motion normal to the surface in the z-direction. Unlike the x-y measurements that track the centroid position of the particle, the z-direction motion is tracked by spatially integrating the total intensity scattered by the particle at a given time when the particle is near the surface, the evanescent field intensity is stronger so the particle scatters more light and a brighter signal is observed. This approach is similar to the TIRM technique [34, 84, 80], and we have previously demonstrated its application to optically trapping structures (Chapter 2) and specifically to single-mode waveguides (Chapter 3). Concisely, this technique relies on mapping the statistical distribution of total scattered light

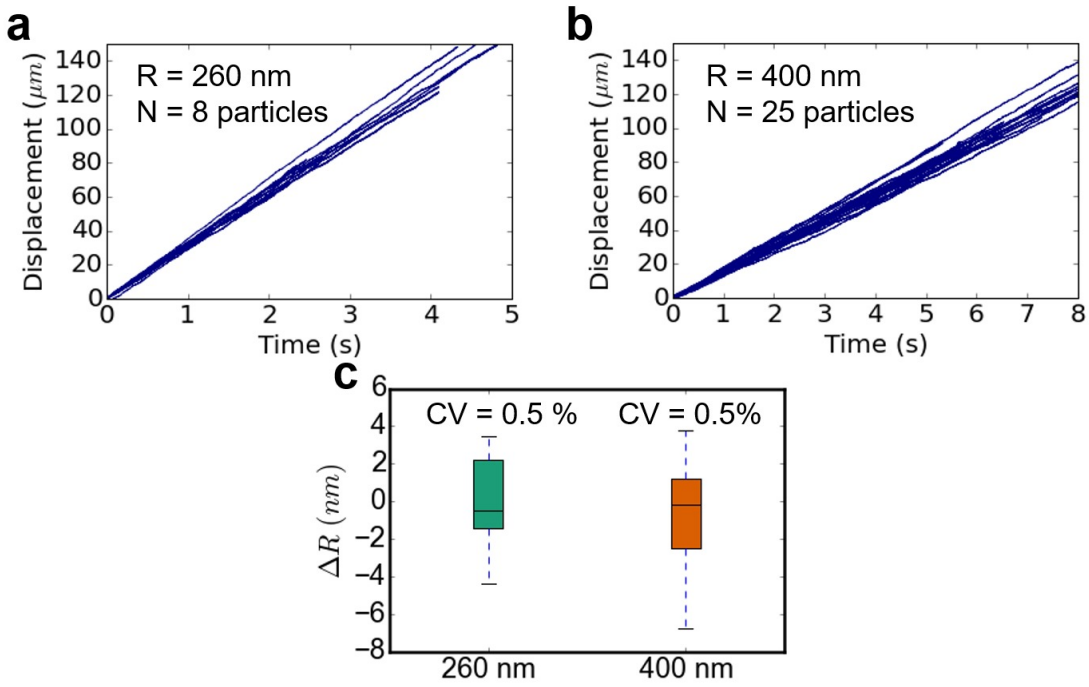

Figure 4.3: Analysis of x-direction motion. Top: x-position traces for (a) R = 260 nm and (b) R = 400 nm particles. The particles reach terminal velocity far faster than the timescale of these measurements. As the velocity depends on R^5, the spread in the terminal velocity (spread in the slopes) is related to the sample polydispersity. (c) Spread in particle radii (ΔR) for 260 nm and 400 nm samples. The coefficient of variation calculated with our methodology is consistent with the values certified by the manufacturer as determined through TEM.

by the particle onto the Boltzmann distribution, and using this to measure the potential energy difference as a function of particle-surface separation distance. This technique relies on the long-term probability distribution of the particle's position as it undergoes Brownian motion and samples different states in the z-direction potential energy well. While the dynamics of the particle's short timescale motion between these states will be influenced by the hydrodynamic presence of the wall, here we rely on the long timescale equilibrium statistical

mechanics.

Here, we focus on what this information adds to the characterization picture when combined with orthogonal measurements of the x-y nanoparticle motion. These measurements can show different physical mechanisms influencing particles of the same size, informing about the presence of contaminants or heterogeneous sub-populations that might be missed just by looking at the ensemble-averaged size.

We demonstrate this dimension by looking at the interaction potential energy landscapes between 260 nm and 400 nm radius nanoparticles with the silicon nitride waveguide surfaces. Here we look at the same particles depicted in Figures 4.2 and 4.3, but we now obtain information about the z-direction based on the scattered light intensity. The results of this analysis are shown in Figure 4.4.

As the Figure shows, the potential well (black curves in Fig. 4.4(a) and 4.4(b)) data are consistent for nominally monodisperse particles. An interesting aspect of the data is that the optical component of the potential well (blue curves) varies somewhat among these particle populations but the surface components retain similar shapes. This makes sense due to the strong (R^3) size dependence of the optical force. In this situation we expect the primary surface interaction force to be electrostatic in nature, and this is typically modelled as depending on R. The height of the repulsive energy barrier in both cases is indicative of the stability of these suspensions.

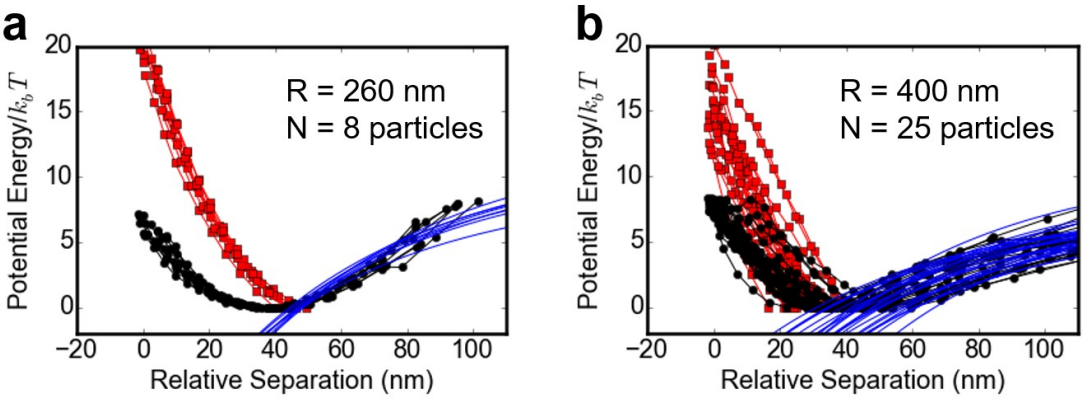

Figure 4.4: Analysis of z-direction motion. (a,b) Potential energy landscapes for (a) R = 260 nm and (b) R = 400 nm particles. The black curves with closed circles indicate the raw potential energy landscapes as computed from the Boltzmann distribution. The blue curves indicate the fits of the optical energy model to the optically dominated regime data. The red curves with closed squares are the surface interaction energy components that remain after the optical component is subtracted.

4.4 Discussion

Currently, our estimates of size from the y-direction diffusion suffer from relatively large uncertainties which make it difficult to discern small differences in the size. Because confined Brownian motion is a stochastic process, there will always be a degree of variance in the measured diffusion coefficient. The lower bound on this uncertainty will improve with more frames, however, as will any systematic biases in the measured size due to undersampling the diffusive motion. Other similar measurements of near-wall diffusion in the presence of force fields have reported similar measurement biases of diffusion in the direction of the force-field[138, 39]. As a result, the accuracy of this technique can be improved significantly by observing the motion with a faster camera. Given the rapid progress in camera quality and data transfer rates in recent years, we pre-

dict that it will soon be possible greatly improve the uncertainties of the sizing technique with low-cost equipment.

The x-direction analysis gives results that are physically sensible and consistent with the manufacturer's specification for these particles. However, the analysis technique is highly dependent on specific balance of forces in this physical system, and is therefore limited to only a narrow regime of particles. The upper bound on the size is determined by transitions to a regime of different optical physics, while the lower bound on size is determined by a transition to a regime where the particle motion is no longer defined by bulk transport at constant velocity.

The upper bound on the particle size for the x-direction measurements is determined by the optical physics of the Mie regime. In deriving Equation 4.6, the Rayleigh approximation was used. While the particles studied here are not strictly within the typically considered bounds of the Rayleigh regime ($2\pi R/\lambda \ll 1$), the simplified expressions derived using this approximation are still illustrative of their behavior as they are not large enough to experience morphology dependent resonances and other Mie regime complications [139, 140]. There is also recent experimental evidence[141] observing Rayleigh regime physics on polystyrene spheres with $2\pi R/\lambda \approx 1$, similar to the borderline cases discussed here. However, as we extend further into the Mie regime, the size dependences of the forces change, and in fact the horizontal optical forces are no longer even completely monotonic in size. As a result, we do not envision this technique being applicable to particles with diameters larger than about 1 μm. That being said, sub-1 μm particles are of interest in many application areas, and we envision the future use of this technique in characterizing

smaller particles than the ones studied here, where the inaccuracies caused by using the Rayleigh approximation will be smaller. There has also been some analytic progress in computing the full Mie solutions for the light scattered by particles under evanescent excitation[142, 143]. More detailed analysis based on this theory is a potential area for future investigation.

A key physical limitation on the x-direction mechanics is that it relies on the net transport of the nanoparticles. As this technique is applied to smaller particles, the diffusive motion in the x-direction can begin to become important. The analysis presented in Fig. 4.3 depends on the particle having a well-defined terminal velocity. This will happen when the particle's transport velocity is much greater than its diffusionin other words, when the particle's Péclet number is much greater than one. Where we have a large ($\gg$1) Péclet number, the motion is characterized by bulk transport at a terminal velocity, and the analysis presented here makes sense. For low Péclet numbers, the diffusion becomes significant and the particle's velocity will fluctuate. Near to the wall, however, the diffusion is hindered and the bulk expression for the Péclet number is also altered. If we consider the limiting case where D approaches 1/3 D_{bulk} (i.e. a particle very near the surface, see Equation 4.5), we can define a Péclet number for transport along the surface of the waveguide using the terminal velocity from Equation 4.8:

$$Pe_{\parallel,z=0} = \frac{RU_o}{D_\parallel} \approx 128\pi^5 \frac{I\epsilon_m}{\lambda^4 c}\left(\frac{\epsilon_p - \epsilon_m}{\epsilon_p + 2\epsilon_m}\right)^2 R^7 \tag{4.10}$$

The notation $Pe_{\parallel,z=0}$ indicates the Péclet number for diffusion parallel to the surface at a height of z = 0, i.e. right on the surface (note that this is for illustrative purposes only, this model is a limiting case of the optical and hydrodynamic effects that does not account for additional surface interactions). It is interesting to note that this expression is very strongly dependent on the particle radius

(R^7). As the particle size decreases, the relative effect of the diffusion on the x-direction transport will become much more significant, undergoing a rapid transition from the regime studied here to a regime where diffusion along the x-direction is prominent. This sets an effective lower bound on the size of particles that can be measured which will also be a function of particle material (ϵ_p) and applied power (I). In an intermediate Péclet number regime (Pe ≈ 1), it may be possible to determine an average transport velocity and use this for one analysis as well as looking at fluctuations from that average to perform a decoupled analysis of what should be the hydrodynamically hindered diffusion in the absence of a potential well (as there is no optical gradient in the x-direction). This measurement is potentially interesting as in this regime a much lower sampling frequency could yield accurate results. Measurements made in this way should in principle be similar to those made using NTA. However due to the very sharp transition in Péclet number with size the range of sizes this will work for is very narrow. For low Péclet number particles, the free-diffusion in the x-direction may yield more accurate sizing than the y-direction approach used in this paper; however the sensitive polydispersity information will be lost.

Effectively, based on this physics, we expect this technique to be useful for dielectric particles roughly in the size range from 250 nm to 1000 nm diameter. While there are many applications that rely on nanoparticles with smaller diameters, this measurement does fill an important niche. Specifically, this size range matches very well with the so-called sub-visible measurement gap noted by researchers investigating the sizes of aggregate particles in suspensions of protein therapeutics[144]. We therefore envision a possible application of this technique to simultaneously measuring the sizes, polydispersity, and surface interactions of these types of particles for quality assurance purposes.

In the z-direction, the data show relatively high potential energy barriers preventing surface sticking, and remarkably consistent surface interaction energy profiles among particles of the same population. This provides a key piece of insight missing from many particle size characterization techniques, as a very different interaction profile for a particle of the same size would indicate the presence of a secondary particle population, possibly an impurity or contaminant within the sample. As these measurements are brought up from an individual particle basis, the interaction energy curve of any single particle is available in addition to the diffusive and convective transport data for that same particle. This can help in figuring out what is happening with any possible outliers in a sample. We envision further implementations of this technique playing a role in quality assurance applications.

Here, we have demonstrated the principle of making orthogonal measurements to gain enhanced information about nanoparticle suspensions by tracking the motion of the nanoparticle in three spatial dimensions. We have performed proof of concept experiments on model nanoparticle suspensions and obtained results that are physically consistent and in line with expectations. Our measurements in the x-direction based on the variation in the optical transport velocity between different members of a population give results consist with the manufacturers specifications, though this technique is unfortunately limited to particles where the optical velocity dominates the Brownian motion in the x-direction. Measuring the y-direction hydrodynamically hindered diffusion shows that particles of different sizes can be distinguished, although absolute size determination remains inaccurate. Simultaneous to these measurements we have also mapped out the interaction energy landscapes for these particles. The pilot scale demonstrations reported here pave the way for future studies

to extend these techniques to a wider size range of particles, and further validate these techniques on larger sample sizes with polydisperse inputs. This technique can be used to gain both quantitative information about nanoparticle populations as well as identifying outlying particles in terms of size or chemical composition and identifying the role that these play in suspension stability.

4.5 Methods

4.5.1 Nanoparticle Suspensions

The particles used in the experiments were Fluoro-Max (Thermo Scientific R500, lot # 42116) with nominal diameter 520 nm, and NIST traceable certified mean diameter polystyrene spheres (Thermo Scientific 3800-05, lot # 44639) with diameter 799 $\pm$9 nm with coefficient of variation of 0.6% certified by transmission electron microscopy (TEM) measurement. Particle concentrations of 0.002% and 0.0015% solid fraction respectively were used. Particles were suspended in a solution of 0.237 mM KCl to create a Debye screening length, λ_D = 20 nm.

4.5.2 Optical and Fluidic Measurement System

These experiments used the NanoTweezer system and chips (Optofluidics Inc., Philadelphia PA USA). Light was coupled into the chips from the systems integrated 1064 nm laser. The devices used in these experiments are single-mode silicon nitride rectangular waveguides with cross-section of 250 nm x 600 nm. More details on the experimental system are provided in our previous work (see

Chapter 3). For these experiments the NanoTweezer pump was turned off and the nanoparticle suspensions were injected directly into the channel inlet tubing using a syringe. Separate waveguide chips were used for the 520 nm and 800 nm particles; however both chips had the same waveguide dimensions, and all data for each sized particle were obtained on the same waveguide with the same nominal input power. A nominal input power of 100 mW from the NanoTweezers laser source was used in these experiments. Scattered light is collected using a 20x microscopy objective and imaged at 3,000 frames per second using a CMOS camera with an exposure time of 24 μs.

4.5.3 3D Particle Tracking

Particle tracking was accomplished using the MOSAIC Particle Tracker plugin for ImageJ[135, 145]. The following parameters were used: radius = 1, cutoff = 0, per/abs = 1, link range = 1, displacement = 10, dynamics = constant velocity, object feature = 1, dynamics = 1, optimizer = Hungarian. Integration of videos to obtain the total intensity and therefore measure the z-direction motion was performed using MATLAB by reading in the centroid position from the MOSAIC track data and integrating a 12x12 pixel box around it by adding all of the pixel values in that box together.

CHAPTER 5

DYNAMICS OF AN OPTICALLY CONFINED NANOPARTICLE DIFFUSING NORMAL TO A SURFACE

Adapted with Permission from Perry Schein, Dakota O'Dell, and David Erickson, "Dynamics of an optically confined nanoparticle diffusing normal to a surface," Physical Review E, 93(6), 062139, 2016.

5.1 Abstract

Here we measure the hindered diffusion of an optically confined nanoparticle in the direction normal to a surface, and use this to determine the particle-surface interaction profile in terms of the absolute height. These studies are performed using the evanescent field of an optically excited single mode silicon nitride waveguide, where the particle is confined in a height-dependent potential energy well generated from the balance of optical gradient and surface forces. Using a high-speed CMOS camera, we demonstrate the ability to capture the short time-scale diffusion dominated motion for 800 nm diameter polystyrene particles, with measurement times of only a few seconds per particle. Using established theory, we show how this information can be used to estimate the equilibrium separation of the particle from the surface. As this measurement can be made simultaneously with equilibrium statistical mechanical measurements of the particle-surface interaction energy landscape, we demonstrate the ability to determine these in terms of the absolute rather than relative separation height. This enables the comparison of potential energy landscapes of particle-surface

interactions measured under different experimental conditions, enhancing the utility of this technique.

5.2 Introduction

Nanoparticles with diameters smaller than 1 μm are being increasingly used for numerous commercial and industrial applications including drug delivery [98], enhanced oil and gas recovery [9] and cosmetics [10]. Many of these applications require nanoparticles to operate in environments where they are tightly confined in regions with characteristic particle-wall separation distances on the scale of the particle diameter, such as geological pores and *in vivo* capillaries. In these regions, the hydrodynamic effects of the wall play an important role in dictating the transport properties of the nanoparticles.

Theoretical studies of the motion of small particles near fluid-solid interfaces were carried out by Brenner and coworkers in the 1960s [1, 146, 147, 2], who derived an exact expression for the dependence of the diffusion coefficient in the direction perpendicular to the surface as a function of particle size and separation distance. For regions near the interface (small h/R), Brenner's exact solution can be approximated [2, 148] and the scaling factor is given as:

$$\frac{D_\perp}{D_{bulk}} = f_\perp^{-1}$$
$$f_\perp \approx \frac{R}{h} + 0.2ln(\frac{R}{h}) + 0.9712 \tag{5.1}$$

where $D_\perp$ is the local diffusion coefficient in the perpendicular direction, D_{bulk} is the bulk diffusion coefficient far from the wall, $f_\perp$ is the scaling factor, R is the particle radius, and h is the distance from the bottom of the particle to the

interface. The full solution, along with this approximation are plotted in Figure 5.1(a).

Over the decades since Brenner's theory was published, there have been numerous experimental studies of the motion of particles near a wall providing evidence in support of the theory, initially on millimeter [149] scale particles before moving to the micrometer scale [150, 151, 152]. Many of these studies have used the Total Internal Reflection Microscopy (TIRM) to measure the hydrodynamically hindered particle motion under various conditions [153, 31, 154, 155]. A noteworthy example of this is the study performed by Oetama and Walz [3] who directly measured the motion of 15 μm diameter particles about 50-100 nm from a surface. This was achieved by looking at many trajectories of a single particle from each height and computing the variance in particle displacement following short time lags, and relating this to the local diffusion coefficient. Once this was done for several particle heights, the $D_\perp$ curve was fit to a linear approximation of Brenner's series (see the black curve in Figure 5.1(a)) allowing the absolute particle separation distance to be determined.

However, there are challenges involved in scaling this method to the nanoparticle regime. This is illustrated in Figure 5.1(b). For 15 μm diameter particles, the linear approximation is reasonable. However, for nanoparticles at similar separation heights this approximation breaks down and more accurate approximations are needed, as illustrated by the divergence of the black curve from the red and blue curves for the $R = 400$ nm case in Figure 5.1(b). Indeed, most of the experimental studies on hindered diffusion are performed for very small h/R ratios. Another challenge in directly measuring the diffusive motion of smaller particles is that the bulk diffusion coefficient is inversely proportional

to particle size. As a result, most of the previous work in this field has been limited to micrometer scale particles. A recent study by Liu et. al [35] looked at the diffusion of 3 μm diameter particles near an evanescently illuminated surface by holding them in place vertically using optical tweezers combined with a TIRM setup. Their experimentally measured diffusion coefficients match the predictions of Brenner's theory over a wide separation range from contact with the surface to about $h/R = 1$. While this measurement is useful as a system calibration allowing for the calculation of absolute separation distances without knowledge of system parameters like the evanescent penetration depth, the total measurement time needed to generate the $D_\perp$ curve for one particle was 20 minutes, making this technique poorly suited for high-throughput particle characterization.

Here we study the motion of sub-micrometer diameter particles as they undergo hindered diffusion near a liquid-solid interface. We demonstrate the capability of measuring the diffusion coefficient normal to the surface and determining the absolute particle-surface separation heights. This allows for population level particle-surface interaction measurements from a single-particle basis, enabling the identification of sub-populations in a heterogeneous suspension and the direct comparison of Nanophotonic Force Microscopy (NFM) [156] measurements under different experimental conditions with different equilibrium positions. Using a waveguide architecture, we measure particles sequentially with high-throughput with measurement times as short as 5 seconds per particle. The optical gradient force generated by the waveguide pulls the nanoparticles close enough to the surface to measure, while the high-speed CMOS camera enables measurement of the local diffusion coefficient at short enough time scales to neglect the drift effects.

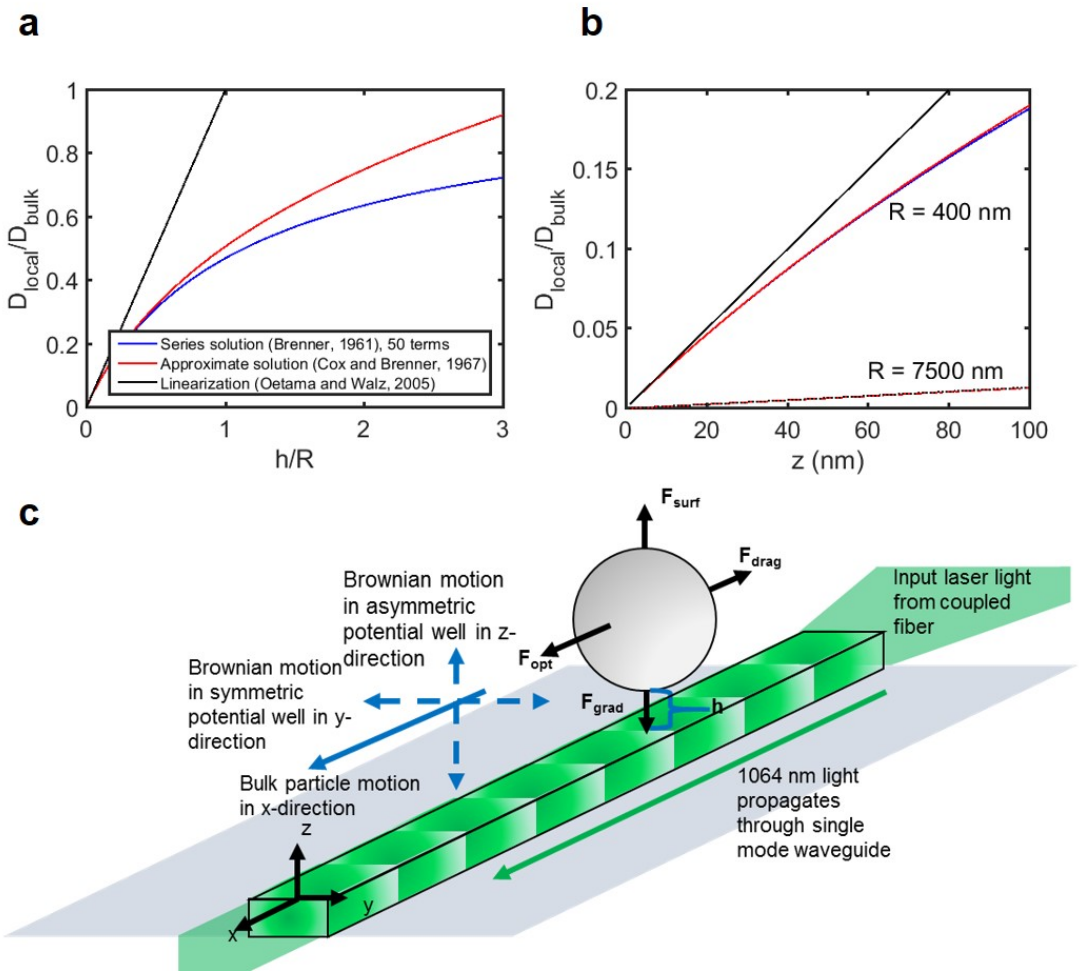

Figure 5.1: a) Non-dimensionalized plot illustrating Brenner's series solution (blue line, see also [1]) as well as some simplified approximations (red [2] and black lines [3], see refs.) for the fraction of bulk diffusion coefficient in the direction normal to a surface as a function of separation height (normalized by particle radius). b) Fraction of bulk diffusion coefficient plotted as a function of height for separation distances within 100 nm of a wall. Colors same as in the legend, solid lines correspond to a particle with $R = 400$ nm studied here, while dashed lines correspond to a particle with $R = 7500$ nm. c) Schematic of the experimental force picture and resulting 3-dimensional motion.

5.3 Analysis Procedure

The experimental system used in this study consists of a single mode silicon nitride rectangular waveguide. Suspensions containing nanoparticles flow over this waveguide in a microfluidic channel. For details of the experimental apparatus please see the Methods section below. As particles in the suspension interact with the waveguide, they experience forces and resulting drift motion in three dimensions, in addition to Brownian motion, as illustrated schematically in Figure 5.1(c). In the x-direction, along the optical axis of the waveguide, the particle experiences a propulsion force given by the sum of optical absorption and scattering balanced by the hydrodynamic drag force [62]. In the y-direction the particle experiences a symmetric potential which can be modeled as harmonic due to the restoring force provided by the optical gradient along the cross-sectional mode profile. In the z-direction, normal to the surface, the particle experiences an optical gradient force in the direction towards the waveguide due to the exponential gradient in the evanescent field. This is balanced by the net particle-surface interaction forces (e.g. electrostatic repulsion in a screened electrical double layer). The optical gradient force, F_{grad} is computed as [56]:

$$F_{grad} = \frac{2\pi\alpha_p}{c}\nabla I \tag{5.2}$$

where α_p is the polarizability of the particle, c is the speed of light, and ∇I is the intensity gradient. Unlike the TIRM scenario described previously, the fiber-coupling scheme provides a fixed angle of incidence, and the evanescent penetration depth is a known system parameter. As the particle moves along the waveguide and interacts with the evanescent field, it scatters light. The amount of light scattered depends exponentially on its height:

$$I_{scat} = I_o exp(-z/d_p) \tag{5.3}$$

where I_{scat} is the light scattered by the particle measured by the camera, I_o is the light that a particle at $z = 0$ would scatter, and d_p is the evanescent penetration depth. In practice I_o is not known, and will be different for every particle in a polydisperse sample, as it is a strong function of particle size. This is especially true for particles in the Mie regime, where the particle size is comparable to or larger than the optical wavelength, and morphology dependent resonances can occur [140]. However, without knowing I_o, the change in height of a single particle between two different observations can be determined by taking the ratio of I_{scat}. When many observations of a particle are taken, as in our experiments, it becomes convenient to compute the position of the particle in each frame relative to some reference height. In our previous work we used the equilibrium position as this reference [156]. Here, with the eventual goal of determining these separation heights absolutely we take a different approach, based on one developed previously in the literature [3]. Briefly, we select an arbitrary value of I_o, $I_{o,guess}$, define the particle position in all frames based on this guess, and compute the trajectory $z(t)$. It follows from equation 5.3 that

$$\begin{aligned} I_{scat}(t) &= I_{o,guess} exp(-z_{relative}(t)/d_p) \\ z_{absolute}(t) &= z_{relative}(t) + z_{offset} \end{aligned} \tag{5.4}$$

where $z_{absolute}$ is the actual distance from the bottom of the particle to the waveguide, $z_{relative}$ is height relative to where $I_{scat} = I_{o,guess}$, and z_{offset} is an unknown constant for each particle that will be determined through fitting the experimental data to hydrodynamic models.

To analyze the dynamics of our system we begin with writing the stochastic equation of motion for a particle moving near the waveguide. While the particle motion along the waveguide is a three-dimensional process (see Figure 5.1(c)),

here we will decouple the motion in the z-direction. Unlike previous works, the particles that we are studying are subjected to drift due to near-field optical gradient forces in the evanescent fields; at short time scales these become unimportant, and an approach resembling that developed in the prior literature can be used [3]. Using this Langevin-equation [148] approach, the one-dimensional equation of motion in the z-direction for our system can be written as:

$$\Delta z = \frac{D_\perp(z)}{k_B T}(F_{grad} + F_{surf})\Delta t + \frac{dD_\perp(z)}{dz}\Delta t + W(t)\sqrt{2D_\perp(z)\Delta t} \tag{5.5}$$

where Δz is the vertical displacement, F_{surf} is the net particle-surface interaction force, and $W(t)$ is a random variable chosen from the normal distribution with a mean of zero and a variance of 1. If the displacement is small, we can simplify this expression by taking $D_\perp(z) = D_{app}$, the apparent diffusion coefficient observed for motion near position z which is valid if the particle moves a small enough distance that the change in the diffusion coefficient is negligible. This can be ensured by taking a small enough Δt that the particle does not have time to displace very far. In the limit of small Δt further simplifications can also be made because the drift term due to external forces and the diffusivity gradient term both scale with Δt while the fluctuation term scales with $\sqrt{\Delta t}$ and so decays less rapidly as the lag time is decreased. In this diffusion-dominated regime, the displacement depends only on the fluctuation term:

$$\Delta z \approx W(t)\sqrt{2D_{app}\Delta t}. \tag{5.6}$$

By the definition of $W(t)$, the variance of the distribution of observed Δz is

$$\sigma_z^2 = 2D_{app}\Delta t \tag{5.7}$$

so D_{app} at a given height can be determined by plotting the variance in the dis-

placement over many vertical displacement "jumps" from that height as a function of the jump time lag, Δt and taking the slope.

To estimate z_{offset} and therefore calculate $z_{absolute}$ we seek to determine the apparent diffusion coefficient at several heights and fit it to the approximation of Brenner's series. Since the diffusion coefficient is spatially dependent and will change over the course of each particle's trajectory, and this process is influenced over long times by drift forces which are spatially dependent as well, we look at what happens over short vertical jumps from when a given height is sampled. Due to the stochastic nature of the process, we need to make a statistical measurement incorporating many jump trials from an initial height. To increase the number of jumps used in the statistics, we incorporate an approach which trades off some of the position resolution in order to obtain large statistical sampling while maintaining throughput. This is accomplished by discretizing the data to reduce the number of initial heights used and increase the number of trajectories from each height (see Methods for details).

5.4 Results

5.4.1 Variance in separation height

Figure 5.2 shows the results of a typical experiment. In Figure 5.2(a), for trajectories from one height that the system stochastically samples, we compute the variance in the displacement after a given lag time. The lag times used are integer multiples of the period between camera acquisitions, in this case (1/3,000) s. The black curve and symbols represent the experimental data, while the red

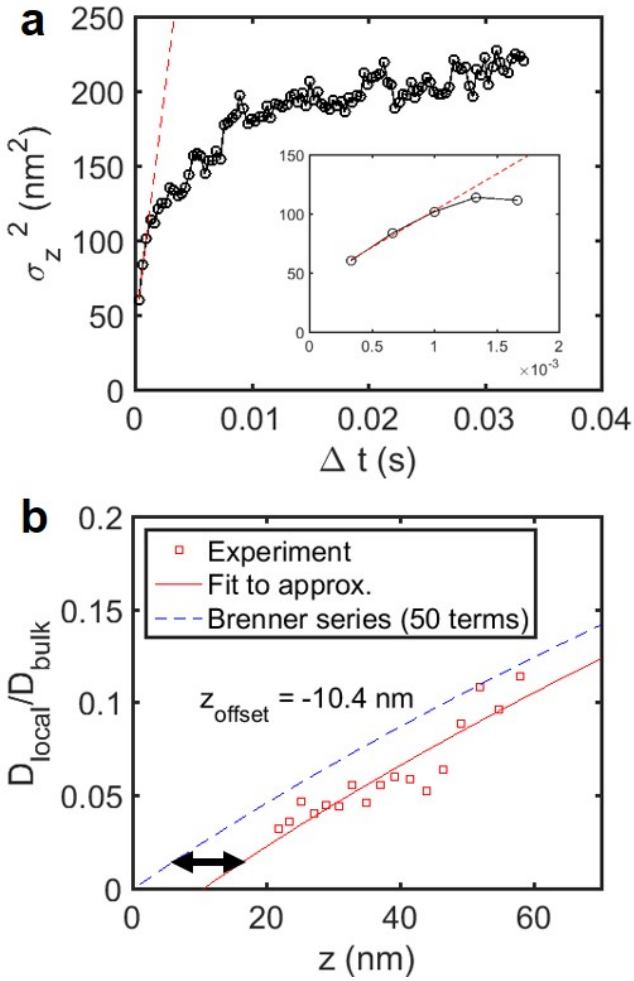

Figure 5.2: a) Variance in vertical displacement vs. lag time, computed for at least 500 trajectories from a single initial condition. At short time scales, drift is negligible and the particle undergoes normal diffusion. The diffusion coefficient is computed by taking the slope of the linear fit to the first 3 data points (red curve). Inset: close-up of the first 5 data points illustrating linear fitting in the diffusion dominated regime. b) After effective diffusion coefficients are determined for all initial conditions with sufficient trajectories, the data is fit, and the vertical offset is computed. The red squares are the experimental data. The red curve is the fit to the data using equation 5.8. For reference, the bulk diffusion coefficient for this particle is $D_{bulk} = 6.14x10^{-13}m^2/s$.

dashed line is a linear fit of the first three data points. The slope of this red line corresponds to the apparent diffusion coefficient, as shown in equation 5.7. The short time scale motion is highlighted in the inset. The linear increase is indicative of a regime in which the particle drift is negligible and diffusion dominates. The first three points are used in the fitting because this is the regime where drift due to the force field is smallest and diffusive motion dominates, leading to the most accurate prediction possible with this sampling rate. As the inset shows, for short time lags the particle is in the diffusive regime and the variance in the displacement is linear as indicated by equation 5.7. The slope decreases as drift becomes more significant. At long time scales the particle experiences the whole potential energy well and the variance no longer changes monotonically with increasing lag time. When this procedure is repeated for different initial conditions that the particle stochastically samples, different values of D_{app} are computed, as expected from equation 5.1. These are plotted as the red open squares in Figure 5.2(b). Of course, our values for the initial conditions are calculated based on an arbitrary selection of $I_{o,guess}$. To find the actual height of the particle, the experimental data are fit to a curve based on the approximation in equation 5.1, as shown in the red line in Figure 5.2(b). To simplify computation, this is done using the non-dimensional form of the equation, modified from equation 5.1 to include a fitting parameter for the spatial offset:

$$\frac{D_{\perp}}{D_{bulk}} = \left[\frac{R}{h + z_{offset}} + 0.2ln\Big(\frac{R}{h + z_{offset}}\Big) + 0.9712\right]^{-1}. \tag{5.8}$$

The result is a shifting of the $D(z)$ curve, as shown in Figure 5.2(b), annotated by the double arrow.

5.4.2 Population level energy landscape mapping

A major advantage of the waveguide architecture is the ability to interrogate particles in rapid succession to achieve high throughput. This can be observed in the Supplemental Movie (see Supplemental Material and Appendix for a detailed description) which depicts a single data acquisition. While not all of these particles can be tracked for long enough to get sufficient statistical data, the throughput is sufficient to obtain population level data over the course of a single experimental session (4-6 hours, including setup time). The value of z_{offset} obtained from the fits to the $D(z)$ curve specify the absolute separation height between the bottom of the particle and the surface in each time step. This is useful, since the same data used in these experiments can also be used to map the potential energy landscape incorporating the interactions between the particle and the surface as well as between the particle and the evanescent field. From the distribution in intensity as the particle translates along the waveguide, the relative potential energy can be computed from the Boltzmann statistics (for details see [157]):

$$\frac{U(z_{rel}) - U(z_{eq})}{k_B T} = ln\left[\frac{P(I_{scat}(z_{eq}))I_{scat}(z_{eq})}{P(I_{scat}(z_{rel}))I_{scat}(z_{rel})}\right] \tag{5.9}$$

where $U(z)$ is the potential energy at position z, $I_{scat}(z)$ is the measured scattered light intensity, and $P(I(z))$ is the probability of scattering at a given intensity determined from the measured distribution. However, since z_{offset} is determined from the fit, an absolute height can now be associated to each state. This facilitates the comparison of energy landscapes measured under different experimental conditions with different equilibrium heights. This is shown in Figure 5.3, where we show corrected equilibrium positions under different experimental salt concentrations, in dilute KCl and Phosphate Buffer Saline (PBS) solu-

tions, as characterized by the Debye screening lengths (λ_D). Each plot shows all particles successfully tracked in the given experimental condition with data meeting the criteria previously discussed, particularly at least 15,000 frames of tracked data at 3,000 frames per second for each particle. The particles used in all cases were NIST-traceable size standard polystyrene spheres (see details in Methods below).

5.4.3 Direct comparisons of nanoparticle-surface interactions under different conditions

To illustrate the utility of this advance, in Figure 5.4 the potential energy wells for two particles measured in different salt concentrations are shown, in 0.01x PBS ($\lambda_D = 7.6$ nm, blue squares) and in 0.001x PBS ($\lambda_D = 24$ nm, black circles). The experiments were performed on the same waveguide at approximately the same coupled optical power. The measured equilibrium is closer to the surface for the high salt case, consistent with the expectation of increased screening of the electrostatic repulsive forces due to the thinner electrical double layer. Looking at the left side of the curves, the repulsive energy barrier for reaching $z_{absolute}$ is much higher for the lower salt case, stabilizing the suspension. At higher salt concentrations, there is enhanced screening of the electrostatic repulsion, and therefore the energy barrier to coming into contact with the surface is lower. Comparing the right hand side of both curves, the similar magnitude and shape of the curve in the optical gradient dominated regime is consistent with the similar polarizability of both particles and the same optical power being applied in both cases.

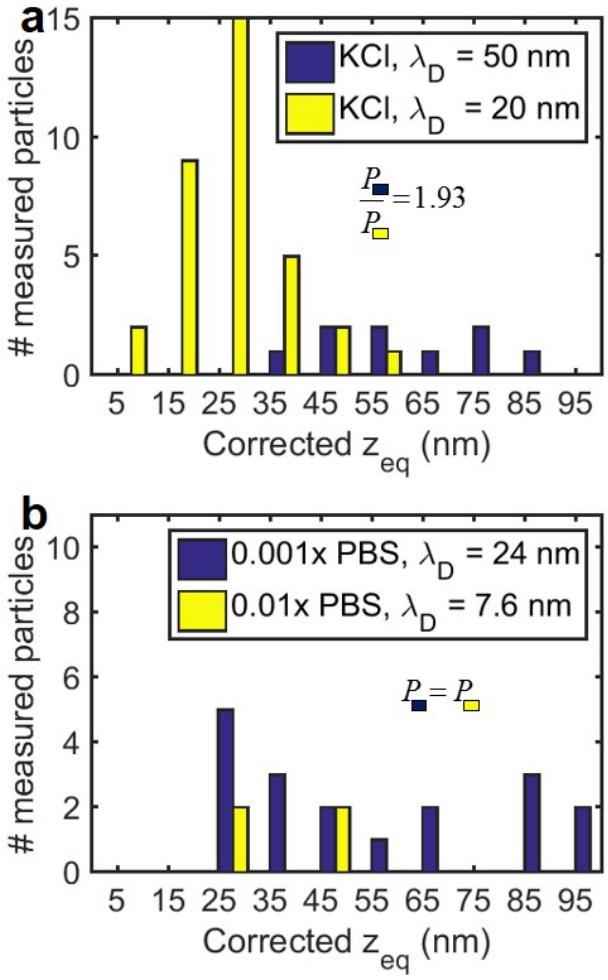

Figure 5.3: Histograms illustrating the number of experimentally measured particles at each calculated corrected equilibrium height, z_{eq} under various experimental conditions. a) 0.076 mM KCl in deionized water, $\lambda_D = 50$ nm (blue bars) and 0.237 mM KCl in deionized water, $\lambda_D = 20$ nm (yellow bars). Note that these experiments were performed at different optical powers, P, to ensure sufficient trapping, which also influences z_{eq}. b) PBS diluted to 0.001x in deionized water, $\lambda_D = 24$ nm (blue bars) and PBS diluted to 0.01x in deionized water, $\lambda_D = 7.6$ nm (yellow bars). These experiments were performed on the same waveguide with the same optical power.

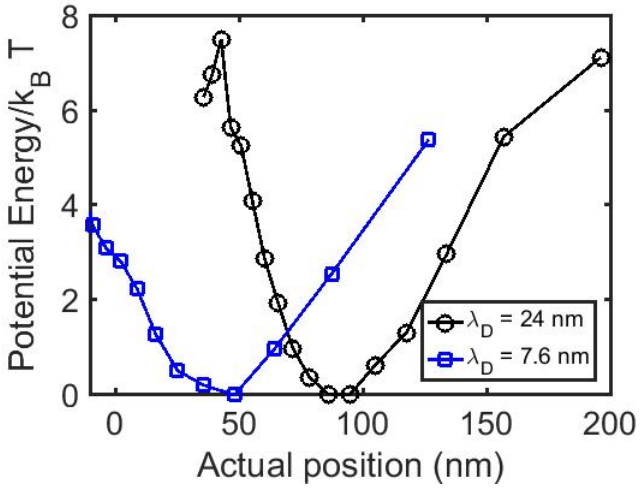

Figure 5.4: Potential energy wells calculated using the Boltzmann inversion for example particles in two different salt concentrations (0.001x PBS, $\lambda_D = 24$ nm, black curve and 0.01x PBS, $\lambda_D = 7.6$ nm, blue curve). The heights (horizontal axis) are absolute distances between the particle bottom and the waveguide. The potential energy, plotted as the energy difference relative to the equilibrium position for each particle is given in units of k_BT and includes contributions from the optical gradient and the particle-surface interaction.

5.5 Discussion

Significantly, Figure 5.2 indicates that with a reasonably fast camera we are able to obtain data in the diffusive regime where the variance in the vertical displacement is proportional to the lag time of the measurement, with the slope corresponding to the effective diffusivity of the particle. In this regime, the particle has not yet had time to respond to the external forcing of the optical and electrostatic fields, and instead its motion is determined purely by hydrodynamic effects. The use of a camera capturing the scattered light is important because we are able to record both the intensity and position of the scattered light pattern as the particle is propelled along the waveguide by the optical scattering

force. The optical confinement provided by the waveguide in two-dimensions allows us to probe particles with diameters smaller by a factor of 20 compared to similar analytical methods used without this confinement in the past [3], while relaxing the confinement in the x-direction allows for estimates of the absolute separation height with measurement times of about 5 seconds per particle as opposed to 20 minutes [35] or longer [158] with current state-of-the-art methods. The use of scattered light allows for shorter integration times, leading to measurements in the regime unbiased by drift effects, in contrast to recent studies with fluorescence techniques [39]. This is especially important when considering previous studies using near-field fluorescence techniques that report under-estimating the z-direction hindered diffusion of nanoparticles due to their inability to differentiate hydrodynamic effects from the electrostatic repulsion between the particle and the surface [159, 138]. In our experiments, Δt is sufficiently short (see equation 5.7) that we are able to measure the hydrodynamics of $R = 400$ nm particles, obtaining results consistent with the Brenner theory for normal diffusion in this regime.

As Figure 5.2(b) shows, the estimate of z_{offset} depends primarily on the accuracy of the fit curve to the measured local diffusion coefficients. As a result, the accuracy of this value depends on how accurately the slope of the variance in vertical position represents the diffusion coefficient in the diffusion dominated regime. This becomes more precise if more points are used in computing the variance and more accurate when the sampling rate is fast relative to the rate of diffusion. As D is smallest closest to the interface, for larger separations, this becomes less accurate because the time scale of diffusion is faster relative to the camera sampling rate. It is worth noting that as shown in equation 5.1, the diffusion coefficient is a function of both height and particle size. Therefore, in

principle it is possible to obtain an estimate of particle size as well as absolute height by using two free parameters in the fitting in equation 5.8. However, the accuracy of this remains poor with the present experiments. A route forward for future investigations may be to use the absolute height estimate obtained here in conjunction with a method based on the in-plane diffusion parallel to the surface, as we did in our previous work to obtain relative changes in particle size [60].

Since the primary limit to the sampling frequency available using CMOS cameras is the data transfer rate, we predict that improved technologies (for example the emerging USB 3.1 Generation 2 data transfer standard [160]) will enable higher frame rates, enabling measurements on smaller particles in the coming years. In addition, some progress has been made recently into extracting relevant physical parameters using data collected in the regime where both drift and diffusion effects are significant [158, 136]. Accounting for drift effects will allow for sampling rates that are slower relative to the diffusion time scales to still yield useful information.

Figure 5.3 displays histograms of the corrected equilibrium positions measured for populations of particles. This is accomplished in both 1:1 electrolyte (Figure 5.3(a)) and diluted buffered solutions (Figure 5.3(b)). The data are consistent with physical expectations as in the higher salt concentration experiments more particles have equilibrium positions closer to the surface, as expected from the increased screening of the electrostatic forces characterized by the shorter Debye length (λ_D). As the Figure shows, there is some variation in the equilibrium positions measured within each experimental condition. This is likely due to the fact that this position depends on the balance of optical gradient

and surface force effects, and the optical gradient force depends on the polarizability of the particle which is a function of particle radius to the third power, which explains these variations even with such nominally monodisperse samples. However, as shown most clearly with the blue bars on the right side of Figure 5.3(b), a small number of the particles behave much differently than the rest of the population. This illustrates how this technique can be used for the identification of impurities or other sub-populations in a heterogeneous suspension environment.

Unlike ensemble averaged measurement techniques like Dynamic Light Scattering, the presence of these different particles does not bias the results of the measurement on the primary constituents, as the individual data for each particle is measured independently. The estimation of absolute height requires no assumption about population monodispersity and is performed individually for each particle. This is accomplished without damage to or fouling of the waveguide or changing the experimental parameters, in contrast to the methods used in conventional TIRM experiments [34]. As the Supplemental Movie shows (see Supplemental Material and Appendix for a detailed description), the waveguide architecture allows for the interrogation of multiple particles in rapid succession. While not all particles can be tracked for long enough to acquire a sufficiently large statistical sample to perform the diffusion analysis procedure described here, the throughput is still sufficient to perform population level measurements. Each salt concentration in each panel of Figure 5.3 was obtained in a single experimental session.

In conclusion, we have demonstrated direct measurement of the diffusive motion of sub-micrometer scale spheres hindered hydrodynamically by the

presence of a wall. This can be performed simultaneously with interaction force or potential energy measurements, and gives an additional piece of information by defining an absolute separation height that is consistent with physical expectations. This is accomplished individually for each particle, making no assumptions regarding sample heterogeneity. The non-destructive nature of the absolute height estimate combined with the sequential measurements enabled by the waveguide optical scattering force and camera-based particle tracking make this technique well-suited for high-throughput population-level measurements. This can potentially be combined with other diffusion based measurements to eventually measure the size of individual nanoparticles simultaneous to the measurements of interaction energy and absolute height.

5.6 Methods

5.6.1 Experimental setup and materials

Experiments were performed using the NanoTweezer system and integrated waveguide and microchannel chips (Optofluidics Inc., Philadelphia, PA). Light from the system's 1064 nm diode laser was coupled into silicon nitride waveguides on-chip through optical fibers. The relative position of the fibers and the chip was adjusted to maximize measured output power. Typically, 10-25% of the input power was measured at the output photodiode. Input powers between 100-210 mW were used to maximize trapping without sticking beads to the waveguides, depending on the salt concentration, with higher input powers used for lower salt concentrations to compensate for the reduction in screening

of the electrostatic repulsive forces. The NanoTweezer pump was turned off during these experiments to reduce mechanical vibrations. Particles were injected into the inlet tubing directly using a syringe. No bulk fluid flow was imposed on the system during data acquisition. For these experiments, NIST traceable polystyrene spheres were used (Thermo Scientific, 3800-005). These particles were certified with a measured diameter of 799 ± 9 nm diameter as measured by Transmission Electron Microscopy (TEM). Experiments were performed in several aqueous suspensions. In all cases the beads were diluted to 0.0015% solid fraction. Experiments were performed in either KCl (Mallinckrodt Chemical, 6858-04) or Phosphate Buffered Saline (Sigma, P5493) diluted in filtered, deionized water at the concentrations stated previously.

5.6.2 Imaging, data acquisition, and processing

Images of the scattered light were recorded using a CMOS Camera (Basler, AC2000-165umNIR). The optical axis of the waveguide was aligned with the horizontal axis of the camera for maximum acquisition speed. Images were acquired over a region of interest spanning 16 pixels in the y-direction by 780 pixels in the x-direction (along the waveguide, see coordinate system in Figure 5.1(c)). Acquisition was performed over a USB 3.0 connection with a dedicated card (StarTech, PEXUSB3S25). This allowed for acquisition rates of 3,000 frames per second for 8-bit monochromatic images. To minimize motion blur, an exposure time of 24 μs was used, the shortest exposure possible with this camera. Gain levels were set to maximize the intensity signal without saturation, which was typically achieved at around 12 dB, roughly half the maximum possible with this camera, though this parameter varied under different experimental

conditions to ensure the use of as much of the pixel range as possible with no saturation. 80,000 frames were acquired in each acquisition set, (26.67 seconds per set). Between data sets there were typical delays of $\sim$3-5 minutes during image writing from the memory buffer to a solid state hard drive. Typically, 1-5 particles were observed during each acquisition. Particle trajectories were tracked from the raw images using the MOSAIC plugin [135, 145] for ImageJ. To account for artifacts in the tracking and imaging and to ensure a large statistical sample of data, only particle trajectories where the particle moved at least 5 pixels (corresponding to 1.375 μm) and containing at least 15,000 frames were used in the analysis. Using the centroid position from the track, the total intensity was integrated from a 12 x 12 pixel box around this position in each frame using MATLAB.

As the videos obtained have a pixel depth of 8 bits, and the integration is performed over a 12 x 12 pixel box, there are 36,864 possible values of scattered light intensity and therefore height that can be measured in each frame. This means that using the raw intensity data each height is sampled very few times in a typical particle trace of 15,000-30,000 frames. To get around this, each measured intensity value is divided by 100, rounded to the nearest integer, and multiplied by 100, reducing the number of possible height "bins." This can be thought of as a discretization of the data. Then, the dynamic analysis is performed for each height that is sampled 500 or more times, ensuring a reliable estimate of the variance in displacement.

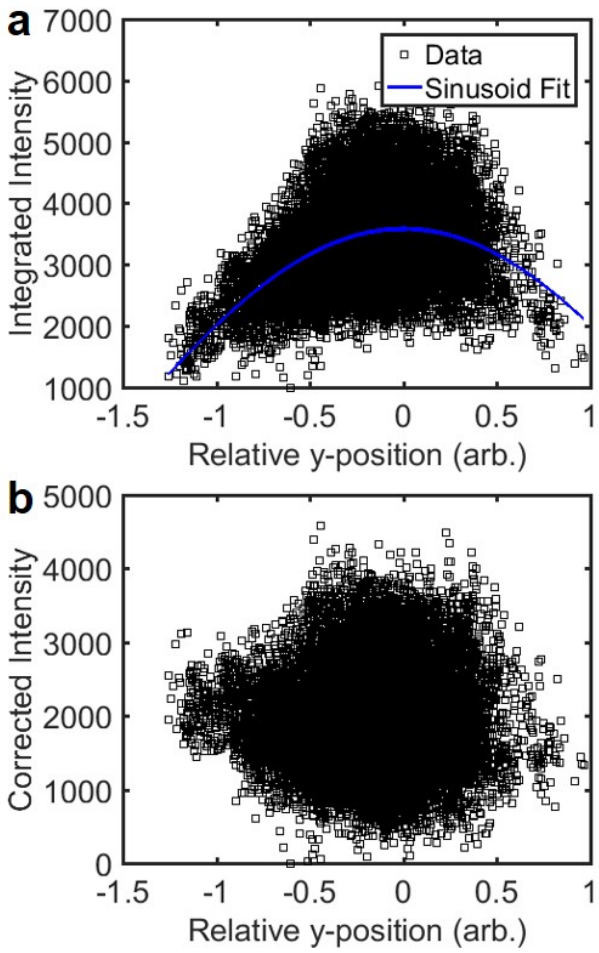

Figure 5.5: Mode profile intensity correction. a) Raw intensity data as a function of horizontal position in pixels. The blue curve is a sinusoidal fit to the data. b) Corrected intensity following subtraction of the sinusoid and renormalization. For reference, the total range of motion of this particle in the y-direction is 0.61 μm.

5.6.3 Correction for the lateral and longitudinal intensity variations

As the waveguide intensity profile is not completely uniform, in addition to the exponential changes in the scattered light intensity due to motion in the z-direction, a small portion of the intensity change will be due to the particle

motion in the y-direction. This is not a significant correction for small particles whose radius is much smaller than that of the waveguide and in scenarios where the confinement is tighter as in our previous work [156], but for the loosely confined 400 nm radius particles studied in this work, this could account for a substantial portion of the intensity change. To correct for this to a first approximation, we have developed an approach based on subtracting the underlying mode profile from the lateral distribution of the intensity. This approach works as follows. The intensity data are plotted as a function of y-position, as shown in Figure 5.5(a). As the figure shows, for positions near the center of the waveguide there is little correlation between the observed intensity and the lateral position in the region where the mode profile is relatively flat. Towards the edges, there is a stronger y-dependence, and the overall range of intensities sampled is lower because there is less light available for scattering in this region. To a first approximation, the mode profile can be modeled as a sinusoid. Fitting a sinusoid to the data as in the blue curve in Figure 5.5(a), note that the correlation is weak because the intensity depends much more strongly on the z-position than on the y-position. When this fitted curve is subtracted from the data, the result is an intensity distribution that is uncorrelated from y-position, as in Figure 5.5(b). This is the data used for further analysis.

In principle, variations in the evanescent field intensity along the direction of propagation (x-direction in Figure 5.1(c)) can also play a role in these measurements. However, for the single-mode silicon nitride structures used here, the material scattering and absorption losses in the experimental window are quite small ($<$0.1%, [161]) and the field can be considered uniform in this direction. While the presence of waveguide defects or stuck particles may locally cause the evanescent field to be non-uniform in the x-direction, in practice these regions

are excluded from the analysis as the tracking algorithm loses the particle as it interacts with these defects. With the waveguides used here, no significant defects with detectable scattering were observed prior to the start of experiments. Particle sticking occurred very infrequently with the relatively low powers and moderate salt concentrations used in these experiments, and the variation in intensity upstream and downstream of a stuck particle was not found to be a significant source of error.

CHAPTER 6

CONCLUSIONS AND OUTLOOK

6.1 Future Direction: Improvements to the NFM toolkit

For the dynamic studies described in Chapters 4 and 5, a key limitation on the size of the particles that can be measured is the ability to effectively measure particles on time-scales where the diffusive motion dominates the drift motion induced by the optical trap. As the optical confinement is significantly tighter in the z-direction as compared with the y-direction, the z-direction dynamic analysis requires even faster frame rates than the y-direction analysis. In both cases however, sampling at faster rates enables the ability to successfully capture this regime on smaller particles. In the experiments that we performed here with a low cost CMOS camera connected over a USB 3.0 connection, we were able to achieve frame rates of 3000 Hz. For the number of pixels imaged in our experiments, current state-of-the-art scientific CMOS cameras can achieve capture rates of up to 10,000 Hz. Going to higher frame rates with reasonably priced cameras and improved data transfer rates will allow for continued pushing of the boundaries of NFM. As the frame rates and exposure times become faster and the particles measured become smaller, signal detection limits become relevant again, and it may be necessary to increase the input power to the waveguides to ensure trapping and imaging.

Another engineering improvement to assist in the dynamic studies is the use of wider waveguides with larger surface area and less optical confinement. Although as shown in Chapter 5 we can account for the lateral intensity variations in the y-direction due to the mode shape of the waveguide that may alter the

NFM profile, there are other effects due to the finite waveguide width. Though this will limit the smallest size of particles that can be trapped, it can lead to improved results in the dynamic studies for several reasons. First, less confinement means weaker drift forces, extending the diffusion dominated regime to longer timescales. Also, a wider waveguide means less ambiguity about which surface the particle is hydrodynamically interacting with, especially for cases where with the current waveguide widths, the particle may overhang the waveguide, which could correct the inaccuracies in sizing using the surface hydrodynamic approximation introduced in Chapter 4.

Given the frequency with which particles interact with the waveguides, the interaction times, the camera frame rate, and the measurement time needed to ensure a sufficiently large number of frames to perform an accurate analysis, in principle the NFM method should achieve throughput of up to thousands of particles per hour. In practice however, a typical experimental session yields closer to 10 particles per hour. This is primarily limited by the time spent in transferring data from the camera to the RAM in the attached computer, and writing data from the RAM to a solid-state hard drive. Currently this takes 2-3 minutes for a 90,000-frame experimental acquisition, but improvements in computing technology will help to reduce this dead time in the future.

6.2 Future Direction: Emerging Application Areas

6.2.1 Benchmarking Reference Materials for use in Harsh Environments

As discussed in Chapter 1, one of the main challenges in understanding the behavior of nanoparticle suspensions in harsh environments, particularly at high salt concentrations, is the inability of the current theory to provide predictive capability. In terms of developing products, this means that it is difficult to know in advance whether a given stabilizing coating will work for a given particle, or what formulation conditions to use in order to ensure the stability of a new product. To address this, a future line of research can involve the use of NFM to develop a general look-up table for predicting nanoparticle interactions and suspension behaviors such as the propensity towards aggregation in a variety of realistic experimental conditions with a variety of reference nanoparticle types. This can provide a rapid screen to determine how a new nanoparticle product's behavior might change in response to, for example, a change in the environmental operating conditions (such as a change in pH or salt concentration) or the selection of a different nanoparticle coating. This table can be established by using the high-throughput waveguide NFM implementation to rapidly screen nanoparticles of different types and different surface coatings, obtaining a family of force-distance curves for each particle under a range of experimental conditions.

The hypothesis here is that because we are making a direct measurement of the stabilization force (rather than inferring it from an indirect method) we

should be able to interpolate within the table to determine the possible stabilizer, particle, and environmental condition combinations that will work for the desired application. Building one of these lookup tables for a given family of stabilized nanoparticles will help in determining how many data sets are required to interpolate a reasonable result, establishing a useful experimental protocol that can be used by formulation scientists to take advantage of NFM to make predictive measurements of particles relevant to their application space.

6.2.2 Experimental Validation of Molecular Dynamics Simulations for Nanoparticle Interactions

In Chapters 2-5, I have discussed making direct measurements of nanoparticle interactions as a means of overcoming the deficiencies of the DLVO theory in predicting the behavior of nanoparticle suspensions. An alternative approach explored in the literature has been to work from the bottom up, providing direct answers regarding nanoparticle interactions by simulating these systems using atomistic molecular dynamics methods [18]. These simulations calculate the potential of mean force (PMF) as a function of particle-particle or particle-surface distance directly by calculating all of the interatomic forces without the use of any smoothed models or superposition of assumed additive forces. The PMF curve is essentially equivalent to the potential energy landscape measured using NFM. Recent computational studies have demonstrated the ability to directly compute these interaction energy landscapes for particles with characteristic diameters on the order of 1 to 5 nm [162, 19, 163]. The results deviate substantially from DLVO theory [19].

As computational efficiency improves and computational resources become cheaper, the path towards atomistic simulations of larger nanoparticles becomes more feasible. Concurrently, as shown in Chapter 3, NFM can work on nanoparticles with diameters as small as 50 nm, and previous studies have demonstrated optical trapping (though not scattered light interaction measurements) on polymer nanoparticles down to diameters of 22 nm [59]. The gap between experimentally measurable interactions and direct atomistic simulations is narrowing. With a future generation of higher quality-factor photonic crystal devices capable of making scattered light interaction potential energy measurements on sub-20 nm particles combined with improving computational ability to predict interactions of 10-plus nm diameter particles, an available line of research in the near-future will be to bridge these approaches, and use the NFM measurements to validate the molecular dynamics results in this intermediate size regime, directly comparing the NFM measurement to a PMF curve achieved through atomistic computation.

6.2.3 Characterization of Protein Aggregate Particles

One key application area where characterizing the size and stability of nanoscale colloidal products is critical is in assessing the presence of protein aggregates in therapeutic products. While protein therapeutics offer many advantages over small molecule drugs, one major challenge is that they can sometimes trigger an immune response in patients, which causes the drug to cease functioning and can cause harmful side effects [164, 165, 166, 167]. It has been shown that the presence of aggregate particles in the drug formulation increases the risk of these effects, and so it is desirable to characterize protein aggregates,

especially those in the 100 nm to 5 μm size range [144, 168, 169, 170]. While this size range corresponds to a measurement gap where many commonly used biophysical characterization techniques break down, as I have shown in Chapters 2-5, this is precisely the size range where NFM is viable.

A possible way to optimize NFM for the measurement of protein aggregates is shown in Figure 6.1. In this implementation, a suspension containing protein aggregates flows down the waveguide in the same direction as the optical propagation axis. Here, a glass waveguide can be used to allow for easy functionalization with a variety of reference surfaces and coatings. Following the procedure demonstrated in Chapter 4, we can make simultaneous measurements of the diffusion coefficient and hydrodynamic size as well as the interaction force-distance curve. We hypothesize that differences in the surface interaction measurements will give insight into the physicochemical properties of different aggregate conformations, and when made orthogonal and simultaneous to measurements of the protein aggregate size, this line of research could provide a significant advancement towards the characterization of protein aggregates.

6.3 Conclusions

In Chapter 2, I introduced the concept of Nanophotonic Force Microscopy, and demonstrated the technique on dielectric nanoparticles using a photonic crystal resonator to generate the optical forces. This demonstrated the ability to make direct k_BT scale interaction energy measurements and sub-pN force measurements on nanoparticles suspended in buffer solutions. In Chapter 3, I showed that by relaxing the optical confinement in one dimension by using a single-

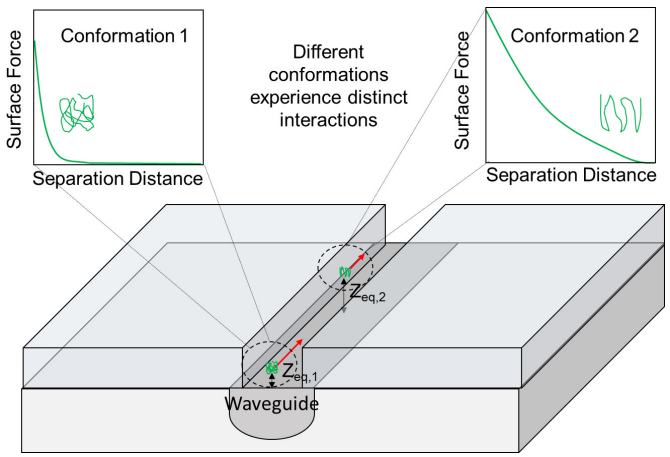

Figure 6.1: High-throughput in-line force measurement technique. Here, two protein aggregates of the same hydrodynamic size but different conformation experience different surface interactions, with conformation 1 being weakly repelled and reaching an equilibrium height, z_{eq} near the surface, and conformation 2 being more strongly repelled and reaching an equilibrium further away. Note that the channel is narrower than the waveguide, ensuring that all particles interact with the evanescent field.

mode waveguide to perform NFM measurements I could greatly improve the throughput and interrogate many nanoparticles in rapid succession. This was demonstrated through studies on 50 nm diameter gold nanoparticles. Relaxing this confinement opened up asymmetric nanoparticle motion in three dimensions. In Chapter 4, I took advantage of this motion in the plane parallel to the waveguide surface to make measurements of the sample polydispersity and the particle diffusion coefficient. In Chapter 5, I extended the study z-direction out-of-plane motion of the nanoparticle to look at the dynamics of how the particle transitioned between states in the potential energy well. Using this information in combination with established hydrodynamic theories of hindered diffusion near a wall, I was able to gain insight into the absolute particle-surface separation height.

Taken together, the results of this dissertation establish NFM as a viable technique for making direct measurements of the quality of nanoparticle products by providing information related to properties including stability, particle size, and heterogeneity. Compared to previously developed direct measurement techniques like TIRM and colloidal probe AFM, I have demonstrated the ability to make measurements on smaller particles than either technique, measure smaller forces than AFM and comparable forces to TIRM, and achieve much greater throughput than either technique, with far simpler sample preparation than with colloidal probe AFM. I have also demonstrated the ability to make orthogonal measurements simultaneously on the same particles, and the ability to work with different particle types and environmental conditions without making any assumptions about the underlying forces beyond the optical trap.

However, there exist some remaining challenges in translating these advances into an integrated sample-in answer-out implementation that provides useful information for nanoparticle quality control. First, the experiments require substantial preparation time by an expert user; a much higher degree of automation in terms of the optical coupling, imaging set-up, and triggering data collection to begin when the particles first become trapped would assist in translating the technique for more broad adoption. Additionally, at present the throughput and temporal resolution are largely limited by the data transfer rate from the camera and write-time to a solid-state disc. Improving this would allow for the use of a higher frame rate camera, enabling more accurate y-direction measurements, shorter measurement track times, and the ability to capture faster time-scale motion, improving the accuracy of the dynamic analysis and enabling measurements on smaller nanoparticles. Beyond these engineering improvements to the measurement system, another necessary step

to the widespread use of NFM is the ability to easily measure the interaction between the particle and application relevant reference surfaces, such as those representative of physiological or environmental surfaces that particles may encounter in real applications. The silicon nitride surfaces used here provide a well-established reference, but are not relevant to many applications. These improvements, along with detailed case studies to validate the use of NFM for critical applications and fundamental studies in physics and biology provide great opportunities for future work to extend this emerging field.

BIBLIOGRAPHY

[1] Howard Brenner. The slow motion of a sphere through a viscous fluid towards a plane surface. *Chemical Engineering Science*, 16(3):242–251, 1961.

[2] Raymond G. Cox and Howard Brenner. The slow motion of a sphere through a viscous fluid towards a plane surfaceii small gap widths, including inertial effects. *Chemical Engineering Science*, 22(12):1753–1777, 1967.

[3] Ratna J. Oetama and John Y. Walz. A new approach for analyzing particle motion near an interface using total internal reflection microscopy. *Journal of Colloid and Interface Science*, 284(1):323–331, 2005.

[4] Matthew Mancuso, Li Jiang, Ethel Cesarman, and David Erickson. Multiplexed colorimetric detection of kaposi's sarcoma associated herpesvirus and bartonella dna using gold and silver nanoparticles. *Nanoscale*, 5:1678–1686, 2013.

[5] Seoho Lee, Saurabh Mehta, and David Erickson. Two-color lateral flow assay for multiplex detection of causative agents behind acute febrile illnesses. *Analytical Chemistry*, 88(17):8359–8363, 2016.

[6] Partha Ghosh, Gang Han, Mrinmoy De, Chae Kyu Kim, and Vincent M. Rotello. Gold nanoparticles in delivery applications. *Advanced Drug Delivery Reviews*, 60(11):1307–1315, 2008.

[7] Wenbo Hou and Stephen B. Cronin. A review of surface plasmon resonance-enhanced photocatalysis. *Advanced Functional Materials*, 23(13):1612–1619, 2013.

[8] Hadi ShamsiJazeyi, Clarence A. Miller, Michael S. Wong, James M. Tour, and Rafael Verduzco. Polymer-coated nanoparticles for enhanced oil recovery. *Journal of Applied Polymer Science*, 131(15):n/a–n/a, 2014.

[9] Hua Zhang, Alex Nikolov, and Darsh Wasan. Enhanced oil recovery (eor) using nanoparticle dispersions: Underlying mechanism and imbibition experiments. *Energy & Fuels*, 28(5):3002–3009, 2014.

[10] Yang Deng, Asiri Ediriwickrema, Fan Yang, Julia Lewis, Michael Girardi, and W. Mark Saltzman. A sunblock based on bioadhesive nanoparticles. *Nat Mater*, 14(12):1278–1285, 2015.

[11] George A Truskey, Fan Yuan, and David F Katz. *Transport phenomena in biological systems*. Pearson/Prentice Hall Upper Saddle River NJ:, 2004.

[12] M. Boström, D. R. M. Williams, and B. W. Ninham. Specific ion effects: Why dlvo theory fails for biology and colloid systems. *Physical Review Letters*, 87(16):168103, 2001.

[13] Sheva Naahidi, Mousa Jafari, Faramarz Edalat, Kevin Raymond, Ali Khademhosseini, and P. Chen. Biocompatibility of engineered nanoparticles for drug delivery. *Journal of Controlled Release*, 166(2):182–194, 2013.

[14] Ernest M. Hotze, Tanapon Phenrat, and Gregory V. Lowry. Nanoparticle aggregation: Challenges to understanding transport and reactivity in the environment. *Journal of Environmental Quality*, 39(6):1909–1924, 2010.

[15] Barry W Ninham and Vassili Yaminsky. Ion binding and ion specificity: the hofmeister effect and onsager and lifshitz theories. *Langmuir*, 13(7):2097–2108, 1997.

[16] B. W. Ninham. On progress in forces since the dlvo theory. *Advances in Colloid and Interface Science*, 83(13):1–17, 1999.

[17] Barry W. Ninham, Richard M. Pashley, and Pierandrea Lo Nostro. Surface forces: Changing concepts and complexity with dissolved gas, bubbles, salt and heat. *Current Opinion in Colloid & Interface Science*, 27:25 – 32, 2017.

[18] Carlos A. Silvera Batista, Ronald G. Larson, and Nicholas A. Kotov. Nonadditivity of nanoparticle interactions. *Science*, 350(6257), 2015.

[19] Guillermo Iván Guerrero-García, Pedro González-Mozuelos, and Monica Olvera de la Cruz. Large counterions boost the solubility and renormalized charge of suspended nanoparticles. *ACS Nano*, 7(11):9714–9723, 2013. PMID: 24180597.

[20] William A Ducker, Tim J Senden, and Richard M Pashley. Direct measurement of colloidal forces using an atomic force microscope. *nature*, 353(6341):239–241, 1991.

[21] Hans-Jürgen Butt. Measuring electrostatic, van der waals, and hydration forces in electrolyte solutions with an atomic force microscope. *Biophysical Journal*, 60(6):1438–1444, 1991.

[22] G. Binnig, C. F. Quate, and Ch. Gerber. Atomic force microscope. *Phys. Rev. Lett.*, 56:930–933, Mar 1986.

[23] Wenhai Han, Jianxun Mou, Jun Sheng, Jie Yang, and Zhifeng Shao. Cryo atomic force microscopy: A new approach for biological imaging at high resolution. *Biochemistry*, 34(26):8215–8220, 1995.

[24] Rico F. Tabor, Rogerio Manica, Derek Y. C. Chan, Franz Grieser, and Raymond R. Dagastine. Repulsive van der waals forces in soft matter: Why bubbles do not stick to walls. *Physical Review Letters*, 106(6):064501, 2011.

[25] Esben Thormann, Adam C. Simonsen, Per L. Hansen, and Ole G. Mouritsen. Interactions between a polystyrene particle and hydrophilic and hydrophobic surfaces in aqueous solutions. *Langmuir*, 24(14):7278–7284, 2008.

[26] Andrew Milling and Simon Biggs. Direct measurement of the depletion force using an atomic force microscope. *Journal of Colloid and Interface Science*, 170(2):604–606, 1995.

[27] Michal Borkovec, Istvan Szilagyi, Ionel Popa, Marco Finessi, Prashant Sinha, Plinio Maroni, and Georg Papastavrou. Investigating forces between charged particles in the presence of oppositely charged polyelectrolytes with the multi-particle colloidal probe technique. *Advances in Colloid and Interface Science*, 179182(0):85–98, 2012.

[28] Barbara M. Alexander and Dennis C. Prieve. A hydrodynamic technique for measurement of colloidal forces. *Langmuir*, 3(5):788–795, 1987.

[29] Dennis C. Prieve, Foo Luo, and Frederick Lanni. Brownian motion of a hydrosol particle in a colloidal force field. *Faraday Discussions of the Chemical Society*, 83(0):297–307, 1987.

[30] Michael A Bevan and Dennis C Prieve. Direct measurement of retarded van der waals attraction. *Langmuir*, 15(23):7925–7936, 1999.

[31] Michael A. Bevan and Dennis C. Prieve. Forces and hydrodynamic interactions between polystyrene surfaces with adsorbed peoppopeo. *Langmuir*, 16(24):9274–9281, 2000.

[32] C. Hertlein, L. Helden, A. Gambassi, S. Dietrich, and C. Bechinger. Direct measurement of critical casimir forces. *nature*, 451(7175):172–175, 2008.

[33] V. Blickle, T. Speck, L. Helden, U. Seifert, and C. Bechinger. Thermodynamics of a colloidal particle in a time-dependent nonharmonic potential. *Physical Review Letters*, 96(7):070603, 2006.

[34] Dennis C. Prieve. Measurement of colloidal forces with tirm. *Advances in Colloid and Interface Science*, 82(13):93–125, 1999.

[35] Lulu Liu, Alexander Woolf, Alejandro W. Rodriguez, and Federico Capasso. Absolute position total internal reflection microscopy with an optical tweezer. *Proceedings of the National Academy of Sciences*, 111(52):E5609–E5615, 2014.

[36] Shannon L. Eichmann, Samartha G. Anekal, and Michael A. Bevan. Electrostatically confined nanoparticle interactions and dynamics. *Langmuir*, 24(3):714–721, 2008.

[37] Shannon L. Eichmann and Michael A. Bevan. Direct measurements of protein-stabilized gold nanoparticle interactions. *Langmuir*, 26(18):14409–14413, 2010.

[38] Shannon L. Eichmann, Billy Smith, Gulsum Meric, D. Howard Fairbrother, and Michael A. Bevan. Imaging carbon nanotube interactions, diffusion, and stability in nanopores. *ACS Nano*, 5(7):5909–5919, 2011.

[39] Yutaka Kazoe, Kazuma Mawatari, and Takehiko Kitamori. Behavior of nanoparticles in extended nanospace measured by evanescent wave-based particle velocimetry. *Analytical Chemistry*, 87(8):4087–4091, 2015.

[40] Karel Svoboda and Steven M. Block. Optical trapping of metallic rayleigh particles. *Optics Letters*, 19(13):930–932, 1994.

[41] Huanjun Chen, Xiaoshan Kou, Zhi Yang, Weihai Ni, and Jianfang Wang. Shape-and size-dependent refractive index sensitivity of gold nanoparticles. *Langmuir*, 24(10):5233–5237, 2008.

[42] Kurosch Rezwan, Lorenz P Meier, Mandana Rezwan, Janos Vörös, Marcus Textor, and Ludwig J Gauckler. Bovine serum albumin adsorption onto colloidal al2o3 particles: a new model based on zeta potential and uv- vis measurements. *Langmuir*, 20(23):10055–10061, 2004.

[43] Edit Csapó, Rita Patakfalvi, Viktória Hornok, László Tamás Tóth, Áron Sipos, Anikó Szalai, Mária Csete, and Imre Dékány. Effect of ph on stabil-

ity and plasmonic properties of cysteine-functionalized silver nanoparticle dispersion. *Colloids and Surfaces B: Biointerfaces*, 98:43–49, 2012.

[44] Jie Gao, Xiangyi Huang, Heng Liu, Feng Zan, and Jicun Ren. Colloidal stability of gold nanoparticles modified with thiol compounds: bioconjugation and application in cancer cell imaging. *Langmuir*, 28(9):4464–4471, 2012.

[45] AV Delgado, Fernando González-Caballero, RJ Hunter, LK Koopal, and J Lyklema. Measurement and interpretation of electrokinetic phenomena (iupac technical report). *Pure and Applied Chemistry*, 77(10):1753–1805, 2005.

[46] R. Pecora. Dynamic light scattering measurement of nanometer particles in liquids. *Journal of Nanoparticle Research*, 2(2):123–131, 2000.

[47] Andrew Malloy and Bob Carr. Nanoparticle tracking analysis the halo system. *Particle & Particle Systems Characterization*, 23(2):197–204, 2006.

[48] Vasco Filipe, Andrea Hawe, and Wim Jiskoot. Critical evaluation of nanoparticle tracking analysis (nta) by nanosight for the measurement of nanoparticles and protein aggregates. *Pharmaceutical Research*, 27(5):796–810, 2010.

[49] Xinsheng Tian, M. Reza Nejadnik, Dorrit Baunsgaard, Anette Henriksen, Christian Rischel, and Wim Jiskoot. A comprehensive evaluation of nanoparticle tracking analysis (nanosight) for characterization of proteinaceous submicron particles. *Journal of Pharmaceutical Sciences*, 105(11):3366 – 3375, 2016.

[50] E. van der Pol, F. A. W. Coumans, A. E. Grootemaat, C. Gardiner, I. L. Sargent, P. Harrison, A. Sturk, T. G. van Leeuwen, and R. Nieuwland. Particle size distribution of exosomes and microvesicles determined by transmission electron microscopy, flow cytometry, nanoparticle tracking analysis, and resistive pulse sensing. *Journal of Thrombosis and Haemostasis*, 12(7):1182–1192, 2014.

[51] John Hartman and Brian Kirby. Decorrelation correction for nanoparticle tracking analysis of dilute polydisperse suspensions in bulk flow. *Phys. Rev. E*, 95:033305, Mar 2017.

[52] A. Ashkin. Acceleration and trapping of particles by radiation pressure. *Phys. Rev. Lett.*, 24:156–159, Jan 1970.

[53] A. Ashkin, J. M. Dziedzic, J. E. Bjorkholm, and Steven Chu. Observation of a single-beam gradient force optical trap for dielectric particles. *Optics Letters*, 11(5):288–290, 1986.

[54] Keir C. Neuman and Steven M. Block. Optical trapping. *Review of Scientific Instruments*, 75(9):2787–2809, 2004.

[55] David G Grier. A revolution in optical manipulation. *Nature*, 424(6950):810–816, 2003.

[56] David Erickson, Xavier Serey, Yih-Fan Chen, and Sudeep Mandal. Nanomanipulation using near field photonics. *Lab on a Chip*, 11(6):995–1009, 2011.

[57] Sudeep Mandal, Julie M. Goddard, and David Erickson. A multiplexed optofluidic biomolecular sensor for low mass detection. *Lab on a Chip*, 9(20):2924–2932, 2009.

[58] Xavier Serey, Sudeep Mandal, Yih-Fan Chen, and David Erickson. Dna transport and delivery in thermal gradients near optofluidic resonators. *Physical Review Letters*, 108(4):048102, 2012.

[59] Yih-Fan Chen, Xavier Serey, Rupa Sarkar, Peng Chen, and David Erickson. Controlled photonic manipulation of proteins and other nanomaterials. *Nano Letters*, 12(3):1633–1637, 2012.

[60] P Kang, P Schein, X Serey, D O'Dell, and D Erickson. Nanophotonic detection of freely interacting molecules on a single influenza virus. *Scientific Reports*, 5.

[61] X Serey, S Mandal, and D Erickson. Comparison of silicon photonic crystal resonator designs for optical trapping of nanomaterials. *Nanotechnology*, 21(30):305202, 2010.

[62] Satoshi Kawata and Tadao Sugiura. Movement of micrometer-sized particles in the evanescent field of a laser beam. *Optics Letters*, 17(11):772–774, 1992.

[63] S. Kawata and T. Tani. Optically driven mie particles in an evanescent field along a channeled waveguide. *Optics Letters*, 21(21):1768–1770, 1996.

[64] L. N. Ng, B. J. Luff, M. N. Zervas, and J. S. Wilkinson. Forces on a rayleigh

particle in the cover region of a planar waveguide. *Journal of Lightwave Technology*, 18(3):388, 2000.

[65] L. N. Ng, B. J. Luff, M. N. Zervas, and J. S. Wilkinson. Propulsion of gold nanoparticles on optical waveguides. *Optics Communications*, 208(13):117–124, 2002.

[66] S. Gaugiran, S. Getin, J. Fedeli, G. Colas, A. Fuchs, F. Chatelain, and J. Derouard. Optical manipulation of microparticles and cells on silicon nitride waveguides. *Optics Express*, 13(18):6956–6963, 2005.

[67] B. S. Ahluwalia, A. Z. Subramanian, O. G. Hellso, N. M. B. Perney, N. P. Sessions, and J. S. Wilkinson. Fabrication of submicrometer high refractive index tantalum pentoxide waveguides for optical propulsion of microparticles. *IEEE Photonics Technology Letters*, 21(19):1408–1410, 2009.

[68] Balpreet Singh Ahluwalia, øystein Ivar Helle, and Olav Gaute Hellesø. Rib waveguides for trapping and transport of particles. *Optics Express*, 24(5):4477–4487, 2016.

[69] Yuncheng Liang, Nidal Hilal, Paul Langston, and Victor Starov. Interaction forces between colloidal particles in liquid: Theory and experiment. *Advances in Colloid and Interface Science*, 134135(0):151–166, 2007.

[70] V Adrian Parsegian. *Van der Waals forces: a handbook for biologists, chemists, engineers, and physicists*. Cambridge Univ. Press, Cambridge, 2006.

[71] J. Padding and A. Louis. Hydrodynamic interactions and brownian forces in colloidal suspensions: Coarse-graining over time and length scales. *Physical Review E*, 74(3):031402, 2006.

[72] F. Caruso. Nanoengineering of particle surfaces. *Advanced Materials*, 13(1):11–22, 2001.

[73] Emmanuel Trizac and Jean-Luc Raimbault. Long-range electrostatic interactions between like-charged colloids: Steric and confinement effects. *Physical Review E*, 60(6):6530–6533, 1999.

[74] Rebecca A. French, Astrid R. Jacobson, Bojeong Kim, Sara L. Isley, R. Lee Penn, and Philippe C. Baveye. Influence of ionic strength, ph, and cation valence on aggregation kinetics of titanium dioxide nanoparticles. *Environmental Science & Technology*, 43(5):1354–1359, 2009.

[75] A. Guyot. Advances in reactive surfactants. *Advances in Colloid and Interface Science*, 108109(0):3–22, 2004.

[76] Motoyuki Iijima and Hidehiro Kamiya. Surface modification for improving the stability of nanoparticles in liquid media. *KONA Powder and Particle Journal*, 27:119–129, 2009.

[77] Jared S. Bee, Michele Davis, Erwin Freund, John F. Carpenter, and Theodore W. Randolph. Aggregation of a monoclonal antibody induced by adsorption to stainless steel. *Biotechnology and Bioengineering*, 105(1):121–129, 2010.

[78] Michael Kappl and Hans-Jürgen Butt. The colloidal probe technique and its application to adhesion force measurements. *Particle & Particle Systems Characterization*, 19(3):129–143, 2002.

[79] Hans-Jürgen Butt, Brunero Cappella, and Michael Kappl. Force measurements with the atomic force microscope: Technique, interpretation and applications. *Surface Science Reports*, 59(16):1–152, 2005.

[80] Xiangjun Gong, Zhaohui Wang, and To Ngai. Direct measurements of particle-surface interactions in aqueous solutions with total internal reflection microscopy. *Chemical Communications*, 50(50):6556–6570, 2014.

[81] Xiaoling Wei, Xiangjun Gong, and To Ngai. Interactions between solid surfaces mediated by polyethylene oxide polymers: Effect of polymer concentration. *Langmuir*, 29(35):11038–11045, 2013.

[82] Gregory E. Fernandes and Michael A. Bevan. Equivalent temperature and specific ion effects in macromolecule-coated colloid interactions. *Langmuir*, 23(3):1500–1506, 2006.

[83] A. Ashkin. Forces of a single-beam gradient laser trap on a dielectric sphere in the ray optics regime. *Biophysical Journal*, 61(2):569–582, 1992.

[84] Dennis C. Prieve and Nasser A. Frej. Total internal reflection microscopy: a quantitative tool for the measurement of colloidal forces. *Langmuir*, 6(2):396–403, 1990.

[85] Yasuhiro Harada and Toshimitsu Asakura. Radiation forces on a dielectric sphere in the rayleigh scattering regime. *Optics Communications*, 124(56):529–541, 1996.

[86] Igor Sokolov, Quy K. Ong, Hasan Shodiev, Nina Chechik, David James, and Mike Oliver. Afm study of forces between silica, silicon nitride and polyurethane pads. *Journal of Colloid and Interface Science*, 300(2):475–481, 2006.

[87] Jason C. W. Corbett, Fraser McNeil-Watson, Robert O. Jack, and Martin Howarth. Measuring surface zeta potential using phase analysis light scattering in a simple dip cell arrangement. *Colloids and Surfaces A: Physicochemical and Engineering Aspects*, 396(0):169–176, 2012.

[88] H. H. von Grünberg, L. Helden, P. Leiderer, and C. Bechinger. Measurement of surface charge densities on brownian particles using total internal reflection microscopy. *The Journal of Chemical Physics*, 114(22):10094–10104, 2001.

[89] José Juan López-García, José Horno, and Constantino Grosse. Poisson-boltzmann description of the electrical double layer including ion size effects. *Langmuir*, 27(23):13970–13974, 2011.

[90] Satoru Ayano, Yuichi Wakamoto, Shinobu Yamashita, and Kenji Yasuda. Quantitative measurement of damage caused by 1064-nm wavelength optical trapping of escherichia coli cells using on-chip single cell cultivation system. *Biochemical and Biophysical Research Communications*, 350(3):678–684, 2006.

[91] Nanotechnology: A realistic market assessment [internet], 2014 Nov.

[92] Isao Matsui. Nanoparticles for electronic device applications: A brief review. *Journal of Chemical Engineering of Japan*, 38(8):535–546, 2005.

[93] Oleg V Salata. Applications of nanoparticles in biology and medicine. *Journal of nanobiotechnology*, 2(1):3, 2004.

[94] Tais A. P. F. Doll, Senthilkumar Raman, Raja Dey, and Peter Burkhard. Nanoscale assemblies and their biomedical applications. *Journal of The Royal Society Interface*, 10(80), 2013.

[95] Feng Jia, Xunpei Liu, Linheng Li, Surya Mallapragada, Balaji Narasimhan, and Qun Wang. Multifunctional nanoparticles for targeted delivery of immune activating and cancer therapeutic agents. *Journal of Controlled Release*, 172(3):1020–1034, 2013.

[96] G. L. Prasad. *Biomedical Applications of Nanoparticles*, chapter 5, pages 89–109. Nanostructure Science and Technology. Springer New York, 2009.

[97] D. W Grainger and D. G Castner. Nanobiomaterials and nanoanalysis: Opportunities for improving the science to benefit biomedical technologies. *Advanced Materials*, 20(5):867–877, 2008.

[98] Erik C. Dreaden, Alaaldin M. Alkilany, Xiaohua Huang, Catherine J. Murphy, and Mostafa A. El-Sayed. The golden age: gold nanoparticles for biomedicine. *Chem. Soc. Rev.*, 41(7):2740–2779, 2012.

[99] Elvin Blanco, Angela Hsiao, Aman P. Mann, Matthew G. Landry, Funda Meric-Bernstam, and Mauro Ferrari. Nanomedicine in cancer therapy: Innovative trends and prospects. *Cancer Science*, 102(7):1247–1252, 2011.

[100] Vicki H. Grassian. When size really matters: Size-dependent properties and surface chemistry of metal and metal oxide nanoparticles in gas and liquid phase environments. *The Journal of Physical Chemistry C*, 112(47):18303–18313, 2008.

[101] D. R. Baer, D. J. Gaspar, P. Nachimuthu, S. D. Techane, and D. G. Castner. Application of surface chemical analysis tools for characterization of nanoparticles. *Analytical and Bioanalytical Chemistry*, 396(3):983–1002, 2010.

[102] Ayush Verma and Francesco Stellacci. Effect of surface properties on nanoparticlecell interactions. *Small*, 6(1):12–21, 2010.

[103] C. Lee Ventola. The nanomedicine revolution: Part 1: Emerging concepts. *Pharmacy and Therapeutics*, 37(9):512–525, 2012.

[104] Hans Bouwmeester, Iseult Lynch, Hans J. P. marvin, Kenneth A. Dawson, Markus Berges, Diane Braguer, Hugh J. Byrne, Alan Casey, Gordon Chambers, Martin J. D. Clift, Giuliano Elia, Teresa F. Fernandes, Lise B. Fjellsbø, Peter Hatto, Lucienne Juillerat, Christoph Klein, Wolfgang G. Kreyling, Carmen Nickel, Michael Riediker, and Vicki Stone. Minimal analytical characterization of engineered nanomaterials needed for hazard assessment in biological matrices. *Nanotoxicology*, 5(1):1–11, 2011.

[105] Sonia Ramirez-Garcia, Lan Chen, Michael A. Morris, and Kenneth A. Dawson. A new methodology for studying nanoparticle interactions in biological systems: Dispersing titania in biocompatible media using chemical stabilisers. *Nanoscale*, 3(11):4617–4624, 2011.

[106] Marco P. Monopoli, Christoffer Aberg, Anna Salvati, and Kenneth A. Dawson. Biomolecular coronas provide the biological identity of nanosized materials. *Nat Nano*, 7(12):779–786, 2012.

[107] DJ Shaw. Introduction to surface and colloid chemistry, 1992.

[108] Dennis C. Prieve and Mitchell M. J. Lin. The effect of a distribution in surface properties on colloid stability. *Journal of Colloid and Interface Science*, 86(1):17–25, 1982.

[109] Vivian S. W. Chan. Nanomedicine: An unresolved regulatory issue. *Regulatory Toxicology and Pharmacology*, 46(3):218–224, 2006.

[110] Neil Desai. Challenges in development of nanoparticle-based therapeutics. *The AAPS Journal*, 14(2):282–295, 2012.

[111] Nanomedicines Drafting Group. Reflection paper on surface coatings: general issues for consideration regarding parenteral administration of coated nanomedicine products, 2013.

[112] D. R. Baer. Application of surface analysis methods to nanomaterials: summary of iso/tc 201 technical report: Iso 14187:2011 surface chemical analysis characterization of nanomaterials. *Surface and Interface Analysis*, 44(9):1305–1308, 2012.

[113] Lingbo Kong, Changwon Lee, Christopher M. Earhart, Bernardo Cordovez, and James W. Chan. A nanotweezer system for evanescent wave excited surface enhanced raman spectroscopy (sers) of single nanoparticles. *Optics Express*, 23(5):6793–6802, 2015.

[114] Pal Løvhaugen, Balpreet Singh Ahluwalia, Thomas R. Huser, and Olav Gaute Hellesø. Serial raman spectroscopy of particles trapped on a waveguide. *Optics Express*, 21(3):2964–2970, 2013.

[115] D. J Sirbuly, A. Tao, M. Law, R. Fan, and P. Yang. Multifunctional nanowire evanescent wave optical sensors. *Advanced Materials*, 19(1):61–66, 2007.

[116] Bradley S. Schmidt, Allen H. Yang, David Erickson, and Michal Lipson. Optofluidic trapping and transport on solid core waveguides within a microfluidic device. *Optics Express*, 15(22):14322–14334, 2007.

[117] DA McQuarrie. *Statistical Mechanics. 2000*, volume 12.

[118] Giovanni Volpe, Thomas Brettschneider, Laurent Helden, and Clemens Bechinger. Novel perspectives for the application of total internal reflection microscopy. *Optics Express*, 17(26):23975–23985, 2009.

[119] R. Morrow, D. R. McKenzie, and M. M. M. Bilek. The time-dependent development of electric double-layers in saline solutions. *Journal of Physics D: Applied Physics*, 39(5):937, 2006.

[120] Stacy G. Bike. Measuring colloidal forces using evanescent wave scattering. *Current Opinion in Colloid & Interface Science*, 5(12):144–150, 2000.

[121] Krishnendu Saha, Sarit S. Agasti, Chaekyu Kim, Xiaoning Li, and Vincent M. Rotello. Gold nanoparticles in chemical and biological sensing. *Chemical Reviews*, 112(5):2739–2779, 2012.

[122] Kun Qian, Brendan C. Sweeny, Aaron C. Johnston-Peck, Wenxin Niu, Jeremy O. Graham, Joseph S. DuChene, Jingjing Qiu, Yi-Chung Wang, Mark H. Engelhard, Dong Su, Eric A. Stach, and Wei David Wei. Surface plasmon-driven water reduction: Gold nanoparticle size matters. *Journal of the American Chemical Society*, 136(28):9842–9845, 2014.

[123] John W. Hickey, Jose Luis Santos, John-Michael Williford, and Hai-Quan Mao. Control of polymeric nanoparticle size to improve therapeutic delivery. *Journal of Controlled Release*, 219:536–547, 2015.

[124] Marie Gaumet, Angelica Vargas, Robert Gurny, and Florence Delie. Nanoparticles for drug delivery: The need for precision in reporting particle size parameters. *European Journal of Pharmaceutics and Biopharmaceutics*, 69(1):1–9, 2008.

[125] Carolyn L. Phillips and Sharon C. Glotzer. Effect of nanoparticle polydispersity on the self-assembly of polymer tethered nanospheres. *The Journal of Chemical Physics*, 137(10):104901, 2012.

[126] David Zhitomirsky, Illan J. Kramer, Andr J. Labelle, Armin Fischer, Ratan Debnath, Jun Pan, Osman M. Bakr, and Edward H. Sargent. Colloidal quantum dot photovoltaics: The effect of polydispersity. *Nano Letters*, 12(2):1007–1012, 2012.

[127] Libo Wu, Jian Zhang, and Wiwik Watanabe. Physical and chemical stability of drug nanoparticles. *Advanced Drug Delivery Reviews*, 63(6):456–469, 2011.

[128] Julian A Gallego-Urrea, Jani Tuoriniemi, and Martin Hassellöv. Applications of particle-tracking analysis to the determination of size distributions and concentrations of nanoparticles in environmental, biological and food samples. *TRAC Trends in Analytical Chemistry*, 30(3):473–483, 2011.

[129] J Drelich, J Long, Z Xu, J Masliyah, J Nalaskowski, R Beauchamp, and Y Liu. Afm colloidal forces measured between microscopic probes and flat substrates in nanoparticle suspensions. *Journal of Colloid and Interface Science*, 301(2):511–522, 2006.

[130] Christopher M Hoo, Natasha Starostin, Paul West, and Martha L Mecartney. A comparison of atomic force microscopy (afm) and dynamic light scattering (dls) methods to characterize nanoparticle size distributions. *Journal of Nanoparticle Research*, 10(1):89–96, 2008.

[131] Robert D Boyd, Siva K Pichaimuthu, and Alexandre Cuenat. New approach to inter-technique comparisons for nanoparticle size measurements; using atomic force microscopy, nanoparticle tracking analysis and dynamic light scattering. *Colloids and Surfaces A: Physicochemical and Engineering Aspects*, 387(1):35–42, 2011.

[132] John F. Carpenter, Theodore W. Randolph, Wim Jiskoot, Daan J. A. Crommelin, C. Russell Middaugh, and Gerhard Winter. Potential inaccurate quantitation and sizing of protein aggregates by size exclusion chromatography: Essential need to use orthogonal methods to assure the quality of therapeutic protein products. *Journal of Pharmaceutical Sciences*, 99(5):2200–2208, 2010.

[133] Monique J. Jacobs and Kerstin Blank. Joining forces: integrating the mechanical and optical single molecule toolkits. *Chemical Science*, 5(5):1680–1697, 2014.

[134] A. J. Goldman, R. G. Cox, and H. Brenner. Slow viscous motion of a sphere parallel to a plane walli motion through a quiescent fluid. *Chemical Engineering Science*, 22(4):637–651, 1967.

[135] I. F. Sbalzarini and P. Koumoutsakos. Feature point tracking and trajectory analysis for video imaging in cell biology. *Journal of Structural Biology*, 151(2):182–195, 2005.

[136] Moshe Lindner, Guy Nir, Anat Vivante, Ian T. Young, and Yuval Garini.

Dynamic analysis of a diffusing particle in a trapping potential. *Physical Review E*, 87(2):022716, 2013. PRE.

[137] Dakota O'Dell, Perry Schein, and David Erickson. Simultaneous characterization of nanoparticle size and particle-surface interactions with 3d nanophotonic force microscopy. 2016.

[138] Arindam Banerjee and Kenneth D. Kihm. Experimental verification of near-wall hindered diffusion for the brownian motion of nanoparticles using evanescent wave microscopy. *Physical Review E*, 72(4):042101, 2005. PRE.

[139] E. Almaas and I. Brevik. Radiation forces on a micrometer-sized sphere in an evanescent field. *Journal of the Optical Society of America B*, 12(12):2429–2438, 1995.

[140] Hung-Jen Wu, Suhani Shah, Richard Beckham, Kenith E. Meissner, and Michael A. Bevan. Resonant effects in evanescent wave scattering of polydisperse colloids. *Langmuir*, 24(23):13790–13795, 2008.

[141] Christophe Pin, Benoit Cluzel, Claude Renaut, Emmanuel Picard, David Peyrade, Emmanuel Hadji, and Frederique de Fornel. Optofluidic near-field optical microscopy: Near-field mapping of a silicon nanocavity using trapped microbeads. *ACS Photonics*, 2(10):1410–1415, 2015.

[142] Djenan Ganic, Xiaosong Gan, and M. i n Gu. Three-dimensional evanescent wave scattering by dielectric particles. *Optik - International Journal for Light and Electron Optics*, 113(3):135–141, 2002.

[143] Djenan Ganic, Xiaosong Gan, and Min Gu. Parametric study of three-dimensional near-field mie scattering by dielectric particles. *Optics Communications*, 216(13):1–10, 2003.

[144] John F. Carpenter, Theodore W. Randolph, Wim Jiskoot, Daan J. A. Crommelin, C. Russell Middaugh, Gerhard Winter, Ying-Xin Fan, Susan Kirshner, Daniela Verthelyi, Steven Kozlowski, Kathleen A. Clouse, Patrick G. Swann, Amy Rosenberg, and Barry Cherney. Overlooking subvisible particles in therapeutic protein products: Gaps that may compromise product quality. *Journal of Pharmaceutical Sciences*, 98(4):1201–1205, 2009.

[145] Nicolas Chenouard, Ihor Smal, Fabrice de Chaumont, Martin Maska, Ivo F. Sbalzarini, Yuanhao Gong, Janick Cardinale, Craig Carthel, Stefano Coraluppi, Mark Winter, Andrew R. Cohen, William J. Godinez, Karl

Rohr, Yannis Kalaidzidis, Liang Liang, James Duncan, Hongying Shen, Yingke Xu, Klas E. G. Magnusson, Joakim Jalden, Helen M. Blau, Perrine Paul-Gilloteaux, Philippe Roudot, Charles Kervrann, Francois Waharte, Jean-Yves Tinevez, Spencer L. Shorte, Joost Willemse, Katherine Celler, Gilles P. van Wezel, Han-Wei Dan, Yuh-Show Tsai, Carlos Ortiz de Solorzano, Jean-Christophe Olivo-Marin, and Erik Meijering. Objective comparison of particle tracking methods. *Nat Meth*, 11(3):281–289, 2014.

[146] A. J. Goldman, R. G. Cox, and H. Brenner. Slow viscous motion of a sphere parallel to a plane walli motion through a quiescent fluid. *Chemical Engineering Science*, 22(4):637–651, 1967.

[147] A. J. Goldman, R. G. Cox, and H. Brenner. Slow viscous motion of a sphere parallel to a plane wallii couette flow. *Chemical Engineering Science*, 22(4):653–660, 1967.

[148] Alec T. Clark, Moti Lal, and Gill M. Watson. Dynamics of colloidal particles in the vicinity of an interacting surface. *Faraday Discussions of the Chemical Society*, 83(0):179–191, 1987.

[149] G. D. M. MacKay, M. Suzuki, and S. G. Mason. Approach of a solid sphere to a rigid plane interface. part 2. *Journal of Colloid Science*, 18(1):103–104, 1963.

[150] Erik Schffer, Simon F. Nrrelykke, and Jonathon Howard. Surface forces and drag coefficients of microspheres near a plane surface measured with optical tweezers. *Langmuir*, 23(7):3654–3665, 2007.

[151] Mauricio D. Carbajal-Tinoco, Ricardo Lopez-Fernandez, and Jos Luis Arauz-Lara. Asymmetry in colloidal diffusion near a rigid wall. *Physical Review Letters*, 99(13):138303, 2007. PRL.

[152] Peter Huang and Kenneth S. Breuer. Direct measurement of anisotropic near-wall hindered diffusion using total internal reflection velocimetry. *Physical Review E*, 76(4):046307, 2007. PRE.

[153] Murray A. Brown and E. J. Staples. Measurement of absolute particle-surface separation using total internal reflection microscopy and radiation pressure forces. *Langmuir*, 6(7):1260–1265, 1990.

[154] Nasser A. Frej and Dennis C. Prieve. Hindered diffusion of a single sphere

very near a wall in a nonuniform force field. *The Journal of Chemical Physics*, 98(9):7552–7564, 1993.

[155] D. W. Pilat, B. Pouligny, A. Best, T. A. Nick, R. Berger, and H. J. Butt. Surface forces between colloidal particles at high hydrostatic pressure. *Physical Review E*, 93(2):022608, 2016. PRE.

[156] Perry Schein, Pilgyu Kang, Dakota ODell, and David Erickson. Nanophotonic force microscopy: Characterizing particlesurface interactions using near-field photonics. *Nano Letters*, 15(2):1414–1420, 2015.

[157] Perry Schein, Colby K. Ashcroft, Dakota ODell, Ian S. Adam, Brian DiPaolo, Manit Sabharwal, Ce Shi, Robert Hart, Christopher Earhart, and David Erickson. Near-field light scattering techniques for measuring nanoparticle-surface interaction energies and forces. *Journal of Lightwave Technology*, 33(16):3494–3502, 2015.

[158] Thomas Brettschneider, Giovanni Volpe, Laurent Helden, Jan Wehr, and Clemens Bechinger. Force measurement in the presence of brownian noise: Equilibrium-distribution method versus drift method. *Physical Review E*, 83(4):041113, 2011. PRE.

[159] K. D. Kihm, A. Banerjee, C. K. Choi, and T. Takagi. Near-wall hindered brownian diffusion of nanoparticles examined by three-dimensional ratiometric total internal reflection fluorescence microscopy (3-d r-tirfm). *Experiments in Fluids*, 37(6):811–824, 2004.

[160] Jan Axelson. *USB complete: the developer's guide*. Lakeview research LLC, 2015.

[161] Alexander Gondarenko, Jacob S. Levy, and Michal Lipson. High confinement micron-scale silicon nitride high q ring resonator. *Opt. Express*, 17(14):11366–11370, Jul 2009.

[162] Huziel E. Sauceda, Denis Mongin, Paolo Maioli, Aurélien Crut, Michel Pellarin, Natalia Del Fatti, Fabrice Vallée, and Ignacio L. Garzón. Vibrational properties of metal nanoparticles: Atomistic simulation and comparison with time-resolved investigation. *The Journal of Physical Chemistry C*, 116(47):25147–25156, 2012.

[163] Juan J. Torres-Vega, L.R. Medrano, C.V. Landauro, and J. Rojas-Tapia. Determination of the threshold of nanoparticle behavior: Structural and elec-

tronic properties study of nano-sized copper. *Physica B: Condensed Matter*, 436:74 – 79, 2014.

[164] José Luis Corchero, Brigitte Gasser, David Resina, Wesley Smith, Ermenegilda Parrilli, Felcitas Vzquez, Ibane Abasolo, Maria Giuliani, Jussi Jntti, Pau Ferrer, Markku Saloheimo, Diethard Mattanovich, Simó Schwartz Jr., Maria Luisa Tutino, and Antonio Villaverde. Unconventional microbial systems for the cost-efficient production of high-quality protein therapeutics. *Biotechnology Advances*, 31(2):140 – 153, 2013.

[165] Karthik P. Jayapal, Katie F. Wlaschin, Wei-Shou Hu, and Miranda G. S. Yap. Recombinant protein therapeutics from cho cells - 20 years and counting. *Chemical Engineering Progress*, 103(10):40–47, 10 2007.

[166] James G Barnard, Ken Babcock, and John F Carpenter. Characterization and quantitation of aggregates and particles in interferon-β products: Potential links between product quality attributes and immunogenicity. *Journal of pharmaceutical sciences*, 102(3):915–928, 2013.

[167] Wei Wang, Satish K Singh, Ning Li, Maria R Toler, Kevin R King, and Sandeep Nema. Immunogenicity of protein aggregatesconcerns and realities. *International journal of pharmaceutics*, 431(1):1–11, 2012.

[168] Satish K Singh, Nataliya Afonina, Michel Awwad, Karoline Bechtold-Peters, Jeffrey T Blue, Danny Chou, Mary Cromwell, Hans-Juergen Krause, Hanns-Christian Mahler, Brian K Meyer, et al. An industry perspective on the monitoring of subvisible particles as a quality attribute for protein therapeutics. *Journal of pharmaceutical sciences*, 99(8):3302–3321, 2010.

[169] Miranda Van Beers, Francesca Gilli, Huub Schellekens, Theodore W Randolph, and WIM Jiskoot. Immunogenicity of recombinant human interferon beta interacting with particles of glass, metal, and polystyrene. *Journal of pharmaceutical sciences*, 101(1):187–199, 2012.

[170] Kirsty D Ratanji, Jeremy P Derrick, Rebecca J Dearman, and Ian Kimber. Immunogenicity of therapeutic proteins: influence of aggregation. *Journal of immunotoxicology*, 11(2):99–109, 2014.